REPORT DOCUMENTATION PAGE

Form Approved
OMB No. 0704-0188

1. REPORT DATE *(DD-MM-YYYY)*	**2. REPORT TYPE**	**3. DATES COVERED** *(From - To)*
27-08-2003	Progress	August 2000-August 2003

4. TITLE AND SUBTITLE
Streamwise Vortex Instability and Hypersonic Boundary-Layer Transition on the Hyper-2000

5a. CONTRACT NUMBER

5b. GRANT NUMBER
F49620-03-1-0030

5c. PROGRAM ELEMENT NUMBER

6. AUTHOR(S)
Shin Matsumura

5d. PROJECT NUMBER

5e. TASK NUMBER

5f. WORK UNIT NUMBER

7. PERFORMING ORGANIZATION NAME(S) AND ADDRESS(ES)
Purdue University, School of Aeronautics and Astronautics
Steven P. Schneider
Aerospace Sciences Lab
1375 Aviation Drive
West Lafayette IN 47907-2015

8. PERFORMING ORGANIZATION REPORT NUMBER

9. SPONSORING / MONITORING AGENCY NAME(S) AND ADDRESS(ES)
Air Force Office of
Scientific Research
4015 Wilson Blvd
Arlington VA 22203

10. SPONSOR/MONITOR'S ACRONYM(S)
AFOSR

11. SPONSOR/MONITOR'S REPORT NUMBER(S)

12. DISTRIBUTION / AVAILABILITY STATEMENT

Approved for public release. Distribution unlimited.

13. SUPPLEMENTARY NOTES
M.S. thesis research supported by NASA Langley under Grant NAG-1-02047 and also by AFOSR.

14. ABSTRACT
Despite the closely coupled nature of hypersonic airbreathing vehicles, the boundary layer transition mechanisms on the forebody ahead of the scramjet inlet are not well understood. Transition induced by the growth of streamwise vortices is studied on a scramjet forebody geometry similar to the Hyper-X. Flow visualization methods are developed in Purdue's Boeing/AFOSR Mach-6 Quiet Tunnel. Fluorescent oil-flow visualization is used to complement instability measurements obtained with temperature-sensitive-paints. The separation zone near the first compression corner is visualized with oil-flow experiments. These experiments also reveal the presence of regularly spaced streamwise vortices on the compression ramp even in the absence of controlled disturbance generators. The growth and decay of these vortices are inferred from heat-transfer measurements using temperature-sensitive paints. Repeatable vortices are generated by wrapping tapes around the leading edge.

15. SUBJECT TERMS
Hypersonic boundary layers, laminar-turbulent transition, inlets, scramjet vehicles

16. SECURITY CLASSIFICATION OF:			**17. LIMITATION OF ABSTRACT**	**18. NUMBER OF PAGES**	**19a. NAME OF RESPONSIBLE PERSON**
a. REPORT	**b. ABSTRACT**	**c. THIS PAGE**			Steven P. Schneider
Unclassified	Unclassified	Unclassified	None	172	**19b. TELEPHONE NUMBER** *(include area code)* 765-494-3343

STREAMWISE VORTEX INSTABILITY AND HYPERSONIC BOUNDARY-LAYER TRANSITION ON THE HYPER-2000

A Thesis

Submitted to the Faculty

of

Purdue University

by

Shin Matsumura

In Partial Fulfillment of the

Requirements for the Degree

of

Master of Science in Aeronautics and Astronautics

December 2003

ACKNOWLEDGEMENTS

This research was funded by NASA Langley Research Center grant NAG1-02047, which was monitored by Scott Berry. A research problem of this level is by no means a one-person task. During his visit to Purdue University, Scott provided many useful and helpful discussions and opinions about the research. His assistance with the oil-flow visualization experiments is greatly acknowledged. Erick Swanson, a member of the hypersonic transition research group, developed the necessary tool-bit paths for machining the Hyper-2000 wind tunnel model. In addition, Prof. John Sullivan and his research assistants Jim Gregory, Chihyung Huang, and Hirotaka Sakue specializing in PSP/TSP provided help and training in the overall TSP experimental technique. Asai-san and Nakakita-san from the National Aerospace Laboratory of Japan also provided valuable advice and expertise throughout the years. The 14-bit CCD camera was generously loaned by The Boeing Company.

Shann and Craig, the remaining members of the hypersonic transition research group, also provided help throughout the years. Shann and Craig often tolerated my requests to help set up the facility, in addition to the once in a while tantrums I threw when things went wrong. The machinists at the Aerospace Sciences Laboratory Jim Younts, Robin Snodgrass, Madeline Chadwell, and Jerry Hahn spent many hours building parts and fixing hardware. They were great supervisors when I was learning to use the machines in the shop, tolerating my clumsiness and tendency to break tool-bits.

A big part of the moral support was provided by close friendships developed over the years. Luiz, Tom, Stephanie, Mikie, and Shannon often had to put up with my whining when I became burnt out, and especially when personal life became a disaster and distracted me from my work. Mom, Dad, Nene, and Bob also were always there for me with their love, sometimes being a constant source of annoyance, as a good parent ought to do. Although they do not know, Russell, Charlotte, and especially Sarah

provided so much support, comfort, and joy. Their seemingly close presence particularly late at night in Grissom made it possible to put in long work hours.

Finally, the major advising professor Dr. Steven Schneider, provided guidance ever since I was enrolled in AAE 333L in 1997. When I walked into the classroom the first day of classes I somehow knew, perhaps with my sixth sense, that Steve would have a major influence on my growth process during my years at Purdue. Steve has watched me grow from a teenager to an “almost” mature adult over these years, making him in some ways my alternate father. I realize, and acknowledge, that a significant part of my technical beliefs and knowledge was passed on directly from him.

TABLE OF CONTENTS

Page

LIST OF TABLES……vii

LIST OF FIGURES……..viii

ABSTRACT……...xv

1. INTRODUCTION ……1

1.1 Importance of Hypersonic Boundary Layer Transition……1

1.2 Current Transition Prediction Capability and Purpose of Research……..2

1.3 Background……...5

1.4 Research Objectives...……...9

1.5 Experimental Approach……..……10

2. EXPERIMENTAL APPARATUS……...13

2.1 The Boeing/AFOSR Mach-6 Quiet Tunnel...……13

2.2 Facility Modifications and Upgrades.……14

2.3 Freestream Flow Conditions..……16

2.4 Efforts Toward Achieving Quiet-Flow……..……18

2.5 Hyper-2000 Model….……22

2.6 Temperature-Sensitive-Paint Calibration Rig……25

3. TEMPERATURE-SENSITIVE-PAINT MEASUREMENT TECHNIQUE……...27

3.1 General Overview of Technique……27

3.2 Selected TSP..……29

3.3 Application Procedure……...……31

3.4 TSP Characteristics……33

4. EXPERIMENTAL SETUP AND DATA ACQUISITION TECHNIQUES……38

4.1 Experimental Setup……38

4.2 Effect of Using Multiple Images to Reduce Noise……40

Page

4.3 Effect of Image Acquisition Time…..…….43
4.4 Effect of CCD Camera Resolution……45
4.5 Oil-Flow Visualization Experiments.……49
5. IMAGE PROCESSING TECHNIQUE……54
5.1 Image Processing Overview..……54
5.2 Image Processing Approach..……55
5.3 Validation of Image Processing Approach……56
6. DATA REDUCTION MODEL……64
6.1 Heat Transfer Rate Model…..……64
6.2 Measurements and Treatment of the Insulator Thickness…..……66
6.3 Comparison of Mean Heat Transfer Rates to Hyper-X Measurements……..……71
6.4 RMS of the Spanwise Heat Transfer Rate Fluctuations……74
6.5 Spectral Analysis Technique..……78
7. STREAMWISE VORTEX GENERATOR DEVELOPMENT……82
7.1 Effect of Paint Layer Roughness…...……82
7.2 Boundary Layer Trips……84
7.3 Tape Strips Wrapped Around the Leading Edge…...……87
7.4 Effect of Leading Edge Roughness Strip Width……88
7.5 Effect of Leading Edge Roughness Strip Length…..……90
7.6 Final Roughness Strip Configuration ……94
8. RESULTS AND DISCUSSION……...95
8.1 Oil-Flow Experiment Results ……95
8.2 Temperature-Sensitive-Paint Heat-Transfer-Rate Images…..……..101
8.3 Spanwise Heat-Transfer-Rate Fluctuations...……..104
8.4 Spacing and Spreading of the Streamwise Vortices..……..110
8.5 RMS Heat-Transfer-Rate Fluctuation Growth……...……..113
8.6 Heat-Transfer-Rate Fluctuation Growth Using the Spectral Method……..118
8.7 Maximum Amplitude Ratio...……..129
9. CONCLUSION……...133

Page

10. RECOMMENDATIONS……...136
10.1 Imaging System…….……..136
10.2 Oil-Flow Visualization Experimental Method……...……..137
10.3 Temperature-Sensitive-Paint Experimental Method..……..137
10.4 Data Processing Method……..138
10.5 Model Improvement...……..139
10.6 Additional Experiments…….……..139
LIST OF REFERENCES…….140
APPENDIX……..150

LIST OF TABLES

Table Page

2.1 The conditions and resulting noise levels for different nozzle wall temperature distributions…...……22

6.1 Insulator thickness variation for several painting trials…….……67

LIST OF FIGURES

Figure		Page
2.1	Schematic of the Boeing/AFOSR Mach-6 Quiet Tunnel	13
2.2	Setup of the support structure for the optical bench	14
2.3	Assembly of the Lexan window enclosure	15
2.4	Freestream Mach number as a function of initial total pressure, for several throat geometries	17
2.5	Freestream noise levels as a function of initial total pressure, for several throat geometries	17
2.6	Temperature distribution along the nozzle	20
2.7	Normalized temperature distribution along the nozzle	20
2.8	Diagram of the nozzle throat region	21
2.9	Sideview of the centerline of the Hyper2000 forebody	23
2.10	Picture of the Hyper2000 forebody model	23
2.11	Image of the leading edge profile under an optical comparator	23
2.12	Leading edge thickness variation along the span	24
2.13	Picture of the temperature-sensitive paint calibration rig	25
3.1	General schematic of a TSP layer over a model surface	28
3.2	Schematic of the TSP experimental procedure	29
3.3	Comparison of the calibration data for Ru(bpy) and Ru(phen)	30
3.4	Comparison of calibration data for unpolished and polished temperature-sensing layers with Ru(phen)	33
3.5	Sensitivity of the TSP to pressure variation at three temperature values	34
3.6	Comparison of temperature calibrations performed at atmospheric and vacuum conditions	35
3.7	Variation of the luminescence intensity at three temperatures	36
3.8	Variation of the temperature sensitivity at three temperatures	37

Figure Page

4.1 Schematic of the experiment setup……38

4.2 Image of the experimental setup……39

4.3 Image of the experimental setup, with the LED light source turned on……39

4.4 Uncalibrated temperature image obtained using a single wind-off image, and using the average of five wind-off images……..……41

4.5 Spanwise distribution of the uncalibrated temperature using a single wind-off image, and using the average of five wind-off images…...……42

4.6 Streamwise distribution of the rms of the fluctuating component of the spanwise uncalibrated temperature, using a single wind-off image and the average of five wind-off images……42

4.7 Uncalibrated temperature images using wind-off images taken at different times from tunnel startup…...……43

4.8 Fluctuating component of the spanwise variation in the uncalibrated temperatures…...……44

4.9 Minimum temperature difference measurable with a 12, 14, and 16-bit CCD camera depending on the initial intensity counts……..……46

4.10 Comparison of the measured surface temperatures (deg. C) using a 12-bit and 14-bit CCD camera…….……47

4.11 Comparison of the measured spanwise temperature distribution at two streamwise stations using the 12-bit and 14-bit CCD camera……...……48

4.12 Streamwise distributions of the temperature fluctuation levels measured with the 12-bit and 14-bit camera…...……49

4.13 Image of the model with sprits of fluorescent oil applied…..……51

4.14 Oil-flow image clip taken immediately after tunnel startup..……52

4.15 Oil-flow image clip taken 6.5 sec. into the tunnel run……...……52

4.16 Oil-flow image clip taken immediately after tunnel unstart..……53

4.17 Oil-flow image clip taken 0.5 sec. after tunnel unstart……..……53

5.1 Locations of the registration marks used in the validation and optimization of the image processing method. All dimensions are in inches……57

5.2 Intensity ratio of the wind-off and wind-on image, showing the misalignment..……57

5.3 Intensity ratio of the wind-off and wind-on image, with the coordinates of the corresponding registration marks in the grid...……58

Figure Page

5.4 RMS Pixel misalignment after applying the image registration equations for the optimized mark locations.……60

5.5 Optimized registration mark locations for the 2nd order polynomial image registration equation...……61

5.6 Intensity ratio image corrected using the 2nd order polynomial with 41 registration marks for calibration…...……61

5.7 Comparison of the centerline intensity ratio distribution for the uncorrected and corrected images..……62

6.1 Thermal model of the heat transfer rate……..……64

6.2 A typical coating thickness grid constructed from raw measured data and from interpolation of the raw data…..……68

6.3 Heat transfer rate distributions computed with three different treatment of the insulator thickness……..……69

6.4 Comparison of the centerline mean heat transfer rate distributions on the Hyper-2000 compression ramps using various approximation of the insulator thickness…..……70

6.5 Comparison of the measured mean heat transfer rates on the Hyper-2000 to the measurements and laminar CFD data on the Hyper-X……71

6.6 Ratio of TSP images taken at no-flow condition, with a temperature of 28.4 deg. C and pressures at 0.05 and 127 psia…..……73

6.7 Comparison of the heat-transfer rates using a wind-off image taken at 0.05 and 127 psia to CFD data…...……74

6.8 Heat transfer rate distribution on the Hyper-2000 near the compression corners……75

6.9 Effect of averaging multiple columns to obtain the spanwise heat transfer rate distribution at representative streamwise stations……...……76

6.10 Variation of q'_{rms} for different number of columns averaged (N) to obtain the spanwise heat transfer rate distribution……77

6.11 Variation of the q'_{rms} along the centerline, with an averaging of 15 pixel columns……..……78

6.12 Power spectral density of the spanwise heat transfer rate fluctuations……..……79

6.13 Power density magnitude variation for different number of columns averaged……..……80

6.14 Power density and energy number distribution along the centerline.……81

Figure Page

7.1 Uncalibrated temperature image and the wind-off image taken with an unpolished insulator layer…..……83

7.2 Uncalibrated temperature image and the wind-off image taken with a polished insulator layer……..……83

7.3 Uncalibrated temperature image and the wind-off image taken with a polished insulator and TSP layer…...……84

7.4 Uncalibrated temperature image using triangular trips about midway on the first ramp and near the leading edge..……86

7.5 Uncalibrated temperature image using roughness dots placed about 0.015 in. from the leading edge…...……86

7.6 Schematic of the leading edge roughness strips……88

7.7 Uncalibrated temperature images for various roughness strip widths……...……89

7.8 Uncalibrated temperature images for various roughness strip lengths on the windward side……91

7.9 Uncalibrated temperature images with the roughness strips wrapped and unwrapped around the leading edge..……92

7.10 Uncalibrated temperature images for two roughness strip lengths on the leeward side...……93

7.11 Image of the leading edge roughness strips...……94

8.1 Oil-flow image at an initial unit Reynolds number of 1.67 million/ft……...……95

8.2 Oil-flow image at an initial unit Reynolds number of 2.20 million/ft……...……96

8.3 Oil-flow image at an initial unit Reynolds number of 2.72 million/ft……...……96

8.4 Effect of initial total pressure on the separation line.……97

8.5 Oil-flow image near the first compression corner using the oil-sprit technique at a unit Reynolds number of 1.67 million/ft……98

8.6 Oil-flow image near the first compression corner using the oil-sprit technique at a unit Reynolds number of 2.72 million/ft……99

8.7 Streamwise-averaged spanwise fluctuations seen in the oil-flow images…..…..100

8.8 Power spectral density of the spanwise fluctuations seen on the third compression ramp in the oil-flow images…..……..100

8.9 Effect of initial total pressure on the heat-transfer-rate images. The cases shown used 17 strips (0.16 inch spacing) with three layers (2.25 mils)……..102

Figure Page

8.10 Effect of leading edge roughness spacing. The cases shown used three layers (2.25 mils) of roughness strips, all at a total pressure of 129.5 psia (2.72 million/ft)……..……..103

8.11 Effect of leading edge roughness thickness. The cases shown used 17 strips (0.16 inches spacing), all at a total pressure of 129.5 psia (2.72 million/ft)……..……..104

8.12 Comparison of the spanwise heat-transfer-rate distributions on the three compression ramps….……..105

8.13 Comparison of the spanwise heat-transfer-rate distribution on the 2nd compression ramp against the initial total pressure...……..106

8.14 Comparison of the spanwise heat-transfer-rate distribution on the 2nd compression ramp against the roughness spacing….……..107

8.15 Comparison of the spanwise heat-transfer-rate distribution on the 2nd compression ramp against the roughness thickness...……..107

8.16 Comparison of the normalized fluctuating component of the spanwise heat-transfer-rate distribution on the 2nd compression ramp against the roughness spacing…...……..108

8.17 Comparison of the magnitudes of the fluctuations normalized by the mean heating value on the 2nd compression ramp...……..109

8.18 Power spectral density of the fluctuating component of the spanwise heat-transfer-rate distributions……...……..110

8.19 Spacing of the streamwise vortices against the roughness spacing...……..111

8.20 Spanwise spreading of the streamwise vortices on the compression ramps from the roughness….……..112

8.21 Spreading rate of the streamwise vortices against the roughness spacing…..…..112

8.22 Streamwise growth of the RMS heat-transfer-rate fluctuations. All cases shown are for the cases with 15 roughness strips (0.18 inch spacing)……..…..114

8.23 Streamwise growth of the RMS heat-transfer-rate fluctuations normalized by the value of the maximum fluctuation. All cases shown are for the cases with 15 roughness strips (0.18 inch spacing)...……..115

8.24 Streamwise growth of the RMS heat-transfer-rate fluctuations normalized by the value of the maximum fluctuation on the second compression ramp. All cases shown are for the cases with 15 roughness strips (0.18 inch spacing)….……..116

Figure Page

8.25 Streamwise growth of the RMS heat-transfer-rate fluctuations normalized by the value of the maximum fluctuation on the third compression ramp. All cases shown are for the cases with 15 roughness strips (0.18 inch spacing)…..……..117

8.26 Streamwise variation of the power spectral density. All cases shown are with 15 roughness strips (0.18 inch spacing) of maximum thickness (2.25 mils) applied…..……..117

8.27 Streamwise growth of the power. All cases shown are for the cases with 15 roughness strips (0.18 inch spacing)…….……..119

8.28 Streamwise growth of the power normalized by the maximum power. All cases shown are for the cases with 15 roughness strips (0.18 inch spacing).…..119

8.29 Streamwise growth of the amplitude ratio. All cases shown are for the cases with 13 roughness strips (0.21 spacing)…….……..120

8.30 Streamwise growth of the amplitude ratio. All cases shown are for the cases with 15 roughness strips (0.18 spacing)…….……..121

8.31 Streamwise growth of the amplitude ratio. All cases shown are for the cases with 17 roughness strips (0.16 spacing)…….……..121

8.32 Streamwise growth of the amplitude ratio. All cases shown are for the cases with 19 roughness strips (0.14 spacing)…….……..122

8.33 Streamwise growth of the amplitude ratio. All cases shown are for the cases with 21 roughness strips (0.125 spacing)…...……..122

8.34 Variation of initial disturbance amplitudes……..123

8.35 Streamwise growth of the power normalized by the maximum power. All cases shown are for the cases with 15 roughness strips (0.18 inch spacing).…..123

8.36 Streamwise growth of the power normalized by the maximum power on the second compression ramp. All cases shown are for the cases with 15 roughness strips (0.18 inch spacing)..……..124

8.37 Streamwise growth of the power normalized by the maximum power on the third compression ramp. All cases shown are for the cases with 13 roughness strips (0.21 inch spacing)..……..125

8.38 Streamwise growth of the power normalized by the maximum power on the third compression ramp. All cases shown are for the cases with 15 roughness strips (0.18 inch spacing)..……..125

8.39 Streamwise growth of the power normalized by the maximum power on the third compression ramp. All cases shown are for the cases with 17 roughness strips (0.16 inch spacing)..……..126

Figure Page

8.40 Streamwise growth of the power normalized by the maximum power on the third compression ramp. All cases shown are for the cases with 19 roughness strips (0.14 inch spacing)..……..126

8.41 Streamwise growth of the power normalized by the maximum power on the third compression ramp. All cases shown are for the cases with 21 roughness strips (0.125 inch spacing)……..127

8.42 Streamwise growth of the power normalized by the maximum power on the third compression ramp. All cases shown are for the cases at the highest total pressure of 129.5 psia (2.72 million/ft)..……..128

8.43 Streamwise growth of the power normalized by the maximum power on the third compression ramp. All cases shown are for the cases at the highest total pressure of 129.5 psia (2.72 million/ft)..……..128

8.44 Maximum amplitude ratios on the second compression ramp……...……..130

8.45 Streamwise coordinate of the maximum amplitude ratio on the second compression ramp…..……..131

8.46 Maximum amplitude ratios on the second compression ramp……...……..131

8.47 Streamwise coordinate of the maximum amplitude ratio on the second compression ramp…..……..132

ABSTRACT

Matsumura, Shin. Master of Science in Aeronautics and Astronautics, Purdue University, December, 2003. Streamwise Vortex Instability and Hypersonic Boundary-Layer Transition on the Hyper-2000. Major Professor: Steven P. Schneider.

Despite the closely coupled multidisciplinary design of hypersonic airbreathing vehicles, the boundary layer transition mechanisms that are important on the forebody ahead of the scramjet inlet are not well understood. Transition induced by the growth of streamwise vortices is studied on a scramjet forebody geometry similar to the Hyper-X. Flow visualization methods are developed for this application in Purdue's Boeing/AFOSR Mach-6 Quiet Tunnel. Fluorescent oil-flow visualization is used to complement the instability measurements obtained with temperature-sensitive-paints. The characteristics of the separation zone near the first compression corner are visualized with oil-flow experiments. These experiments also reveal the presence of regularly spaced streamwise vortices on the compression ramp even in the absence of controlled disturbance generators. The growth and decay of these vortices are inferred from the heat-transfer rates measured using temperature-sensitive-paints. The streamwise vortices are enhanced in a controlled and repeatable manner by wrapping tapes around the leading edge. The vortices grow significantly on the second compression ramp and then decay, suggesting transition onset. The disturbance growth seems to show a systematic trend with unit Reynolds number, although this trend was not consistently seen for all cases. For some of the cases, the disturbances showed the largest growth when the roughness spacing was close to the vortex spacing seen in the oil-flow images.

1. INTRODUCTION

1.1 Importance of Hypersonic Boundary Layer Transition

Boundary layer transition on hypersonic vehicles has three main direct effects: increased heating, induced forces on the vehicle including increased friction drag, and influences on optical-systems aberrations. The windward heating on the space shuttle has been well documented [1-3]. Increased heating requires more thermal-protection-system (TPS) material, and increases the weight of the vehicle [4]. TPS weight trades pound for pound with payload weight, which is a small fraction of the overall vehicle mass to begin with. Increased heating also affects the operational and maintenance cost. At present tiles are used on the shuttle, and these are very expensive to maintain. This has led to the proposed use of a smooth, reusable metallic windward surface for the X-33 [5]. This has the potential of reducing the maintenance cost and shortening turnaround time, but will require much more reliable and accurate transition prediction and control methods to avoid overheating, because of the lower maximum temperature limit of metallic TPS.

Turbulent boundary layers also increase the friction drag. For accurate design and predictions of the re-entry trajectory and cross-range, which affects the safety and mission-abort options, the aerodynamic forces on the vehicle must be accurately predicted. For hypersonic airbreathing vehicles such as the Hyper-X [6] and the National Aerospace Plane and its derivatives [7, 8], prediction and reduction of drag is crucial, because of the challenges of obtaining a net thrust with scramjet propulsion systems ([9] pg. 26). Asymmetric boundary layer transition along the vehicle centerline can also induce rolling and yawing moments on the vehicle. This was experienced with the shuttle, and has raised concerns about the amount of propellant needed to enable the reaction control system (RCS) thrusters to compensate [10].

Optical systems onboard interceptors and reconnaissance vehicles are also affected by boundary layer transition [11, 12]. To prevent the performance of the seeker

windows from degrading, the fluid flow over the window must be accurately modeled and controlled. Two key issues are film cooling and transition, both of which influence the flow-field structure. Not only does transition affect the performance of the seeker, it affects the structural integrity of the windows by increasing the heat transfer rate, which in turn induces tensile forces due to thermal expansion of the windows. Accurate transition-location prediction is crucial for the design of a robust seeker system.

The National Aerospace Plane (NASP) program provides one of the best examples of the influence transition can have on a vehicle design. The NASP is a completely different type of vehicle from previous hypersonic vehicles such as re-entry capsules and the shuttle, since it must accelerate at hypersonic conditions using airbreathing propulsion. Not only does transition increase drag and heating, it changes the flow conditions at the engine inlet, affecting the engine performance as well. During the NASP program, the transition location was estimated to vary from 20-80% along the body, depending on the transition correlation used. When all the factors that are affected by this variation in transition location were taken into account, the gross take off weight of the vehicle varied by a factor of two or more [13]. A few years later, this uncertainty in the transition location and lack of a reliable prediction method became one of the main reasons for canceling the NASP program [14]. This clearly shows that for these classes of vehicles, transition can have a significant effect on the vehicle design, and must be considered early in the design stage using a reliable and robust prediction method.

1.2 Current Transition Prediction Capability and Purpose of Research

Unfortunately none of the transition prediction methods available today are reliable or accurate to the desired level. The techniques that are used for hypersonic speeds are all based on empirical correlations, and not on the flow physics. Because of this, they only work for limited or similar cases, and extrapolation from wind tunnel to flight conditions is very risky for new vehicle concepts and geometries. Mechanism-based methods include linear stability theory and the e^N method [15, 16], which relates the integrated growth of the instability waves to the breakdown of the waves, but the N-

value for transition can still have a significant scatter [17]. This method has not been used widely at hypersonic conditions either. Direct Numerical Simulation (DNS) can compute all of the flow physics without any correlations or modeling, but is too expensive for flows at practical Reynolds numbers [18]. Another difficulty with DNS is that it requires detailed knowledge of the freestream disturbances and the receptivity modes at work creating the instability waves. This information is usually not known and is treated in an ad-hoc fashion [19]. The Parabolized Stability Equations (PSE), on the other hand, is a very promising technique. PSE also requires the initial disturbances as inputs, but it is capable of modeling several instability modes, secondary instabilities, wave and mode interactions, receptivity, breakdown, and is also the only stability model that can truly be formulated for three-dimensional disturbances in a three-dimensional mean flow [20-23] at a reasonable computational cost.

As with any computational and simulation tools, any transition prediction method including the PSE will require development, validation, and calibration based on flight and/or experimental data. The relevant instability modes must be known; these must be sorted out through a series of experiments. This is however very difficult for hypersonic flight conditions, because flight-testing is extremely expensive, and instrumentation is limited. In addition, hypersonic boundary-layer transition and stability experiments performed in conventional hypersonic tunnels suffer from ambiguities due to high levels of freestream noise, which is mostly caused by the turbulent boundary layer along the nozzle wall [24]. At high Mach numbers, this turbulent boundary layer radiates noise in the form of eddy Mach wave acoustic radiation into the test section and onto the flow around the test model. This has a significant effect on the stability of the boundary layer, and can not only change the quantitative results; it can change the trends in boundary layer stability and transition [25-27]. For example, linear stability theory along with the e^N method for transition location correlation says that transition will occur earlier on a 5º half angle cone than on a flat plate at Mach 3.5. Experiments done at NASA Langley Research Center (LaRC) under noisy conditions showed that transition occurred earlier on a flat plate, whereas under quiet conditions, linear stability theory was verified [28].

The Boeing/AFOSR Mach 6 Quiet Tunnel (BAM6QT) at Purdue University was designed and built for studying high-speed boundary layer transition under quiet conditions to obtain conclusive data regarding boundary layer stability and transition. Construction of the tunnel was finished during the spring of 2001, and although the tunnel is not running quiet yet, results from tunnel shakedown experiments are being used to make modifications to the tunnel [29-32]. If the tunnel runs quiet, this would be the only hypersonic quiet tunnel in operation, besides the Mach 6 quiet tunnel at LaRC, which at the moment is not operational [33]. In addition, the instrumentation and measurement techniques are being developed at the same time. This includes an automatic vertical traverse system for pitot-tubes and hot-wires [34], and temperature and pressure sensitive paint systems (TSP and PSP) for surface measurements [35, 36].

The Hyper-X is representative of the vehicle geometry that is of interest to the hypersonics community. A geometry that is "representative" of the Hyper-X class of vehicles, called the Hyper-2000, which is publicly releasable, was obtained from LaRC [31]. Experimental research aimed at the identification and physical understanding of possible instability modes and transition mechanisms should be applicable for a broad range of vehicle geometries that are similar to the Hyper-X. This data can aid the computational and theoretical developers working to develop transition prediction methods for the vehicle designers, and also would be useful to the designers directly, because it would give them an understanding of the physics governing the performance of various designs. However this present research would be performed under noisy tunnel conditions, and because of that the data might not be truly unambiguous as desired, as stated previously. However, comparing the data obtained from a noisy condition to future experiments performed under quiet conditions might reveal some important noise effect issues, which would be useful in interpreting data taken in conventional tunnels.

1.3 Background

The Hyper-2000 is a geometry that is typical of hypersonic vehicles powered by a scramjet propulsion system with a two-dimensional compression surface. For such geometries several instability modes and their interactions might be important. One of them is the first and second modes, or the Mack modes [37]. The first mode is a vorticity disturbance similar to the Tollmien-Schlicting waves seen at low-speed conditions, and the second mode is an acoustic disturbance trapped within the boundary layer. These could be measured using hot-wires, by introducing controlled disturbances using glow and laser perturbers developed in the Mach 4 Ludwieg tube [38, 39]. Cross-flow instability is another mechanism that might occur. It occurs from an inflection point in the spanwise direction within the boundary layer, caused by a spanwise pressure gradient [40]. Oil flow experiments performed on the Hyper-X geometry clearly show a small spanwise spreading of the streamlines [41]. Another possible instability mode is the Görtler mode, which arises from centrifugal forces acting on the flow along curved surfaces [42]. Although the main compression surface of the Hyper-2000 is composed of three flat surfaces and two compression corners, the corners and the possible separation bubble at the corners may act as surface curvature. If a separation bubble forms at the corners, this would give rise to a shear-layer instability as well, which would be similar to the classical inviscid instability of Kelvin-Helmholz type.

The stationary, as opposed to traveling cross-flow and Görtler instabilities, involve the growth of stationary streamwise vortices, where in cross-flow mode the vortices are co-rotating and in Görtler mode they are counter-rotating. In cross-flow the vortices are generated from the inflectional velocity profile in the spanwise direction, whereas in Görtler mode a centrifugal instability generates the vortices. The instability waves grow from initial perturbations such as surface roughness, freestream turbulence, acoustic waves, etc. The formation of vortices from these perturbations is governed by receptivity mechanisms [43]. Because of multiple instability modes that might be present on the Hyper-2000 geometry, there may also be coupling and interaction effects between the different modes. One possible hypothesis might be that streamwise vortices are amplified on the first surface by the cross-flow instability, and then the Görtler and/or the

shear-layer instability near the corner might trigger a breakdown, leading to transition to turbulent flow. In this hypothesis, the cross-flow, Görtler, and possibly the shear-layer instability all have some role in the transition process. Another possibility is that streamwise vortices are generated on the first surface in the absence of cross-flow instability, and are again amplified at the compression corner, with the final breakdown occurring at the reattachment point. In this hypothesis, cross-flow instability would not have any importance. Whatever the case may be, it seems like the streamwise vortices and the compression corners might have an important role on the transition process on these geometries.

The flow near a compression corner is a classical shock-boundary layer interaction problem, where the incoming boundary layer interacts with the inviscid flow and the shock. A variety of geometries with separation such as forward and backward facing steps, sharp and curved corners, and shock reflections, were tested at subsonic and supersonic Mach numbers to categorize the qualitative flow characteristics based on the boundary layer state [44]. The flows are categorized as laminar, transitional or turbulent depending on whether transition occurs downstream of reattachment, between the separation and reattachment point, or upstream of the separation point. Depending on the flow conditions and the corner angle, this interaction is strong enough to modify the established flow significantly. Few theories and simple analytical methods have been developed for this problem, and are compared to experimental data in reference [45]. Overall the flow can be adequately predicted if the flow remains attached. However, as the separation region becomes larger and as transition starts to become an issue, the simple theories fail.

Lewis et al. measured the pressure distribution along a 10.25 deg. corner at a freestream Mach number of 6.06 [46]. This angle is sufficiently large to cause separation at this Mach number unless the Reynolds number based on the model length is made sufficiently small, on the order of 150,000. The pressure distribution along the wall gradually increases from the first plate to the second plate, with some overshoot. As the Reynolds number is increased the influence on the pressure distribution upstream of the

corner increases. At some point the Reynolds number becomes large enough to cause transition, which now reduces the upstream influence and the pressure overshoot.

Chpoun investigated the effects of transition for compression angles of 10, 20, and 30 deg. at Mach 4.96 and Reynolds number of a million [47]. Flow visualization showed separation to occur for all three angles. The Reynolds number was varied by changing the length of the flat-plate portion of the model, upstream of the corner. For the 10 deg. case, the flow remained laminar, and increasing the Reynolds number moved the separation point upstream. For the 20 and 30 deg. cases, transition occurred and the separation zone showed an opposite trend from the 10 deg. case. Qualitatively these conclusions are consistent with those of Lewis et al. The pressure distribution for the 20 deg. case was qualitatively similar to that of Lewis et al., where the pressure increases from the value on the flat plate to the peak pressure at the reattachment point downstream of the corner. However for the 30 deg. case, the wall pressure distribution had a plateau region, followed by an inflection point.

Cassel et al. performed computations for a range of smaller compression angles at supersonic conditions using the triple-deck theory [48]. The appearance of the plateau region in the pressure distribution for larger compression angles is shown here as well. Skin friction distributions are given. These show that the separation point moves upstream and the reattachment point moves downstream as the corner angle is increased. In addition stability computations were performed using harmonic disturbances. A temporal instability was observed at the corner, which is presumably caused by the inflectional velocity profile within the recirculation zone. The existence of this instability shows the possibility that Tollmien-Schlicting instability might be important for compression corners when a separation is present at supersonic conditions, which would imply that the second mode might be important as well at hypersonic conditions.

On the other hand, Balakumar et al. performed computations on a 5.5 deg. corner at a Mach number of 5.373 and unit Reynolds number of 5.64 million/ft, which corresponds to a set of experiments done as part of the Hyper-X program [49]. The mean flow was computed first with the three-dimensional Navier-Stokes equation, and then two and three-dimensional disturbances were introduced. Again the mean flow pressure

distribution contains a plateau region due to a separation bubble. The results focus on the growth of the second mode, and show that the unstable frequencies upstream of the corner are actually neutral in the separation region. Waves with those frequencies become unstable again downstream of the separation region. In other words, if the incoming boundary layer into the corner is laminar, then the unstable second mode waves approaching the corner can only cause transition downstream of the reattachment point, and not within the separation zone. This however does not mean that second mode waves are not important over the separation region, because frequencies which are stable upstream of the corner may become unstable over the separation region.

Kosinov et al. however draw conclusions similar to Cassel et al. [50]. They used a double-cone model with half-angles of 5 and 10 deg. The freestream Mach number was 2 and the unit Reynolds number was about 2 million per ft. Artificial disturbances were introduced using a spark discharge, and the instability waves were measured using hot-wires. The growth of 20 kHz waves is shown, and a conclusion is drawn that in separated corner flows Tollmien-Schlicting waves are the disturbances determining the transition. An oil flow image is also included, which clearly shows the location of separation and reattachment. The image however also shows striation patterns immediately upstream of the separation point and immediately downstream of the reattachment point. These might be streamwise vortices of some sort, which might be playing a role in triggering transition, or they might simply be the streamline traces. It is difficult to tell because of the poor quality of the image.

Several independent workers have observed these striation patterns in compression corner flows. Simeonides et al. provides a comprehensive list of several experiments on compression corners at hypersonic Mach numbers [51]. They show that there is a consistent relation between the occurrences of these striations and transition in the reattachment region, with the striations terminating when the transition process is completed. This is typical of instability-driven transition processes, where the instability waves become washed away once turbulent flow is established. The experiments of Nakakita et al. were done on a 30 deg. corner at Mach 10 and Reynolds number of 160,000, for the purpose of PSP technique development [52]. Their pressure distribution

image shows streaks of high-pressure regions in the reattachment region as well. The striation patterns actually are not limited to compression corner flows, as Ginoux observed them for other separated flows, flat plates, and delta wings at Mach numbers between 1.5 and 7 [53]. Experiments were also done on a hollow cylinder at zero AOA. The presence of the striations even for this case shows that the streaks are not necessarily cross-flow vortices. In fact, Ginoux placed strips of tape along the leading edge of various two-dimensional models at regular spacings, and showed unambiguously that the peaks and valleys in the flow visualization and spanwise distribution of pitot pressure measurements could be correlated to the location of the tapes on the leading edge.

De Luca et al. systematically studied the striation patterns and their relation to the leading edge geometry using compression corners of 10-25 deg, at Mach 7.14 and unit Reynolds numbers of 2.3-7.3 million per ft. [54]. The leading edge of the model had a sinusoidal pattern, with a wavelength and amplitude of 2 and 0.5 mm respectively. The resulting striation patterns were imaged using an infrared imaging system. The wavelength of the periodic fluctuation of the spanwise heat transfer rate distribution decreased as the freestream unit Reynolds number was increased. This shows that the dominant wavelength of these streamwise vortices was dependent on the flow conditions. The experiments were repeated after a significantly long time, so that the tunnel conditions would be slightly different, but the striations were remarkably repeatable, which is an important aspect when using controlled disturbances for instability and transition research.

1.4 Research Objectives

Streamwise vortices clearly seem to have a major role in determining the transition location in compression corner flows, which might be related to cross-flow or Görtler vortices, or they might be a new instability mode for these geometries. The instability mechanisms of these vortices can only be speculated upon this time, because no validated theories or computational models exist for the Hyper-2000 geometry at

hypersonic conditions. Thus measurements of the growth and decay of these streamwise vortices at various conditions would be new experimental discoveries.

In the past, the striations have been measured using various techniques, ranging from conventional hot-wires and pitot-pressure probes, to flow visualization with oil-flows, sublimation, and infrared imaging systems. Due to the low cost and set-up time required, the TSP technique seems to be very promising for this application. Streamwise vortices are important in other geometries as well, so the measurement technique is not limited solely to the research using the Hyper-2000. The technique would also be useful for other high-speed tests in the future. A secondary objective of this research is thus to develop the TSP measurement technique, data acquisition and processing system for this particular facility.

References [55-57] give comprehensive descriptions of the TSP technique, and will not be repeated here. TSP has been used for various flow visualization and quantitative heat-transfer-rate measurements at high-speed conditions, such as forward and backward facing steps at supersonic conditions [58], cones and wing-body geometries in shock tunnels [59, 60], and boundary layer transition detection on wings and airfoils [61-63]. Because of the large number of experiments performed with TSP over the years, developing the technique for this facility should be relatively straightforward. However, all experiments to date have been for flows where the range of heat transfer rate is relatively large, which simplifies the problem. For the present research, the challenge is to measure the small-amplitude vortices and especially their growth rates, which will only be a small percentage of the mean heating rate.

1.5 Experimental Approach

The research is divided into three main steps. The measurement and post-processing techniques must first be developed, along with any modifications and/or upgrades necessary to the facility. Measurement technique development includes tasks such as the selection and characterization of the TSP, image-processing methods, and data reduction models. Validation of the technique is desired as well, although this is of

secondary importance because TSP's can be considered a validated technique at this point with all the past work that has been accomplished.

Second, qualitative measurements on the Hyper-2000 are necessary, to obtain an overall understanding of the flow field. The effect of a separation bubble on the flow characteristics was reviewed in the previous section. Clearly this must be investigated, even if it is only by qualitative flow visualization means. Stollery [64] gives a very simple equation for incipient separation for hypersonic compression corners:

$$M_\infty \alpha_i \approx 80 \chi^{1/2} \tag{1.1}$$

where M_∞ is the freestream Mach number, α_i is the compression angle at incipient separation, and χ is the viscous interaction parameter defined as:

$$\chi \equiv M_\infty^{\,3} \Big/ \sqrt{\mathrm{Re}_L} \tag{1.2}$$

where Re_L is the length Reynolds number. Using these relations, separation may or may not occur on the Hyper-2000 depending on the unit Reynolds number. Effects of wall roughness should also be investigated. It is known that wall roughness tends to promote Görtler instability [66]. If streamwise vortices are seen on the Hyper-2000, these may be Görtler vortices, and the wall roughness must be quantified along with the instability growth rate.

The method to generate streamwise vortices should also be investigated briefly. The previous discussions showed that the leading edge geometry has a significant affect on the streamwise vortex formation, so the simplest way to generate streamwise vortices of different amplitudes and wavelengths is probably to use strips of tape near the leading edge following Ginoux's technique. However, the Hyper-X uses boundary layer trips located about half way down the first surface, and striation patterns are seen in the flow visualization as well [41]. Controlled roughness attached to the surface away from the leading edge is another possible method to introduce streamwise vortices. The purpose

of this research is not to investigate the physics of boundary layer trips, but it might be useful for understanding transition caused by trips for these configurations.

With the vortex generator of choice finalized, the growth rate of streamwise vortices will be measured in the final part of the research. The task here will be to quantify the characteristics of the streamwise vortices for several conditions. Some important characteristics include the growth rates, the dominant wavelength, and the spreading rate in the presence of cross-flow. A database for several flow conditions and vortex generator conditions will be established so that comparisons can be made to understand the trends.

2. EXPERIMENTAL APPARATUS

2.1 The Boeing/AFOSR Mach-6 Quiet Tunnel

The Boeing/AFOSR Mach-6 Quiet Tunnel (BAM6QT) is a Ludwieg-tube blow-down wind tunnel. A general schematic of the facility is shown in Figure 2.1, which is taken from Ref. [66]. The air storage tank is a 122 ft. driver pipe that connects directly to the contraction without gates, valves, or screens. This helps to maintain a smooth flow into the contraction. Downstream of the driver pipe is the contraction and nozzle, with a boundary layer bleed at the throat to start a new boundary layer for the supersonic expansion. The nozzle is designed to maintain a laminar boundary layer as long as possible; reducing the Görtler instability by using a gentle wall curvature, reducing the Tollmien-Schlicting instability through non-uniform heating, and eliminating cross-flow instability with an axisymmetric design [67].

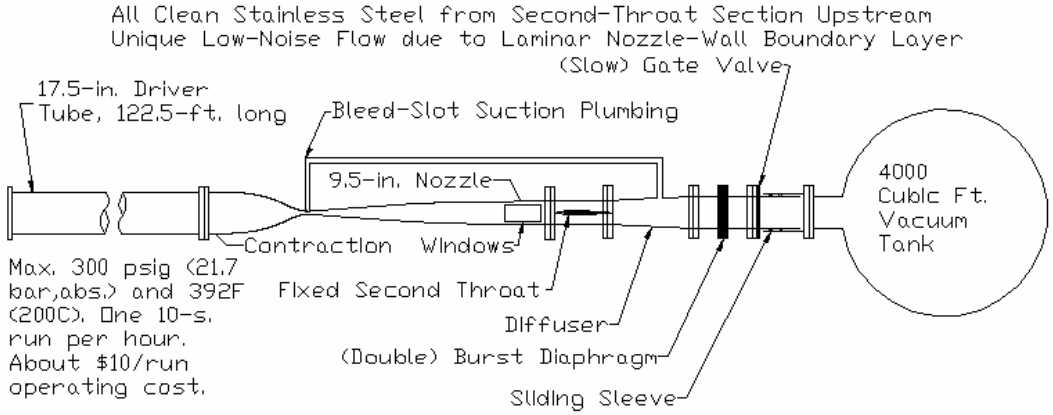

Figure 2.1. Schematic of the Boeing/AFOSR Mach-6 Quiet Tunnel, from Ref. [66].

In addition the majority of the nozzle is polished to a mirror finish to meet the roughness Reynolds number requirement of no more than about 10-12 to avoid roughness effects [68]. The double diamond wedge downstream of the nozzle creates a second throat, which is also where the model sting is supported. The tunnel is started using the double

burst diaphragm, which initially separates the vacuum tank from the tunnel. More details of the mechanical design are reported in Refs. [29, 69-71]. Also included are test results of components, and measurements of the nozzle coordinates.

2.2 Facility Modifications and Upgrades

A 7x14 inch Plexiglas window was installed to allow optical access for TSP and other image-based measurement techniques. In addition, a 2x10 ft. optical breadboard was installed underneath the test section. The optical bench was placed on a rail system with a precision traverse so that the position could be adjusted. The rail is supported on pneumatic vibration isolators, both of which were adapted from the older Mach-4 tunnel [72]. The new setup for the BAM6QT is shown in Figure 2.2. Also, an enclosure to cover the window was assembled over the optical bench, shown in Figure 2.3. The window can be seen on the left in this image.

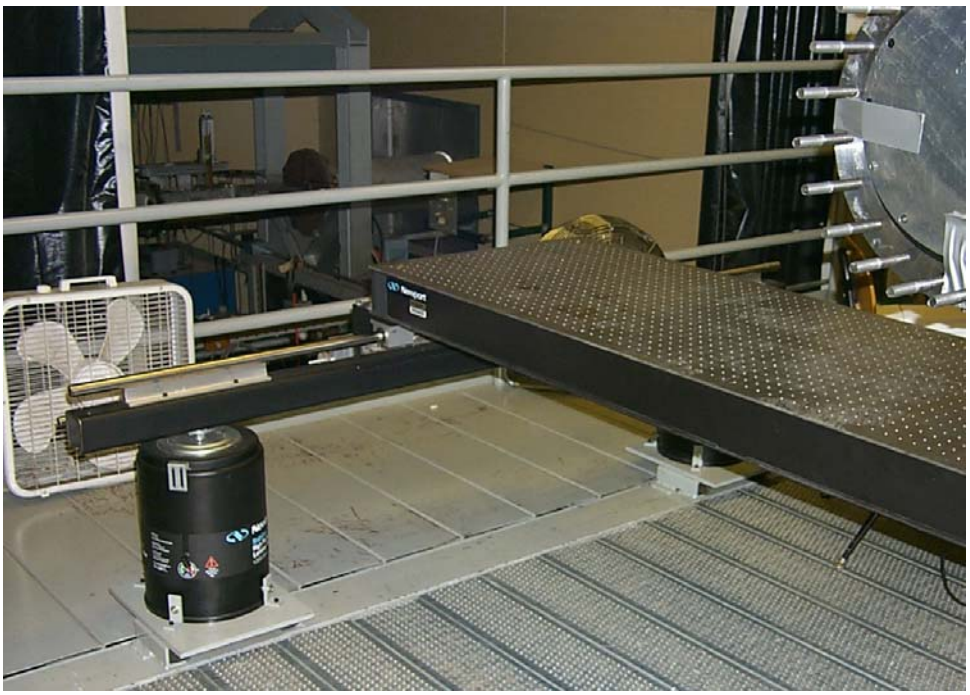

Figure 2.2. Setup of the support structure for the optical bench.

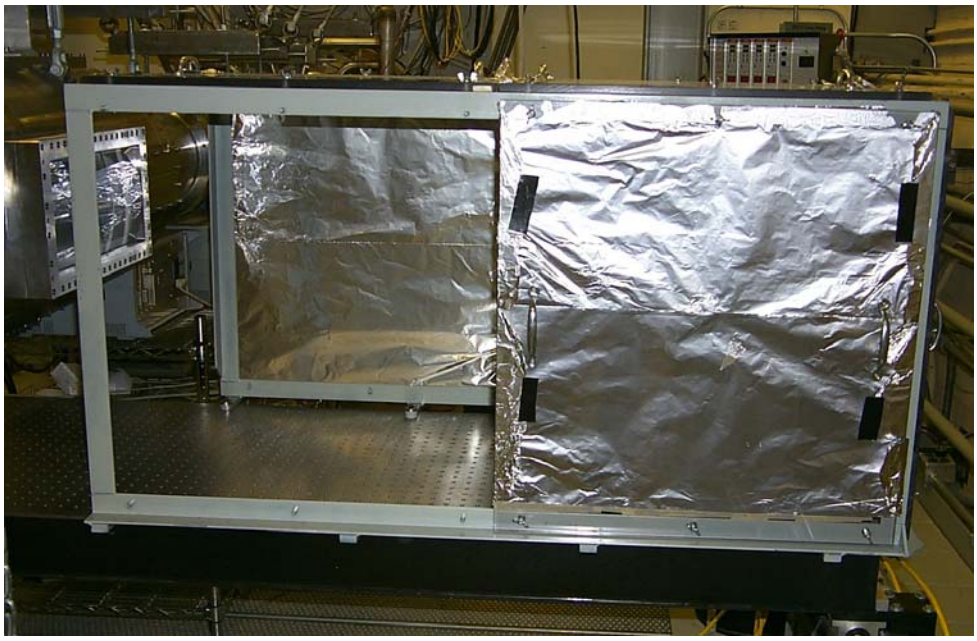

Figure 2.3. Assembly of the Lexan window enclosure.

The enclosure consists of a steel frame, with seven Lexan panels that can easily be removed. This enclosure served to protect the window from becoming scratched, and as a redundant safety precaution in the unlikely event the window shatters under pressure.

One drawback of the present Ludwieg tube is that the test section must be pressurized with the driver pipe to the initial total pressure before the run. Any windows installed must withstand this load. For this tunnel, the internal window surface must be curved to match the tunnel wall contour to avoid large separations, and the external surface must be curved so that image distortion is minimized. These requirements present a non-trivial mechanical design, which was analyzed with finite-element methods (FEM). For this window design a three-dimensional FEM analysis showed that for a 150 psi operating load, a safety factor of 4.7 could be achieved [73]. The window was installed using an installation jig, and pressure tested to 230 psia using nitrogen bottles, 1.5 times the nominal operating load [74].

The Plexiglas window is mounted in an aluminum casing. There is a small gap of about 30-80 mils between the window and the casing, which is filled with dental plaster as gasketing material. The deflection of the window due to the pressure load apparently cracked the plaster, which was sucked into the tunnel during the initial runs with the

windows installed. The loose dental plaster in the gap was carefully removed, and the deeper portions of the gap, of a depth more than an inch, were refilled with Orthocast Inc.'s Orthodontic Plaster. Twice the quoted amount of water was used to make the plaster flow into the small gap. This also softened the cured plaster, which should help it to withstand the deflection of the window without cracking. The remainder of the gap was filled with Dow Corning's 734 Flowable RTV Silicone. A layer of white Dow Corning 732 RTV Sealant was used on top in an attempt to create a smooth surface to match the contour of the window and casing. The window has been operational since then without any problems. Details of the gap filling materials considered, filling material testing procedure, and the final procedure are documented in Ref. [75].

2.3 Freestream Flow Conditions

Quiet flow continues to be sought; several modifications have been made to the throat and boundary layer bleed geometry in an attempt to achieve it. The preliminary experiments on the Hyper-2000 have been made using several tunnel configurations, which all result in slightly different flow conditions. Thus a single value cannot be placed on the flow conditions (such as the Mach number) to represent all of the experiments that have been performed. Figures 2.4 and 2.5 show the freestream Mach number and noise levels on the centerline (±1/16 in.) as a function of the initial total pressure using several throat geometries [31]. The measurements were taken between 84.16-84.63 in. downstream from the throat. The reader is referred to the reference for the descriptions of the eleven cases shown here. For all cases the Mach number is between 5.6 and 6. A single data point at a Mach number 4.8 is shown at a total pressure of about 8 psia, which is probably caused by separation in the nozzle. The noise levels are typical of conventional wind tunnels, of about 1-5 % of the mean.

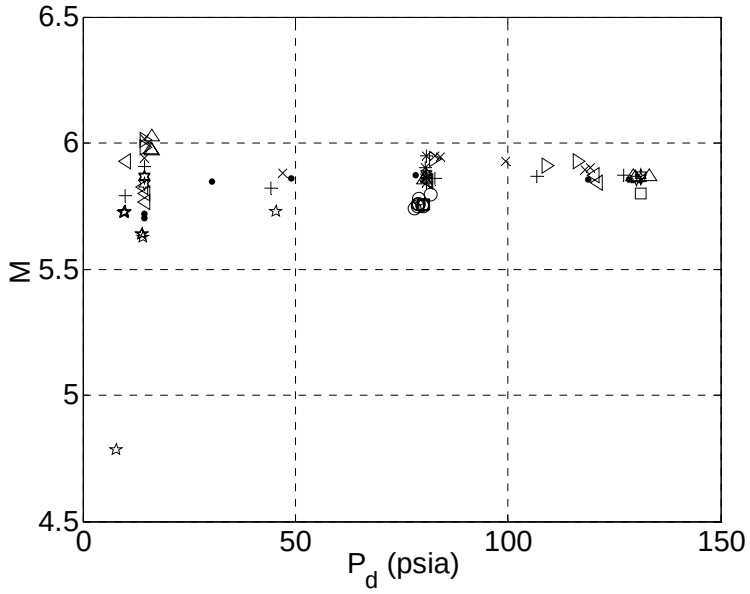

Figure 2.4. Freestream Mach number as a function of initial total pressure, for several throat geometries [31].

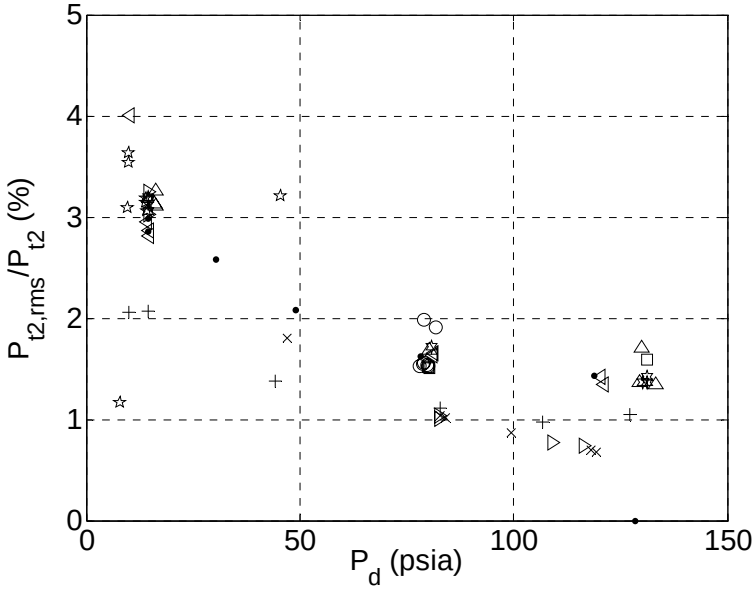

Figure 2.5. Freestream noise levels as a function of initial total pressure, for several throat geometries [31].

For all experiments the total temperature was nominally 160 °C, and the total pressure varied between one and ten atmospheres. Using a Mach number of 6 as a representative value, the unit Reynolds number ranges from about 0.3-3.2 million/ft. For the 11.78-inch long Hyper-2000 model, this corresponds to model length Reynolds

number of about 0.29-3.1 million. The tunnel run lasts 8-10 sec., depending on the bleed configuration at the throat and the initial total pressure. During that time the total pressure and temperature decrease quasi-statically in a stair-step manner, caused by the reflection of the expansion wave in the driver pipe, resulting in a series of 0.2 sec. steady-state flow conditions [30]. The total temperature variation during the run is modeled using the standard isentropic relation, shown in Equation 2.1.

$$\frac{T_0}{T_{0,i}} = \left[\frac{P_0}{P_{0,i}} \right]^{\frac{\gamma-1}{\gamma}} \tag{2.1}$$

Here, γ is the ratio of specific heats, and T_0 and P_0 are the total temperature and pressure respectively, with the subscript "i" denoting the initial value prior to tunnel startup. This relation has also been used for the Mach-4 tunnel [76]. Results using this theory have been compared to cold-wire measurements in the Mach-6 facility, and show that the measurements are always slightly higher [30]. The reason for this has not been resolved yet. Refs. [30, 31] also show the Mach number profiles in the test section. With the exception of the data at a total pressure of one atm., all the profiles show fairly good uniformity. Finally, the dew point of the air was measured for some of the runs, to check the possible effects of condensation. These measurements were only taken for some of the experiments on the Hyper-2000, and none were taken for the noise measurements with different nozzle wall temperature distributions. The dew points measured during the August-September timeframe ranged from –1.1 to -14.7 °C. During the February-March timeframe, the dew points were between –25 to -30 °C. The drier climate during the winter season seems to be reflected in these measurements.

2.4. Efforts Toward Achieving Quiet-Flow

A possible approach to obtain quiet flow is to change the nozzle-wall temperature distribution. During the design and analysis of the nozzle contour, the wall temperature was assumed to drop linearly from 180 °C at the throat to room temperature at the end of

the nozzle [67]. However, finite-element computations have shown that the temperature drops to ambient in the first meter of the nozzle, and measurements have shown similar results [71]. Thus the effect of changing the nozzle-wall temperature distribution was investigated by insulating portions of the nozzle and contraction. The experiments were carried out using the Case-5 throat geometry, which exhibited no quiet flow [30]. Ceramic fiber insulation that was 1.5 in. thick was used. Two layers were used, since one layer was not enough to provide sufficient insulation. The mean and fluctuating pitot pressure were measured on the centerline, at 84.63±1/6 in. downstream from the throat, with a 0.062 in. Kulite pitot-probe. The driver tube and contraction temperature were set to 140 °C. The initial total pressure for all runs was one atm.

A baseline case was run first, with no insulation, denoted as Run 1. The tunnel was heated for 24 hours prior to performing the first run. From this point on, insulation was added progressively on the following regions in order: Run 2: throat (nozzle sections 1 and 2), Run 3: downstream portion of contraction, Run 4: nozzle sections 3 and 4, Run 5: nozzle section 5, Runs 6 and 7: the upstream portion of the contraction. For Run 7, the driver pipe temperature was increased to 160 °C., with the same insulation configuration as Run 6. The measured nozzle temperature distributions for all cases are shown in Figure 2.6, and Figure 2.7 shows the same data normalized by the respective driver pipe temperature. In both figures, the origin of the z-axis is at the throat, and the first two data points correspond to the 2^{nd} and 3^{rd} thermocouples shown in Figure 2.8, which is taken from Ref. [32].

The overall temperature increases as each section of insulation is added, as would be expected. The last case labeled “Skoch” was measured previously without insulation, with the tunnel heated to 160 °C. This plot clearly shows that using the insulation raises the temperature significantly, although less than initially expected. Even though the temperature has increased overall, the plots show that the temperature still drops near ambient about 45 in. from the nozzle throat. This is only about 10 in. downstream of the reference case without any insulation.

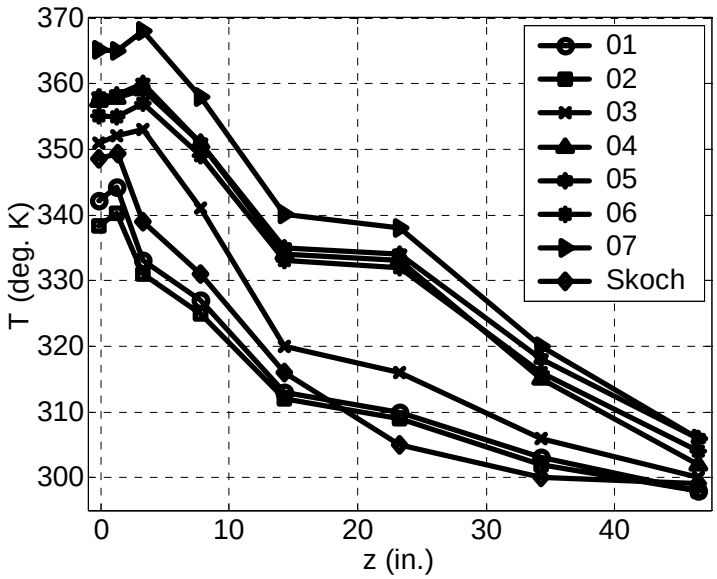

Figure 2.6. Temperature distribution along the nozzle.

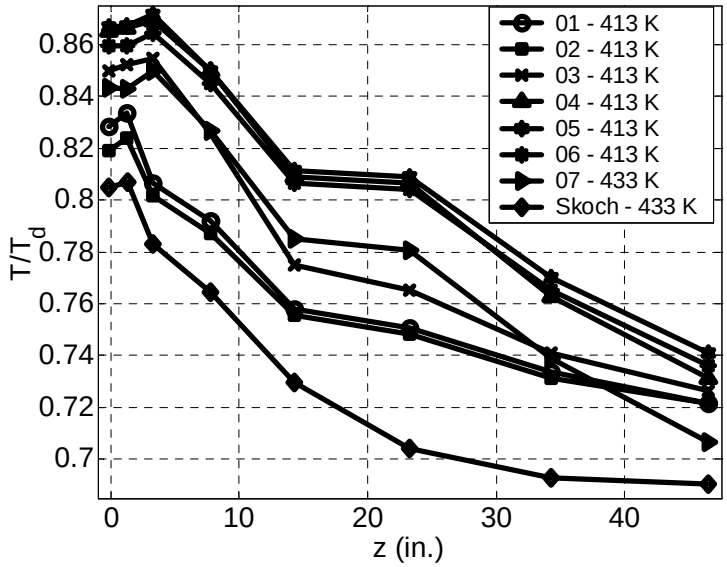

Figure 2.7. Normalized temperature distribution along the nozzle.

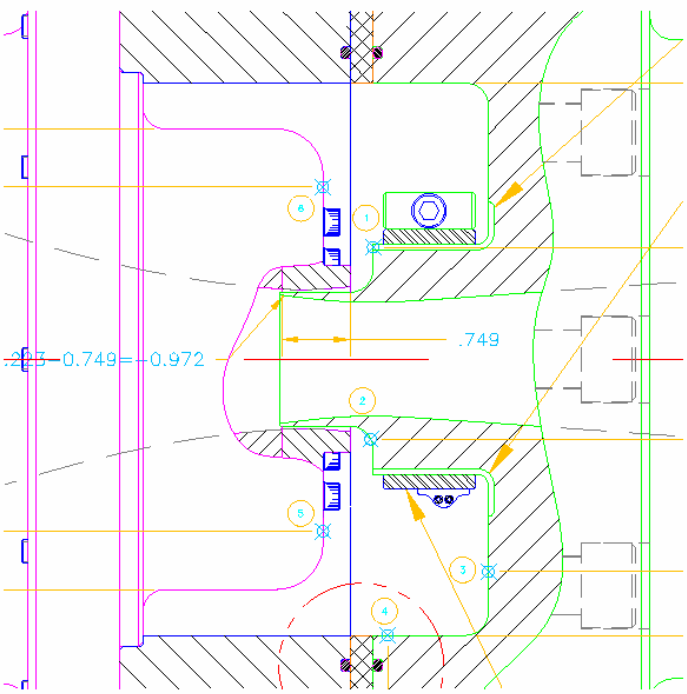

Figure 2.8. Diagram of the nozzle throat region, taken from Ref. [32].

This shows that the insulation is not sufficient to make a large change in the temperature distribution of the nozzle, and heaters will be required if a more gradual temperature drop along the nozzle is to be obtained. The measured noise levels for each case are listed in Table 2.1. The noise level seems to decrease with the addition of more insulation, except for Run 4. This is probably because the change in wall temperature changes the boundary layer properties. In previous noise measurements, a warmer nozzle-wall temperature or a colder driver-tube-gas temperature resulted in lower noise levels, which seems consistent with the results shown here [32].

Table 2.1. The conditions and resulting noise levels for different nozzle wall temperature distributions.

Run Number	Wait Time (hours)	Initial Total Temperature (deg. C)	Initial Total Pressure (psia)	Pitot Noise Level (% of mean)
1	24	140	14.48	5.77
2	14	140	14.46	5.67
3	25.5	140	14.55	5.53
4	21	140	14.45	5.69
5	18.5	140	14.53	5.52
6	21.5	140	14.49	5.47
7	12	160	14.41	5.22

2.5. The Hyper-2000 Model

The Hyper-2000 geometry was obtained from the Hyper-X program office, after consulting several organizations for a geometry that represents airbreathing hypersonic vehicles of current interest. The model consists of three compression surfaces and the chines. It is truncated at the combustor cowl. The compression surfaces have angles of 2.5, 8, and 11 deg. to the freestream, with the model at zero angle of attack, which is identical to the Hyper-X geometry. A simplified schematic of the compression ramp portion is shown in Figure 2.9, which is adapted from Figure 1 in Ref. [31]. The windward surface of the Hyper-2000 model is shown in Figure 2.10. The model was milled from standard 6061-T6 aluminum to reduce machining costs. The model is 11.79 in. long, and has a span of 5.619 in. at the trailing edge. The compression surfaces are flat over a span of 2.85 in.

The leading edge has a square cross-section, and not a nose radius. This leading edge geometry is the result of the tool-bit path used during the manufacture, where the windward and leeward surfaces of the model were machined first, and then the perimeter of the model was milled out from the aluminum block. The thickness of the leading edge at several spanwise stations was measured by pressing the model into a lead sheet. The

resulting profiles left in the lead sheet were examined under a 40X optical comparator. A sample image under the comparator is shown in Figure 2.11.

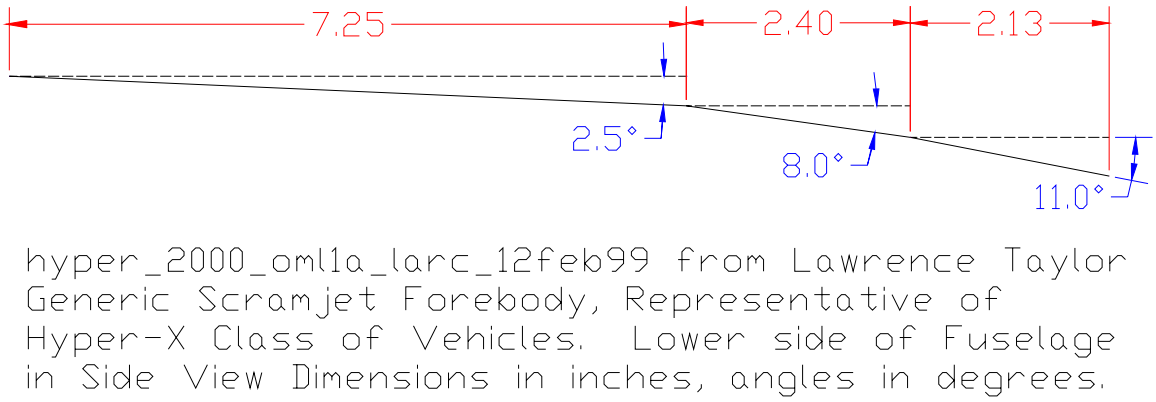

Figure 2.9. Sideview of the centerline of the Hyper-2000 forebody, adapted from Ref. [31].

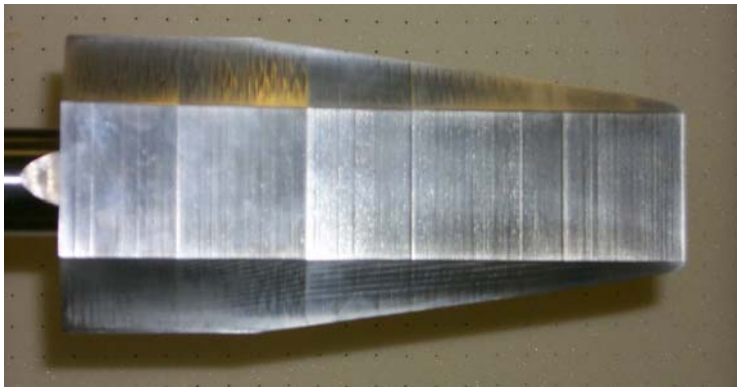

Figure 2.10. Picture of the Hyper-2000 forebody model.

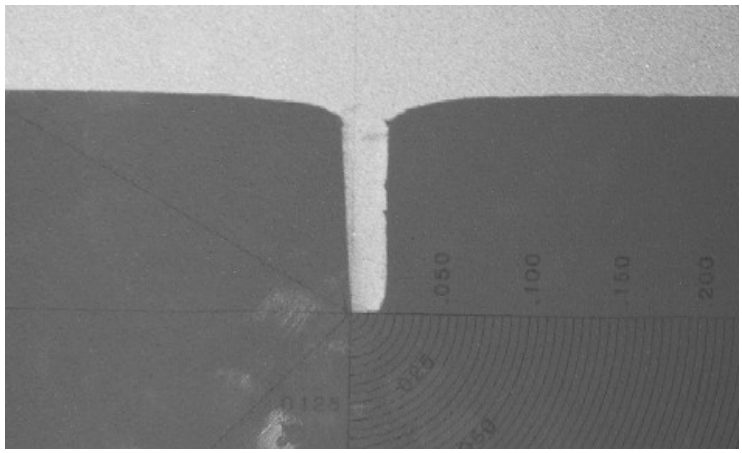

Figure 2.11. Image of the leading edge profile under an optical comparator with 40X magnification.

Measurements of the leading edge thickness were then taken along the span at several locations, and are shown in Figure 2.12. The thickness varies from about 0.008 to about 0.0122 in. The measurements are believed to be accurate to about 0.0005 in. These measurements results in a mean leading edge thickness of 0.0108 in. with an rms value of 0.001 in. There is a definite spanwise taper in the leading edge thickness. The left side of the model as seen from the front is slightly thinner. Unfortunately, these flaws were identified too late to allow the leading edge to be reworked to a smoother finish for the present effort.

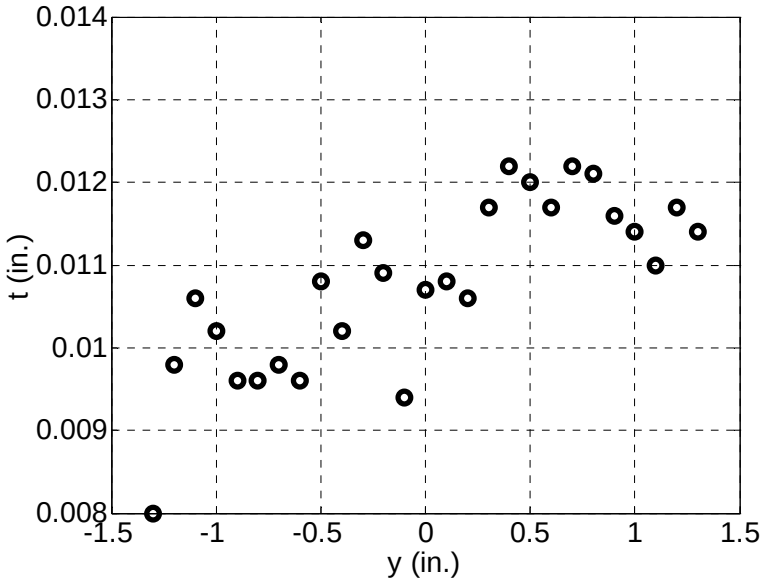

Figure 2.12. Leading edge thickness variation along the span. Negative coordinate corresponds to the left as seen from the front.

The compression angles on the Hyper-2000 are identical to those of the Hyper-X model. However, the relative lengths of the first and second compression ramps are slightly different. This discrepancy was also verified in the original CAD file received from LaRC, ruling out the possibility of a faulty manufacture of the model. The lengths of the two compression ramps for the Hyper-2000 model are shown in Figure 2.9. The first ramp extends 7.25 in. from the leading edge, followed by the second ramp, which is 2.40 in. For the Hyper-X model, the first ramp extends 12.433 in. from the virtual nose, and the second ramp is 5.334 in. [77]. When the lengths of these two models are non-dimensionalized by the total length from the nose to the end of the second ramp, the

lengths of the first compression ramps are 0.75 and 0.70 for the Hyper-2000 and the Hyper-X respectively. This shows that the first compression ramp is relatively longer on the Hyper-2000 model. The reason for this mismatch is not known, but it may be one of the changes made to the Hyper-X geometry so that it would be publicly releasable.

2.6. Temperature Sensitive Paint Calibration Rig

The temperature sensitive paint was calibrated prior to using it in the Mach-6 facility. In addition to temperature calibrations, which were in fact performed at various pressures, the pressure sensitivity of the paint at various temperatures was also examined as part of the instrumentation development. Repeatability of the calibration and degradation of the paint over time was also examined and characterized. These experiments used the same CCD camera and blue LED light source as in the Mach-6 experiments. For these tasks, a sample specimen was painted on a piece of stainless steel shim stock typically about 1”x 1” square, and tested in an environment-controlled calibration chamber.

A picture of the calibration rig is shown in Figure 2.13. The chamber is shown on the left with a specimen attached.

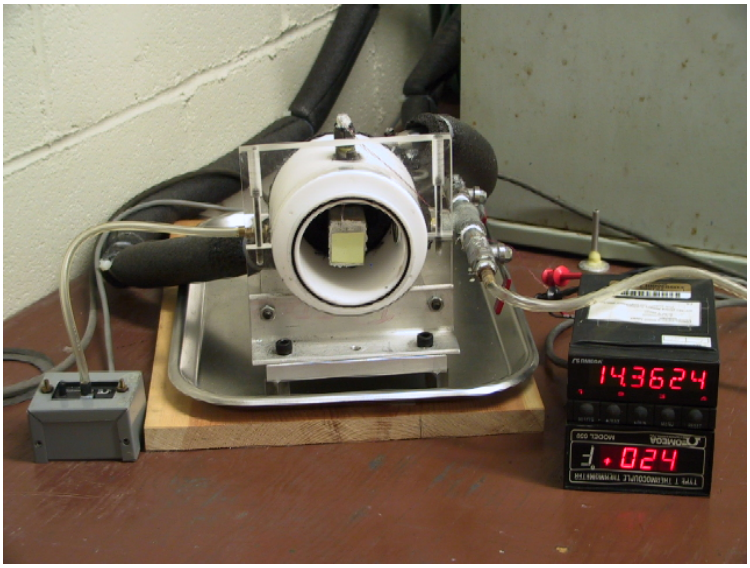

Figure 2.13. Picture of the temperature-sensitive paint calibration rig.

The test specimen is attached to the end of an aluminum bar with thermal grease. A glass cover piece is mounted over the front opening during tests. The temperature of the specimen is controlled using a digital temperature controller (Polyscience Model 9710), which continuously circulates a mixture of ethylene glycol and distilled water as the cooling or heating liquid. This particular mixture allows sub-zero temperatures without freezing. The liquid flows in and out of the back end of the calibration rig, which is directly attached to the test specimen holder. This component of the rig is constructed from aluminum to allow a high thermal conductivity. The temperature of the test specimen is read using a T-type thermocouple, which is placed between the specimen and the specimen holder. The current design only allows a sub-atmospheric pressure, which is controlled using a standard vacuum pump attached to one of the two valves. The pressure is read using a standard absolute pressure transducer (Omega PX142).

3. TEMPERATURE-SENSITIVE-PAINT MEASUREMENT TECHNIQUE

3.1 General Overview of Technique

Temperature-sensitive-paint (TSP) is used to measure the global temperature distribution of the model surface during the tunnel run. TSP works under the thermal quenching principle, where the luminescent molecules absorb a particular wavelength of light that depends on the luminescent chemical used, and emits red-shifted light at an intensity that depends on the surface temperature. As the temperature increases, the thermal energy of the excited fluorescent molecule also increases, and the emission intensity decreases. A CCD camera is most commonly used to capture the emitted light from the TSP. The temperature of the model surface can then be determined by applying a calibration that relates the model temperature to the emitted light intensity, using what is known as the intensity-based method. The decay rate or phase-shift of the emission from a pulsed excitation source can also be measured, using the lifetime method. This alternative has offered some advantages with pressure-sensitive-paints and thermographic phosphors, and should be possible to perform with TSP's as well, if necessary or desired [78-81].

A general schematic of a TSP layer over a model surface is shown in Figure 3.1, which is adapted from Ref. [82]. The actual temperature-sensing layer is composed of luminescent molecules imbedded in a binder material, usually some sort of polymer-based coating. For metallic wind tunnel models with high thermal diffusivity and conductivity, an insulation layer is painted on the model surface first. This decreases the heat transfer between the TSP layer and the model, resulting in a larger temperature change in the thin temperature-sensing layer. This in turn results in a higher signal-to-noise ratio, and allows the use of simplified heat-transfer models for data reduction.

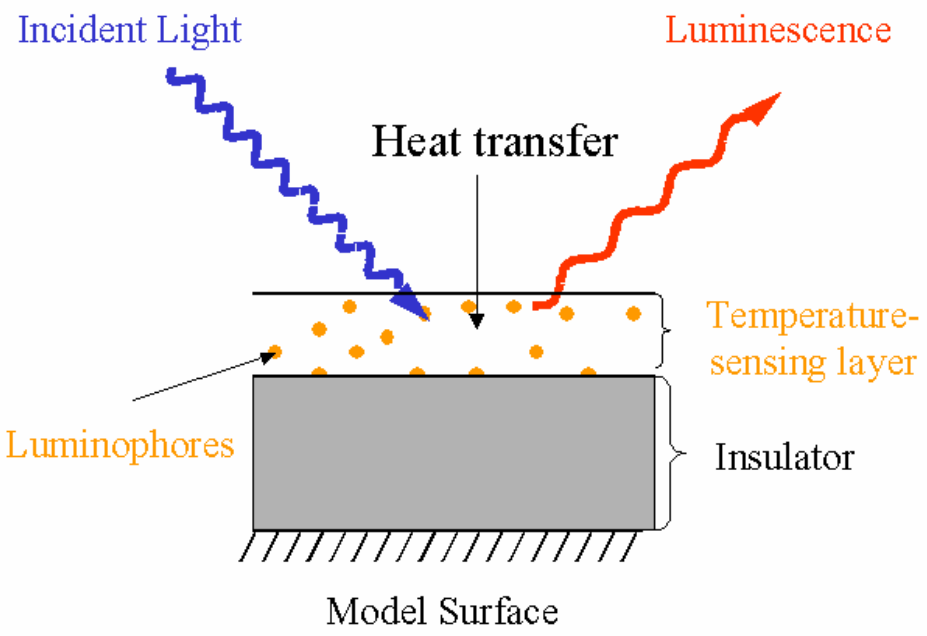

Figure 3.1. General schematic of a TSP layer over a model surface, from Ref. [82].

The fluorescent material and binder are dissolved in solvents so that they can easily be applied to the model surface with a brush or spray gun. The polymer binder is an important ingredient of luminescent paint systems, since it serves to adhere the paint to the model surface, but also influences the pressure and temperature sensitivity, and the response time as well. With the intensity-based method, which is used for this research, a reference image is taken at a known temperature (wind-off image). A second image is then taken during the tunnel run (wind-on image). The ratio of these two images eliminates non-uniform lighting and painting. The model surface temperature can then be determined through a calibration curve, either performed prior to the wind tunnel testing on a TSP sample, or in-situ during the wind tunnel test. A general procedural schematic of this process is illustrated in Figure 3.2, which is taken from Ref. [83]. In-situ calibration results in more accurate measurements, but requires thermocouples strategically placed in the model [84].

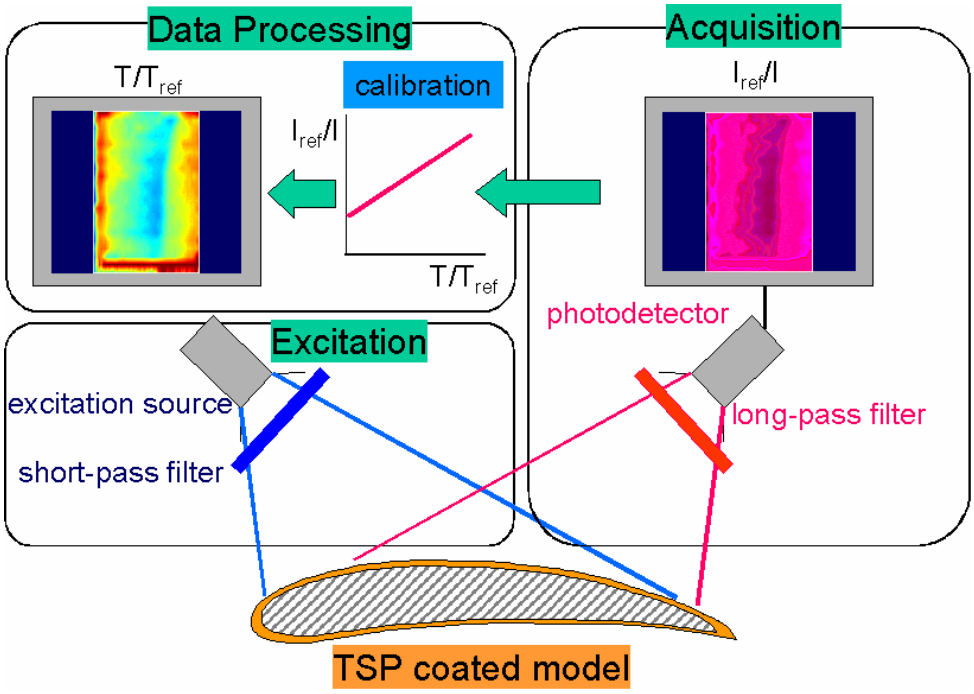

Figure 3.2. Schematic of the TSP experimental procedure, adapted from Ref. [83].

3.2 Selected TSP

Several luminophores, binder materials, and insulators have been discovered and developed over the years. A partial list and sample calibration data of some luminophores are listed in Refs. [55, 56]. In a past experiment in the Mach-4 facility, Ru(bpy), which is short for Tris(2,2'-bipyridyl) dichloro-Ruthenium(II) hexahydrate, has been used successfully [35]. For this research, Ru(phen), which is short for Dichlorotris(1,10-phenantrholine) ruthenium(II) hydrate, is used instead. This luminophore has been shown to be well suited for use in short-duration facilities [60, 84]. A comparison of the Ru(phen) calibration against Ru(bpy) showed the former to have a slightly higher sensitivity above room temperature (Figure 3.3). Both of these calibrations, and all calibrations shown in subsequent sections, were performed in the calibration rig. The reference condition is taken at 297 deg. K here. Both of these calibrations were done at one atm., with the same excitation light source and CCD camera used for the actual wind tunnel testing. The chosen binder for this research is DuPont's Chroma Clear polyurethane automobile paint. Again, this has been used

successfully in the past [60, 84]. Many of the Ruthenium-based luminophores are known to also be sensitive to pressure through oxygen quenching, an undesired characteristic for TSP's. Polyurethane binders offer the advantage of low oxygen permeability, which significantly reduces pressure sensitivity, reducing the error and uncertainty in the temperature measurement.

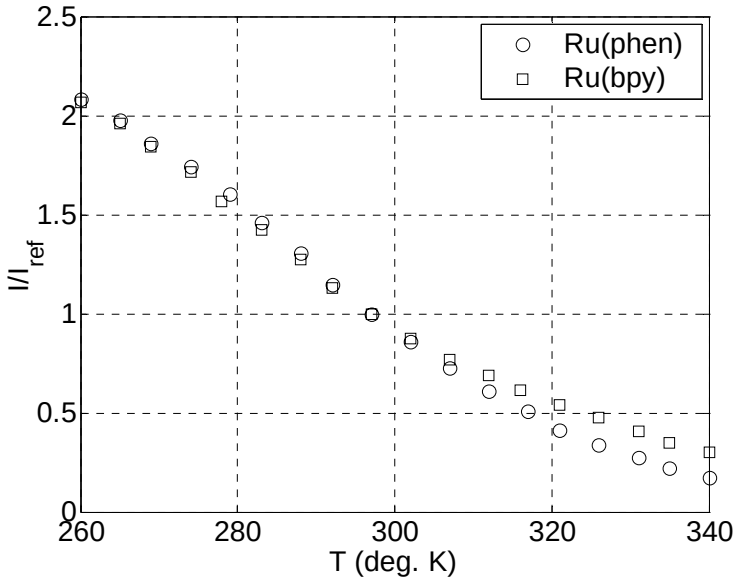

Figure 3.3. Comparison of the calibration data for Ru(bpy) and Ru(phen).

The insulation layer affects the sensitivity and accuracy of the heat transfer model used in reducing the data to heat transfer rates. For this reason the accuracy attainable in computing the heat transfer rates is dictated mostly by the accuracy to which the thickness and thermal properties of the insulator are known. Thus, Mylar films such as those used for remote-controlled airplane applications are well suited [85]. However these are not suitable for three-dimensional models, and an insulating layer must be painted onto the model. For the present research the same binder coating is used for the insulation layer as well. The thermal conductivity and diffusivity of this coating are 0.48 W/(m-K) and 2.7×10^{-7} m^2/s respectively, between the temperature ranges of 293-323 deg. K [84]. Often times, a white pigment is added to the insulation layer to enhance the reflectivity of the temperature-sensing layer above the insulator. DuPont's Ti-Pure R-900 titanium dioxide (TiO_2) powder is used for this research. Two thermal properties are known for this particular material: a thermal conductivity of 8.8 W/m-K and a specific

heat of 799 J/kg-K [86]. The addition of TiO_2 results in a softer insulator layer, which allows for easier polishing; however, it increases the thermal conductivity. The insulation layer is only a few percent TiO_2 by weight, so this should not cause significant problems.

3.3. Application Procedure

Application of the two paint layers involves craftsmanship, technique, and skill. It is impossible to outline a detailed procedure to achieve a good paint layer, but some key issues will be outlined. Both the insulator and temperature-sensing layers must be air-sprayed; using a brush is not sufficient. Using an air pressure of about 22 psig seems to work very well. The model and the spray gun must be cleaned thoroughly with acetone before spraying the insulating layer. The spray gun then must be allowed to dry for a few minutes, since any acetone residue will eat away the paint. For the Hyper-2000 model used for this research, 300-400 mL of Chroma Clear and 12-18 g. of TiO_2 powder are mixed. This usually results in an insulator thickness of about 3-5 mils. Chroma Clear is a two-part coating, and the amount quoted above includes both parts.

In the very beginning, a very thin layer should be sprayed on, by setting the flow rate on the spray gun to a minimum, and also by holding it relatively far from the model. Also, the spray gun should always remain in motion to avoid the paint layer from becoming too thick in one particular spot, and causing runs. This layer should then be allowed to dry for 10-15 min. This process should be repeated a few times, until a good initial coating is achieved. The flow rate should then be increased gradually, and repeated a few more times. The process can be stopped when the grayish color caused by the aluminum surface can no longer be seen, and the coating is bright white and highly reflective. The wet paint layer should be allowed to dry for at least 12 hrs. The dry insulator layer is then polished to remove any roughness. A 1200-grit wet sand paper is initially used until the orange-peel finish of the paint is completely removed. A 2000-grit wet sand paper is then used to smooth the surface further. This process typically removes

about 0.5-1 mil of insulator. The process removes most of the shininess of the insulator, which is partially restored using Meguiar's 2 Mirror Glaze Fine-Cut Cleaner.

The temperature-sensing layer is sprayed in an identical manner as the insulating layer. However two issues are much more crucial than when spraying the insulator layer: (1) that a very small flow rate is set, and (2) that the spray gun is kept in constant motion to cover the entire model surface without resulting in too thick of a coating. For the Hyper-2000 geometry, only 35 mL of the temperature-sensing 2nd coating should be used, of which 25 mL is the binder. This should result in a coating thickness of no more than 1 mil at most. About 0.01-0.02 g of the Ru(phen) crystals are first dissolved in 10 mL of ethanol. The exact quantity of Ru(phen) is not critical to the quality and performance of the paint. The quantity of the luminophore affects the brightness of the luminescence, which can be adjusted by changing the photodetector's shutter time. The quantity does not affect the sensitivity. However, if too much is used, then not all of the crystals will dissolve, possibly clogging the spray gun or depositing the crystals onto the model surface, causing problems during the experiments. Because the temperature-sensing layer is very thin, this layer should not be polished, and any polishing will probably destroy the uniformity of the coating thickness. However in the event that a polishing technique can be found, then it will not change the calibration, as confirmed in Figure 3.4. Here, the dataset labeled "original" is the same data shown in Figure 3.3, but the reference is taken at 302 deg. K. The cases labeled "raw" and "polished" are two new TSP specimens, painted in an identical manner as the specimen for the "original" case, but the insulator layer was polished before applying the TSP layer. The TSP layer for the "raw" specimen was not polished, and the TSP layer for the "polished" case was polished. All three calibration data are essentially the same.

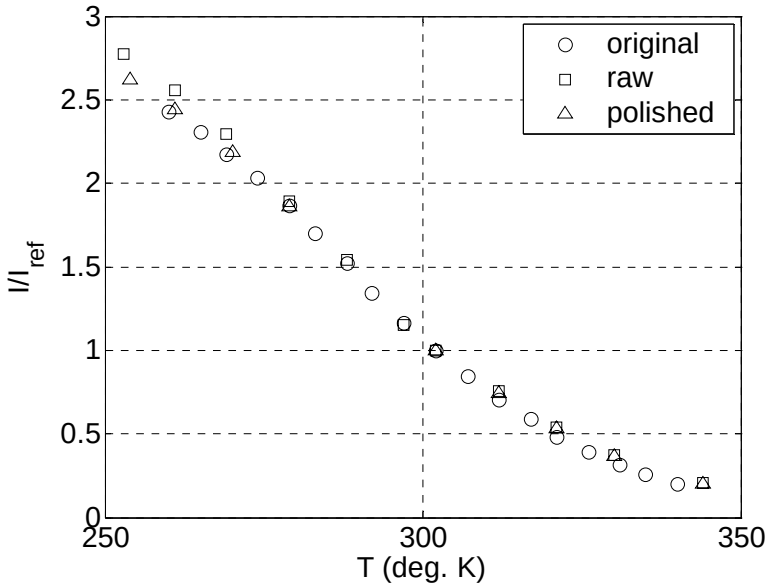

Figure 3.4. Comparison of calibration data for unpolished and polished temperature-sensing layers with Ru(phen).

3.4. TSP Characteristics

The luminophore chosen for this research is known to have both temperature and pressure sensitivity. A temperature calibration was shown in Figures 3.3 and 3.4, which was performed at one atmosphere. However, during wind tunnel experiments, the compression ramps on the Hyper-2000 model see pressures between 0.01-0.3 psia depending on the total pressure, as computed using oblique shock relations. The polyurethane binder is not perfectly oxygen impermeable, so some pressure sensitivity remains. This pressure sensitivity introduces error in applying the calibration data to different areas of the model with different pressures acting on them. Pressure and temperature calibrations for 18 different combinations of luminophores and binder materials are shown in Ref. [87]. One of the formulations tested was Ru(bpy) in an unspecified polyurethane binder, which is very similar to the TSP used for this research. The data shows that the luminescence intensity increases by 2 % between one atmosphere and a tenth of an atmosphere, with the temperature set constant at 293.1 deg. K. This is very small compared to the temperature sensitivity of –2 % per degree, with the pressure

set constant at nearly one atmosphere, so the error in applying the calibration data due to pressure sensitivity should be acceptable.

Because the TSP used for this research is very similar, it is reasonable to assume that the pressure sensitivity will be small as well. The assumption however was checked through a series of pressure calibrations, and the results are shown in Figure 3.5.

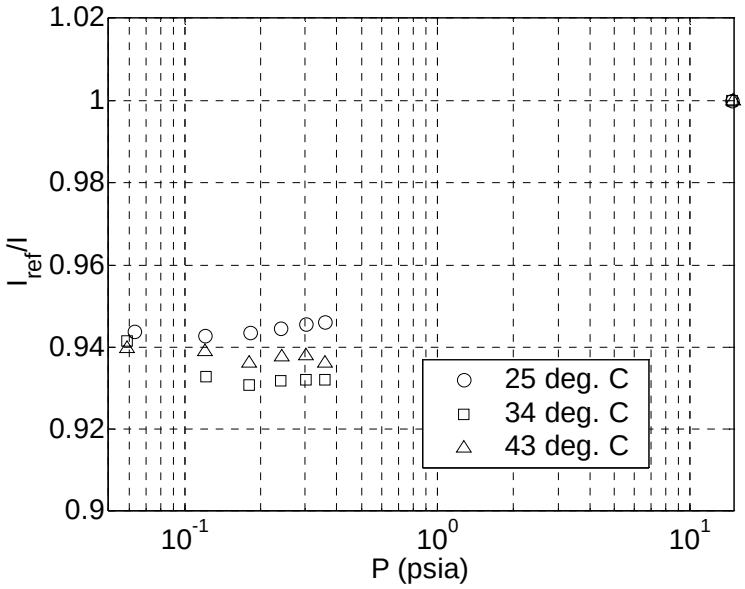

Figure 3.5. Sensitivity of the TSP to pressure variation at three temperature values.

The calibration was performed with the temperature held constant at three values, of 25, 34, and 43 deg. C. The reference is taken at one atmosphere for each case. The variation with pressure is about 5-7 % between one atmosphere and vacuum, which is slightly higher than that of Ru(bpy). The sensitivity at vacuum conditions, however, is very small, on the order of less than a percent at most. The small variations are probably caused by slight differences in the temperature during the calibration, on the order of tenths of a degree, since the thermocouple is accurate only to within a degree. This shows that the pressure variation on the model surface in this pressure range will result in an uncertainty of only about a percent, which is very acceptable.

The calibration was redone at vacuum conditions to compare against the calibration peformed at one atm. Figure 3.6 shows the resulting calibration data at vacuum conditions, compared to the calibration done at one atmosphere. The results are

more or less identical below 320 deg. K. The sensitivity is slightly lower at higher temperatures, but it is difficult to tell whether this is a repeatability issue, uncertainty in the measured temperature, or is actually a loss in temperature sensitivity. Whatever the case may be, this is the calibration data used for the TSP in this research.

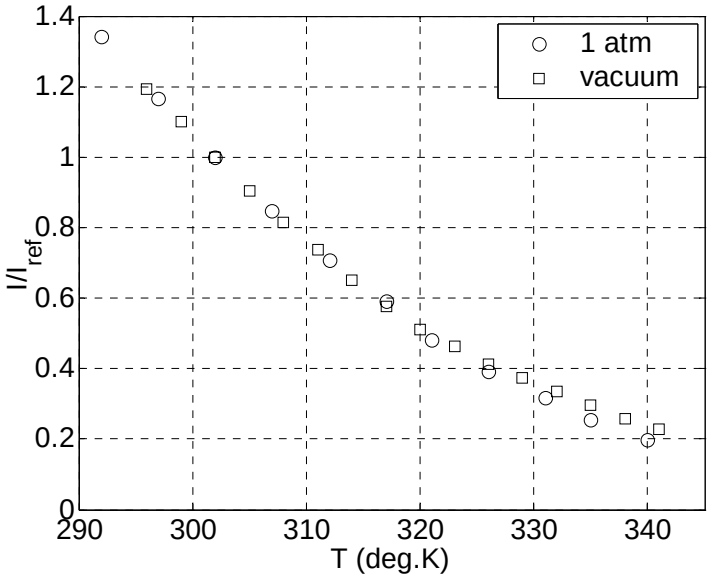

Figure 3.6. Comparison of temperature calibrations performed at atmospheric and vacuum conditions.

Another important aspect of luminescent-paint techniques is photodegradation, which is the loss of luminescence intensity and sensitivity resulting from exposure to a light source. This is however not really a problem for this research, because Ruthenium complexes are known to be quite stable, the model is exposed to ambient light for only a few hours during preparation of the experiments, and the light source during data acquisition is turned on for a very short time. Repeatability of the calibration over time can however become an issue, which is investigated briefly here.

The calibration was repeated several times over a period of about 100 hours. Four temperature values along the calibration curve were chosen. The results are shown in Figure 3.7. Here, the luminescence intensity is normalized by the first measurements, which were taken approximately 19 hours after preparing the TSP samples. At the lowest temperature of 23 deg. C the luminescence intensity decreases, which is a sign that the paint is degrading. However after 120 hours the intensity has dropped only by 4 %,

which is not that significant. The intensity at the remaining three temperature values of 41, 53, and 62 deg. C increases, the opposite trend of the data at 23 deg. C. For the 53 and 62 deg. C cases, the intensity increases by almost 12 %, which is quite significant, whereas for 41 deg. C the intensity increase is only about 4 %. The irregularities seen in all of the data are probably from the uncertainty in the temperature measurement.

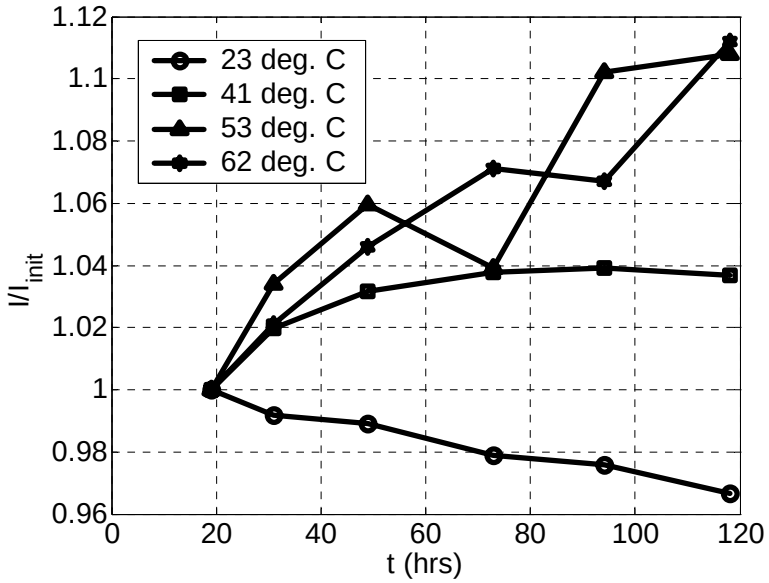

Figure 3.7. Variation of the luminescence intensity at three temperatures.

The data shown in Figure 3.7 can be used to compute the temperature sensitivity for three temperature ranges, if the calibration curve (e.g., Figure 3.6) is represented by three linear-fits. This was done for the data shown in Figure 3.7, as shown in Figure 3.8. Again, the temperature sensitivities are normalized by the initial set of measurements. The sensitivity in the lowest temperature range is expected to decrease, because the intensity at 23 deg. C is monotonically decreasing whereas the intensity at 41 deg. C increases. The intensity increase at 53 deg. C is more than the intensity increase at 41 deg. C, which also results in a sensitivity loss. However the sensitivity tends to increase at the higher temperatures. As shown in Figure 3.7, the reason for the intensity increase above 23 deg. C is not known, but one possibility is that the properties of the binder material are changing. This might be avoided in future tests by pre-conditioning the TSP layer prior to running any calibration or wind tunnel tests. Pre-conditioning of the TSP

can be accomplished by simply heating the paint layer up to 40-50 deg. C for about an hour.

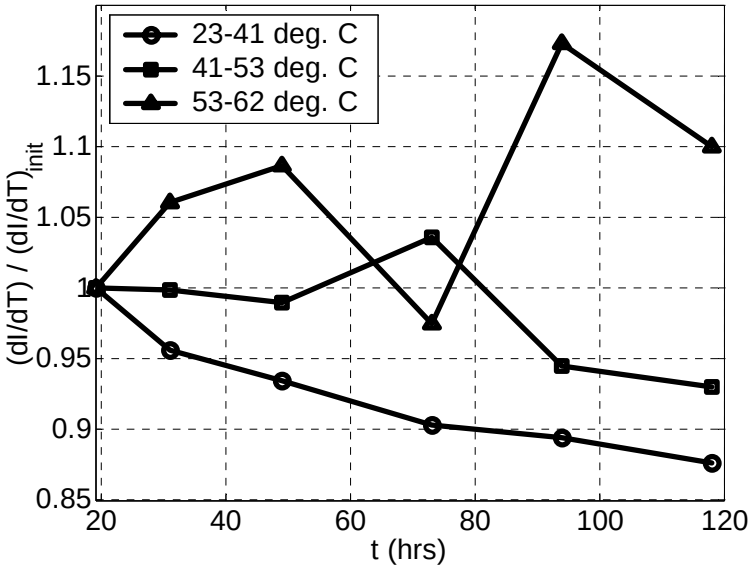

Figure 3.8. Variation of the temperature sensitivity at three temperatures.

4. EXPERIMENTAL SETUP AND DATA ACQUISITION TECHNIQUES

4.1. Setup and Procedure for Temperature Sensitive Paint Experiments

A general schematic of the experimental setup is shown in Figure 4.1, which was adapted from Ref. [36]. Note that none of the components are shown to scale. An image of the setup is shown in Figures 4.2 and 4.3. The black circular pod is the 4 in. blue LED source (ISSI LM4 464 nm) containing 341 individual LED's for illumination. Both the LED source and the 12-bit CCD camera (Photometrics Sensys 0401E) used to acquire the images point at the Hyper-2000 model seen through the window. A long-pass filter with a cut-off wavelength of 500 nm is used on the CCD camera lens, so the light from the blue LED source does not pass directly into the camera.

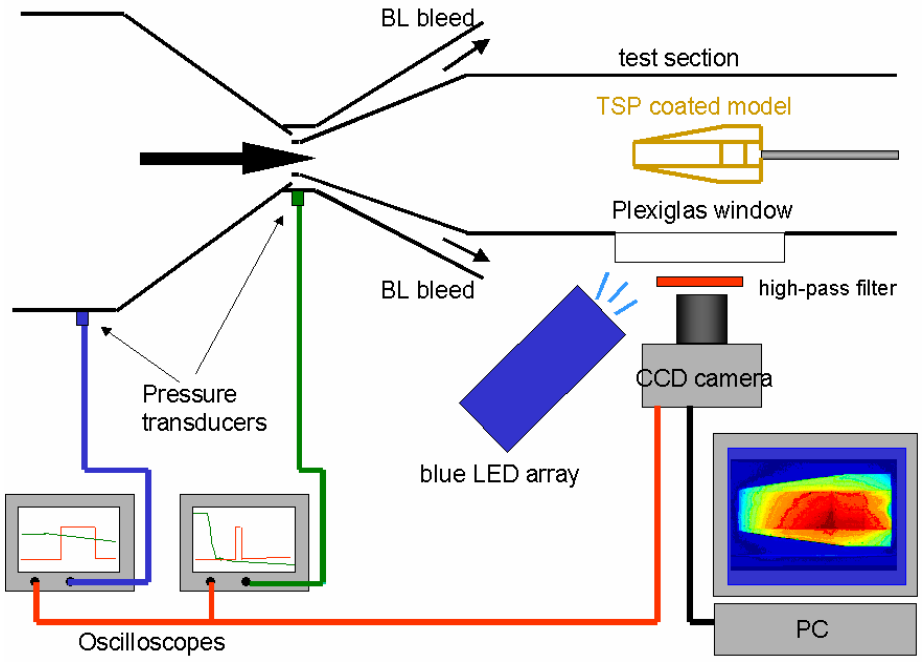

Figure 4.1. Schematic of the experiment setup, adapted from Ref. [36].

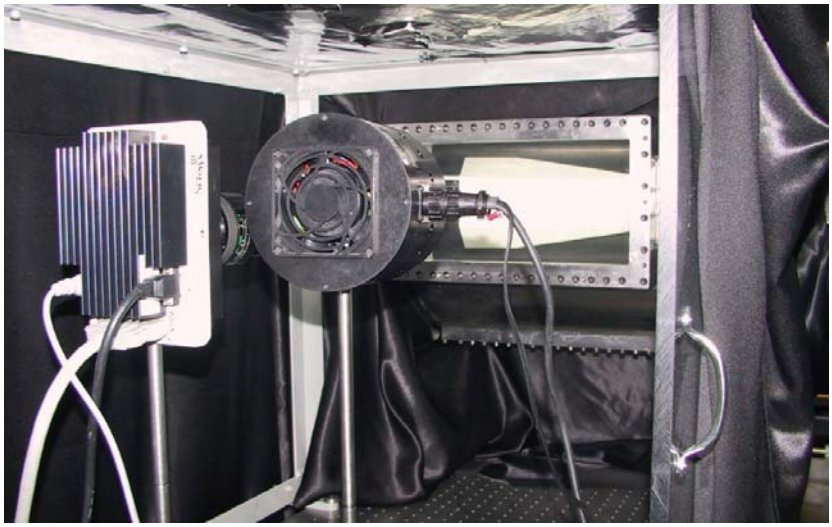

Figure 4.2. Image of the experimental setup.

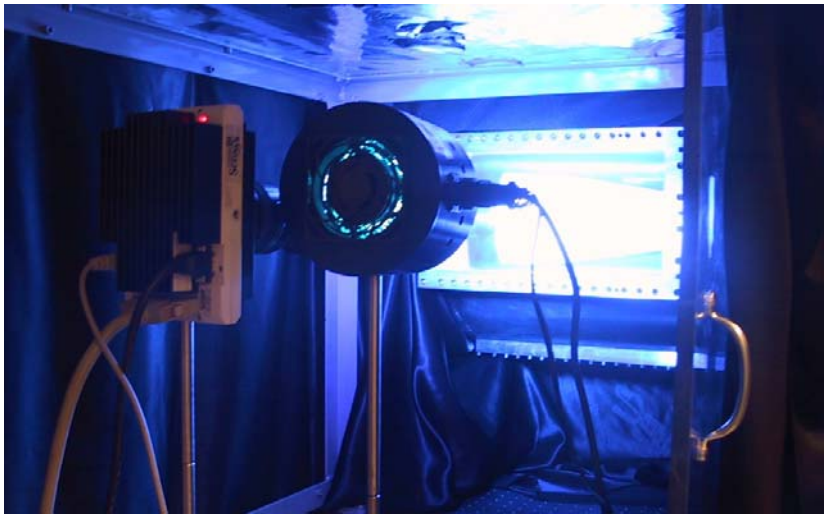

Figure 4.3. Image of the experimental setup, with the LED light source turned on.

The CCD camera at present must be activated manually, and cannot be triggered by an external signal. The image acquisition time with respect to tunnel startup can be repeated to within 0.1-0.5 sec. A 5-volt DC signal is generated from the camera while the shutter is open. The signal is fed into two oscilloscopes (LeCroy 9304/9314 AM). One of them records the signal from a Kulite pressure transducer mounted in the plenum section of the boundary layer bleed at the nozzle throat. The rapid decrease in pressure caused by the tunnel startup and the signal from the camera can be used to find the image acquisition time relative to tunnel startup. The second oscilloscope records the signal

from a Kulite pressure transducer mounted at the entrance to the contraction. This signal combined with the camera signal gives the total pressure during image exposure. The total temperature during image exposure can then be computed using Equation 2.1.

The entire setup is placed inside the Lexan® enclosure, and the enclosure is covered with black fabric to isolate the imaging system from the room lights. Turning off the room lights can simply eliminate most of the ambient light, however procedurally it was much more efficient to keep the room lights on constantly, and it also facilitated the operation of the facility. The exposure time of the CCD camera is typically set to between 50 and 200 ms, depending on the position of the LED source and thickness of the TSP layer. The exposure time is adjusted when acquiring the wind-off image so that the majority of the CCD bit-well will be filled up. In the preliminary experiments the wind-off image was taken immediately before the run, but for the final data set the wind-off image was taken at vacuum conditions, to eliminate the uncertainty due to pressure differences between the wind-off and wind-on images.

4.2. Effect of Using Multiple Images to Reduce Noise

In all of the experiments performed for this research, single wind-off, wind-on, and dark images are used. In many PSP and TSP experiments performed to date, several images for each are acquired, and then averaged [80, 88, and 89]. This can sometimes reduce shot and read-out noise levels and result in much cleaner data. This technique was briefly investigated for a particular wind tunnel run case, where five wind-off images were taken prior to running the tunnel. For this comparison case, only one dark and wind-on image was taken. The dark image is usually a very small fraction of the signal, and taking the average does not result in much of a benefit. Multiple wind-on images cannot be taken with the current CCD camera because of its slow framing rate, of about an image every 1-1.5 sec. The freestream flow is not steady state for this duration, and averaging wind-on images under these conditions would actually introduce significant error, due to changing flow conditions.

The uncalibrated temperature image obtained from using one or five wind-off images is compared in Figure 4.4. From visual inspection, the two images look identical, and no obvious differences can be seen.

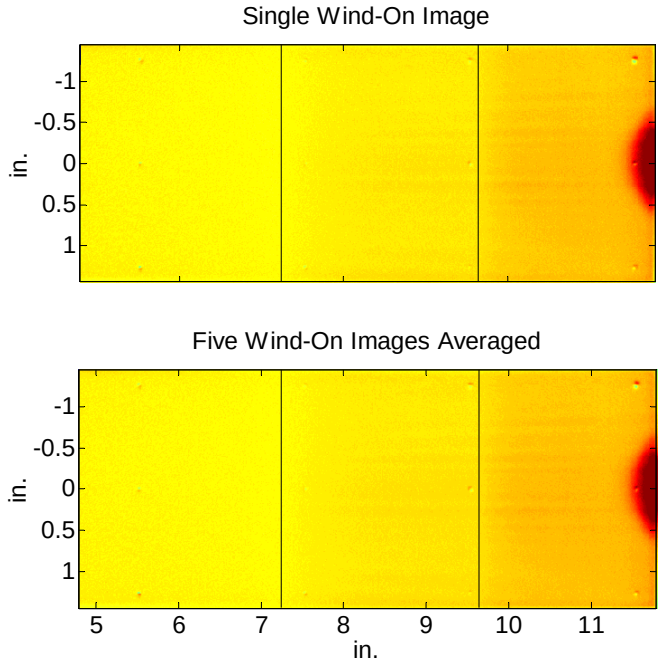

Figure 4.4. Uncalibrated temperature image obtained using a single wind-off image, and using the average of five wind-off images.

The spanwise distribution of the uncalibrated temperature is shown in Figure 4.5, which is extracted from these images. Only the data on half of the span is shown for clarity. This figure also does not seem to show any significant differences between the two cases compared. However the rms of the spanwise distribution does show slight differences. This is illustrated in Figure 4.6, where the rms of the fluctuating component of the spanwise distribution is plotted along the streamwise coordinate. The noise level is slightly lower when using the average of five images. However on the third compression ramp the rms values are actually lower when using only a single image. It is not clear why this would be the case, but the signal-to-noise ratio is probably higher on the third surface where the temperature is higher. The benefit of using multiple wind-off images does not seem to result in a significantly lower noise level, and all experiments performed for this research used only one wind-off image. This also shows that the noise level

might decrease if the model is cooled prior to running the tunnel. The larger temperature change from wind-off to wind-on conditions will result in a higher signal-to-noise ratio.

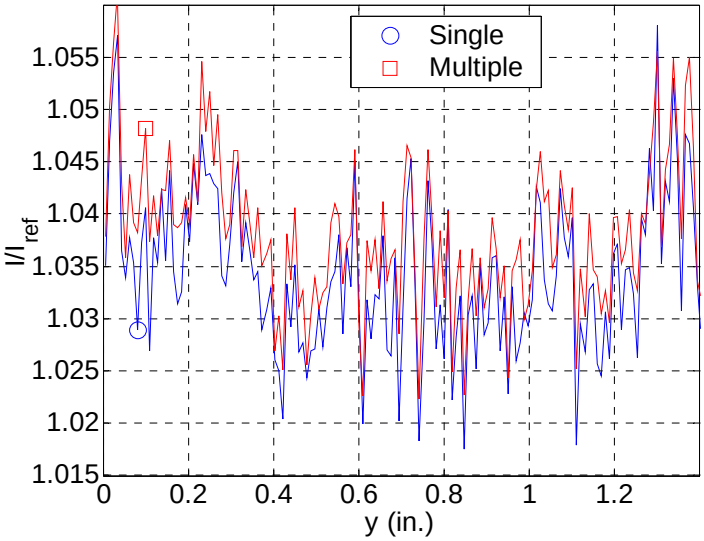

Figure 4.5. Spanwise distribution of the uncalibrated temperature using a single wind-off image, and using the average of five wind-off images.

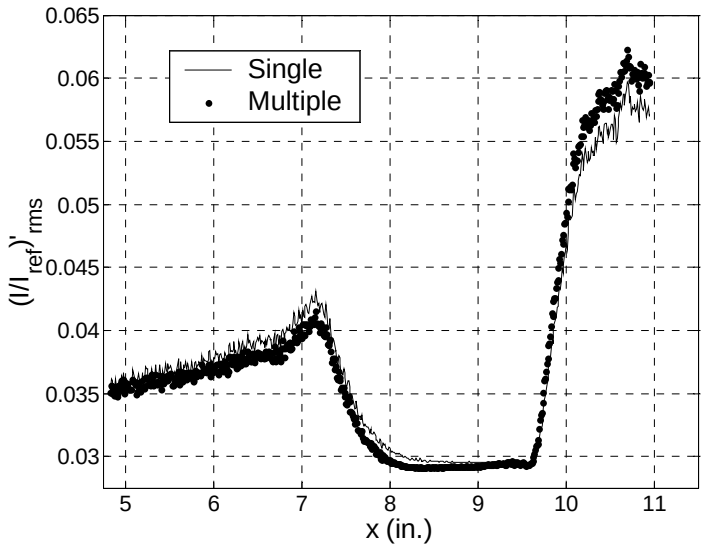

Figure 4.6. Streamwise distribution of the rms of the fluctuating component of the spanwise uncalibrated temperature, using a single wind-off image and the average of five wind-off images.

4.3. Effect of Image Acquisition Time

The quality of the stability measurements, of the streamwise vortices, is partially dictated by the smallest amplitude of the instability waves measurable. This is governed by the contrast between the higher heating regions and the rest of the model surface. A possible way to enhance the spatial variation of the temperature due to the streamwise vortices is to take the wind-on image later into the tunnel run. This would allow the differences in the temperature between the portions of the model that sees an increased heating and the portions that do not, to develop, resulting in a larger contrast between the two regions.

This concept was tested on a particular case that showed several striations patterns growing on the second compression ramp. Four wind-on images were taken approximately 1.2 sec. apart, with the first image taken 1.3 sec. after tunnel startup. The total pressure and temperature was initially at 128.5 psia and 160 ºC respectively, and the wind-off images were taken at unit Reynolds numbers of 2.59, 2.50, 2.41, and 2.33 million/ft. The uncalibrated temperature images using the first and last images taken are shown in Figure 4.7.

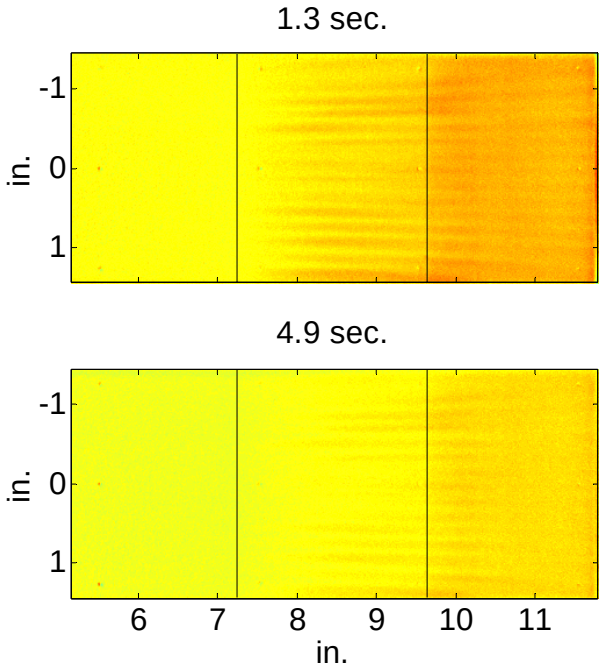

Figure 4.7. Uncalibrated temperature images using wind-off images taken at different times from tunnel startup.

Here, both images use identical false-color scales. The striation patterns are clearly more visible in the first image, and appear to become washed away later into the tunnel run.

A portion of the fluctuating component of the spanwise variation of the uncalibrated temperature is compared in Figure 4.8. Here 21 pixel columns, which span from a streamwise coordinate of 8.57-8.74 in., are averaged to reduce noise. The periodicity in the variation which results from the striations are clear, and they remain for the most part stationary throughout the tunnel run. Also shown is that the amplitudes of the fluctuation decreases with time. Intuitively, it might seem that the images taken later into the tunnel run should show a larger amplitude, because the surface temperature difference between the high and low heating regions would increase later into the tunnel run. However, two-dimensional conduction effects could become significant as well. Despite this unsolved issue, the fluctuations seem to be more easily measurable immediately upon tunnel startup, and for this research the wind-on image was taken as soon as possible after tunnel start up.

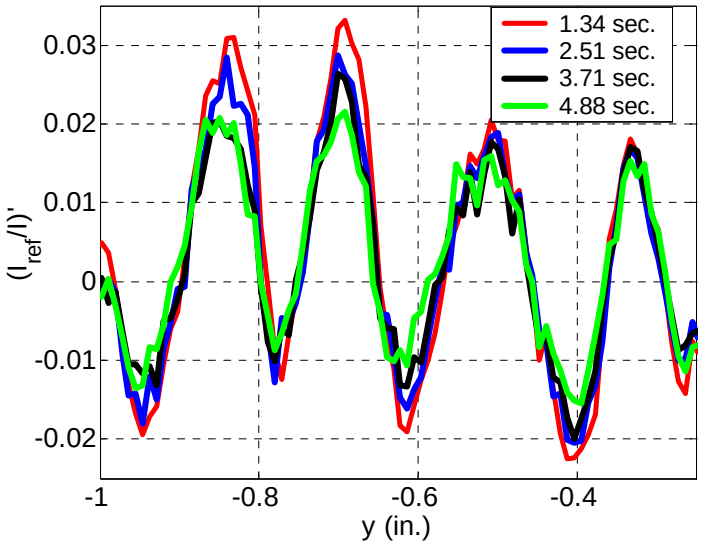

Figure 4.8. Fluctuating component of the spanwise variation in the uncalibrated temperatures.

4.4. Effect of CCD Camera Resolution

The smallest amplitude wave measurable is dependent on the resolution attainable with the imaging system. For digital imaging systems such as the CCD camera in use, the smallest temperature difference resolvable is determined by the temperature sensitivity of the TSP, heat transfer rate sensitivity of the binder material, and by the resolution of the CCD camera. The sensitivity of the TSP, the luminescence intensity change with temperature, is determined from the characteristics of the luminophore. The sensitivity of the binder to heat transfer rate, which is the temperature change of the TSP layer for a given heat transfer rate is dominated by the binder thermal properties, but also by the thickness of the TSP and insulator layer. The purpose of the TSP layer is to respond to the heat transfer, which can be maximized by using a thin TSP layer and a thick insulator. However too thin of a TSP layer will significantly decrease the luminescence intensity, resulting in lower signal-to-noise ratio. Too thick of a insulator layer also might change the aerodynamic geometry of the model, due to the increasing intrusiveness of the paint layer, which has been seen in PSP experiments [90]. Thus there is a trade-off in the two paint layer thicknesses, in terms of achieving a high signal-to-noise ratio with a thicker TSP layer but with a slower response time [91], and achieving a larger temperature difference by using a thicker insulator, but at the expense of paint layer intrusiveness. These issues were not investigated as part of this research, but the effect of a higher bit-depth on the CCD camera was briefly investigated.

The 12-bit CCD camera used for this research has a total intensity count of 4095 (2^{12}). Thus the smallest uncalibrated temperature difference resolvable with this camera is the ratio 4094/4095, which is 0.99976 neglecting the useful intensity count loss due to the dark image, non-uniformity, shot, and readout noise. Assuming that the model is initially at 25 ºC prior to tunnel startup, the smallest temperature change from the wind-off condition measurable is 0.008 ºC, which is computed using the TSP calibration shown in Figure 3.6. Typical wind-off images with the 12-bit camera however have intensity counts between 2400-4000 when factoring in the dark image, non-uniformity, shot and readout noise, which result in a loss in resolution. 14 and 16-bit CCD cameras also have a significantly higher maximum intensity count of 16383 and 65535 counts respectively,

allowing for a much higher resolution. This is illustrated in Figure 4.9, where the theoretical minimum measurable temperature changes are shown against the initial intensity counts for the three bit-depths of CCD cameras.

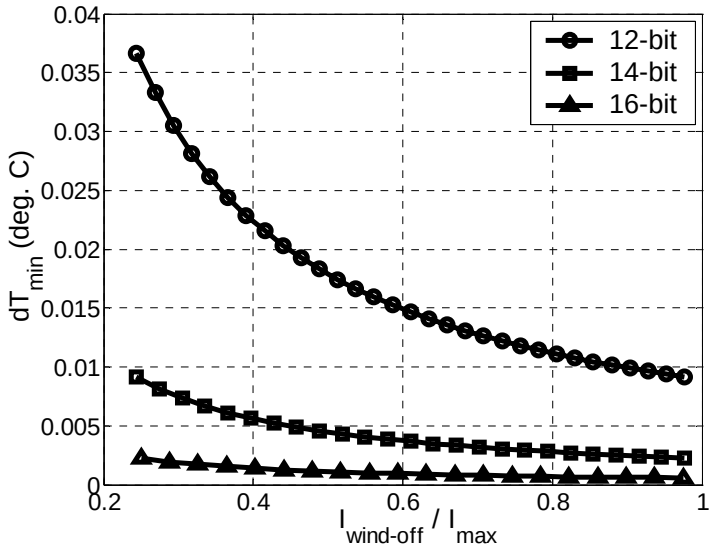

Figure 4.9. Minimum temperature difference measurable with a 12, 14, and 16-bit CCD camera depending on the initial intensity counts.

An initial temperature of 25 ºC was used for all cases shown. The initial intensity counts are normalized by their respective maximum intensity counts.

The plot confirms that the resolution improves as the capacity of the CCD bits is filled. The improvement of the resolution for higher bit CCD cameras compared to the 12-bit is also significant. The 16-bit camera can achieve a resolution that is an order of magnitude finer than the 12-bit camera. The ability of higher bit CCD cameras to measure a smaller temperature change implies that they can measure smaller amplitude streamwise vortices. This would be advantageous for several reasons. First, smaller amplitude disturbances are more likely to be governed by a linearized instability theory, which already exists and awaits validation. Second, calculation of the integrated growth rates of the waves requires some sort of initial disturbance amplitude. The smaller of an amplitude that the waves could be measured, the better of an initial disturbance amplitude can be obtained.

A test case was performed to investigate the possible advantage of using a higher resolution CCD camera. A particular test condition was repeated using the 14-bit camera. The surface temperature distributions taken with the two cameras are compared in Figure 4.10.

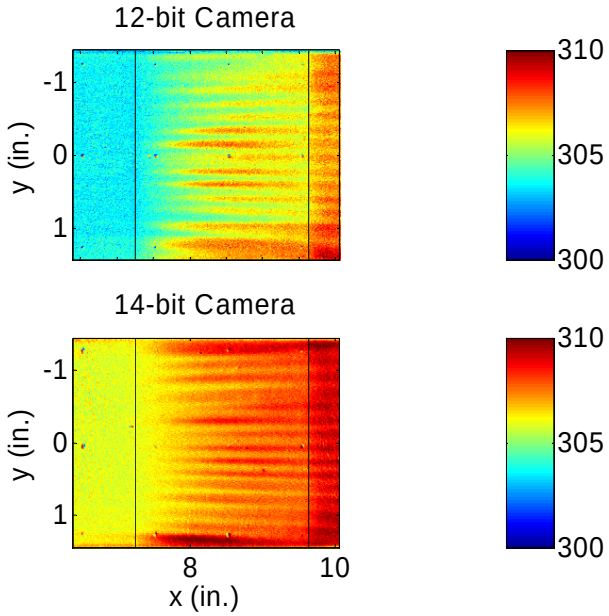

Figure 4.10. Comparison of the measured surface temperatures (deg. K) using a 12-bit and 14-bit CCD camera.

The flow conditions for the 12-bit camera case was a total pressure of 120.5 psia and a unit Reynolds number of 2.60 million/ft. The model was initially at 26 ºC, and the image was taken 0.72 sec. after tunnel startup. The exact flow conditions for the 14-bit camera case are not known, but should be within a few percent of the 12-bit camera case. The model temperature was initially at 27.7 ºC. Because the initial temperature is higher for the 14-bit case, the overall temperature is higher as well. No other significant differences are seen in the two images. The development of streamwise vortices first become visible around 7.5 in. for both cameras.

The fluctuating component of the spanwise temperature distribution is compared at two streamwise locations, of 7.09 and 8.85 in. from the leading edge, in Figure 4.11. The 14-bit camera does not seem to show any obvious advantages over the 12-bit camera at both stations. The data from the 14-bit camera may result in lower background noise, evident in the comparison at 7.09 inches. The amplitudes of the fluctuations measured by

the 14-bit camera at the second station might be slightly lower compared to the 12-bit camera. It is difficult to say whether this is due to lower noise, or is an effect from the different image acquisition time and the initial model temperature as discussed in the previous section.

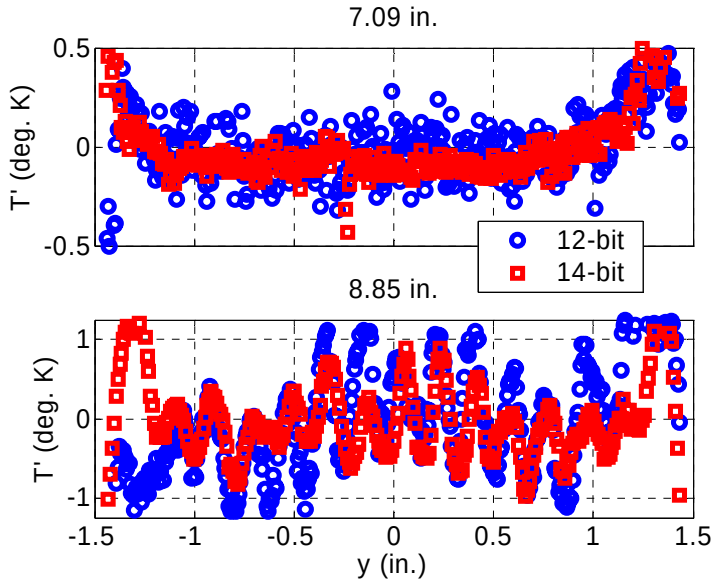

Figure 4.11. Comparison of the measured spanwise temperature distribution at two streamwise stations using the 12-bit and 14-bit CCD camera.

The rms of the spanwise temperature distributions is shown along the streamwise coordinate in Figure 4.12, for both the 12-bit and 14-bit camera. Here, 20 spanwise temperature distributions were averaged to reduce noise for both cases. Overall, the 12-bit camera gives a higher rms level. The image processing on the images taken with the two cameras achieved an image pixel alignment accuracy of about 0.04 and 0.006" for the 14-bit and 12-bit cameras respectively. Because the images from the 12-bit camera are better processed, the higher rms values cannot be the result of graininess of poorer quality images. Therefore, this might suggest that small fluctuations are actually better resolved with the 12-bit camera. However, the 14-bit camera seems to show a smoother distribution of the fluctuations along the streamwise coordinate.

The comparisons made between the 12-bit and 14-bit camera do not seem to show a significant and definitive advantage of the 14-bit camera. This implies that taking full advantage of a higher-resolution camera will not be a trivial task. Even if the 14-bit camera truly is capable of resolving smaller amplitude disturbances, simply replacing the

camera in the measurement system will not yield higher quality measurements. More work is necessary in this area to improve the quality of the measurement technique.

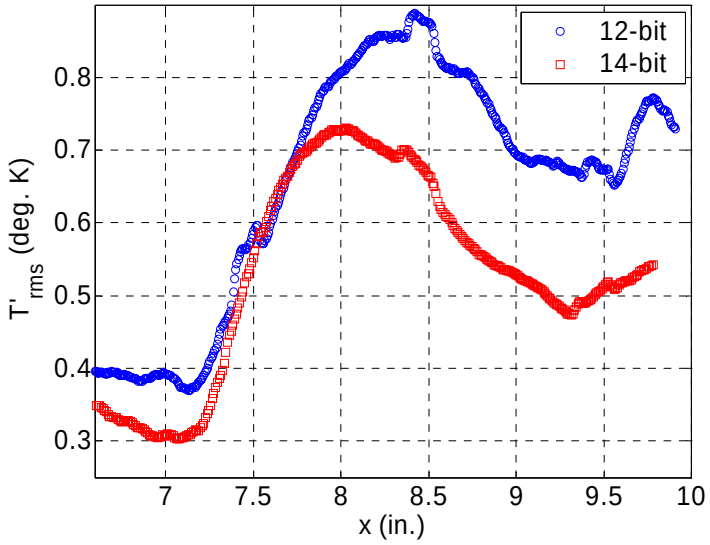

Figure 4.12. Streamwise distributions of the temperature fluctuation levels measured with the 12-bit and 14-bit camera.

4.5. Oil-Flow Visualization Experiments

Oil-flow experiments were performed to visualize the overall flowfield features which cannot be readily measured with TSP's. The separation line near the first compression corner is of primary interest for these experiments. Generally it is very difficult to measure separation onset using TSP's, because the change in heat-transfer-rate in the separation zone is not significant enough to cause a noticeable temperature difference compared to the regions where the boundary layer is attached. Oil-flow experiments also give an understanding of the surface streamlines, which is important for modeling cross-flow instability.

For these experiments, pink fluorescent pigment (Dayglo Color Corp) was added to the oil, and then illuminated with the same blue LED used for the TSP experiments. An orange or red filter was used on the imaging cameras to block the blue light reflections from the window. Traditionally the model surface is painted black when

performing oil-flow experiments and a white pigment is added to the oil to enhance the contrast in the images. Because fluorescent oil was used for this research, there was no need to have a black model surface. Consequently, the model was spray-painted with typical commercial high temperature white paint, which permitted the application and use of registration marks and image-processing methods used for the TSP images. Several thin layers were applied which were slightly polished with a 1200/2000-grit wet sandpaper before painting the next layer. As with preparing for the TSP experiments, this generally results in a smoother finish with the final coat.

Dow Corning's silicone oil was used for these experiments. Three viscosity grades were available, 100, 200, and 350 cs. A 20 and 50 cs viscosity oil were also available, but were not used because there seemed to be a possibility that these viscosity oils could craze the Plexiglas window, according to the oil manufacturer. A simple test was performed by applying few drops of 50 cs viscosity grade oil onto a Plexiglas specimen. After several days the Plexiglas did not seem to be affected, from visual inspection. However, a decision was made to not use 50 cs oil until more thorough investigations could be performed.

Out of the available oil viscosity grades, the 200 cs viscosity oil resulted in the best images when the fluorescent oil was brushed onto the model surface in a fairly uniform coating. This technique was mainly used to capture the separation line and the spacing of streamwise vortices, but could not capture the reattachment point or the surface streamlines very well. To capture the latter two flow features, the oil-dot technique was used. Here, a thin layer of clear oil was wiped onto the model, and then dots of fluorescent oil were flicked onto the base coat. For this technique, the 100 cs viscosity oil for both the base coat and the fluorescent oil resulted in the best images. A sample image for this technique is shown in Figure 4.13. The image shows a close-up view of the compression corner regions, with the model leading edge to the right. The approximate locations of the compression surfaces and corners are marked with white lines for clarity.

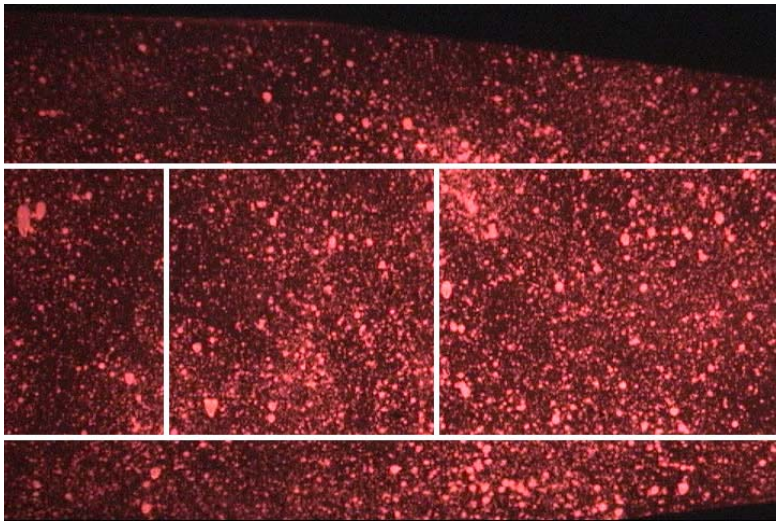

Figure 4.13. Image of the model with sprits of fluorescent oil applied.

The setup for these experiments was nearly identical to the setup for the TSP experiments. The blue LED pod, a high-resolution digital camera, and a digital video camera were placed inside the Lexan assembly and pointed at the model in the desired manner. An orange filter was consistently used with the digital camera. A red filter seemed to block too much of the fluorescence, and much of the contrast between the bright and dim regions of the model were lost. The quality of the video taken with the video camera was independent of whether an orange or red filter was used. Consequently, a newer and cleaner red filter was used. The tunnel was started almost immediately upon pressurization so that the oil would not run off the model, about 15 minutes after applying the oil onto the model. The video camera was started prior to starting the tunnel, and the digital camera took four images spaced about 0.5 sec. apart about 7 sec. into the tunnel run, immediately preceding tunnel unstart. The tunnel unstart washed away most of the flow features which developed over the 7-9 sec. of Mach 6 flow.

This development of the flow features over time is illustrated in Figures 4.14-4.17. Figure 4.14 is an image immediately following tunnel startup. The non-uniformities in the oil layer are still evident here, as seen by the brighter and darker regions. The oil has not yet moved enough to reveal the major flow features. Figure 4.15 is an image 6.5 sec. later. The separation line is clearly seen in this image, which is

represented by the bright line immediately upstream of the first compression corner. The presence of streamwise vortices on the second and third compression ramp is also seen in this image. Figure 4.16 is an image taken 0.75 sec. later, which is estimated to be about 0.25 sec. after tunnel unstart. The oil accumulated at the separation line has been washed away, and the separation line is no longer clearly visible. Finally, Figure 4.17 shows an image taken after another 0.25 sec. In this image, the accumulated oil has been completely washed away onto the second compression ramp, and all evidence of the separation line has been destroyed.

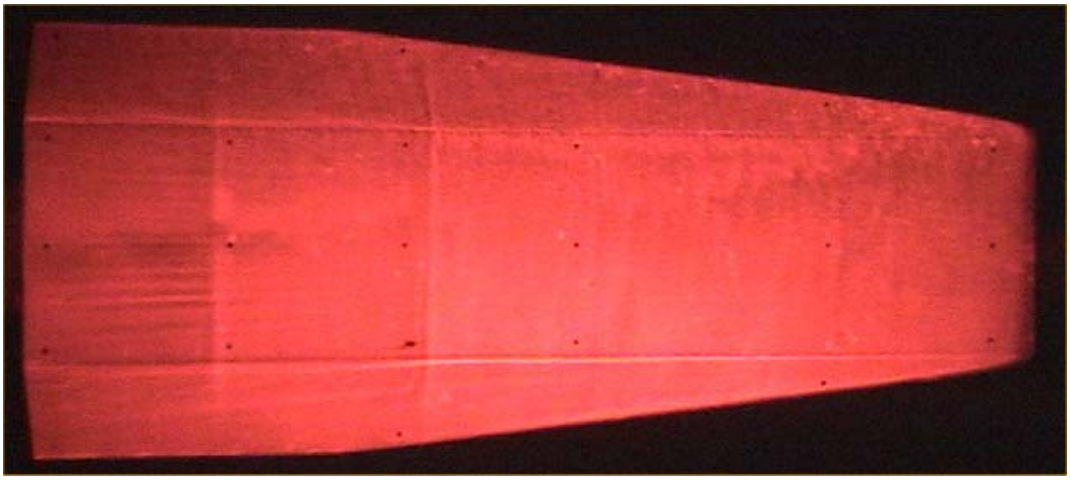

Figure 4.14. Oil-flow image clip taken immediately after tunnel startup.

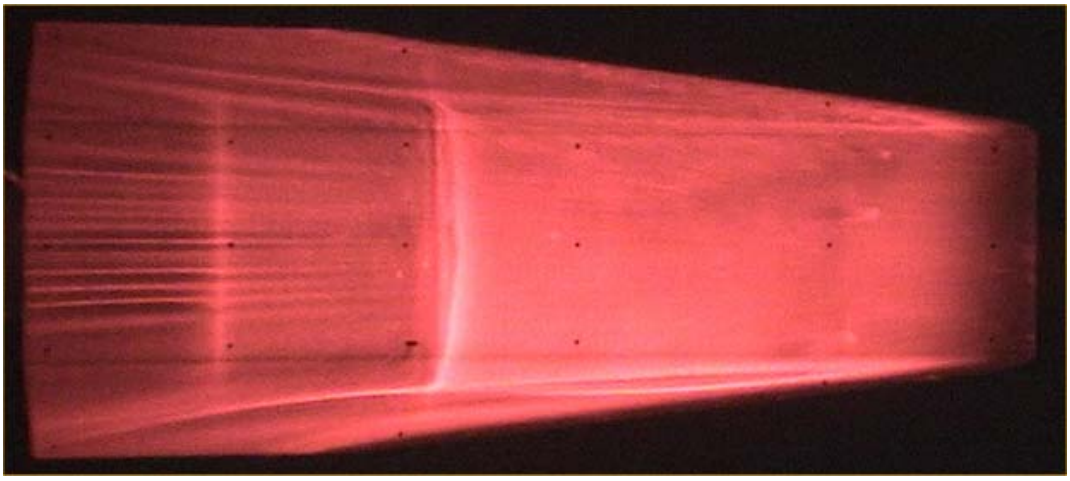

Figure 4.15. Oil-flow image clip taken 6.5 sec. into the tunnel run.

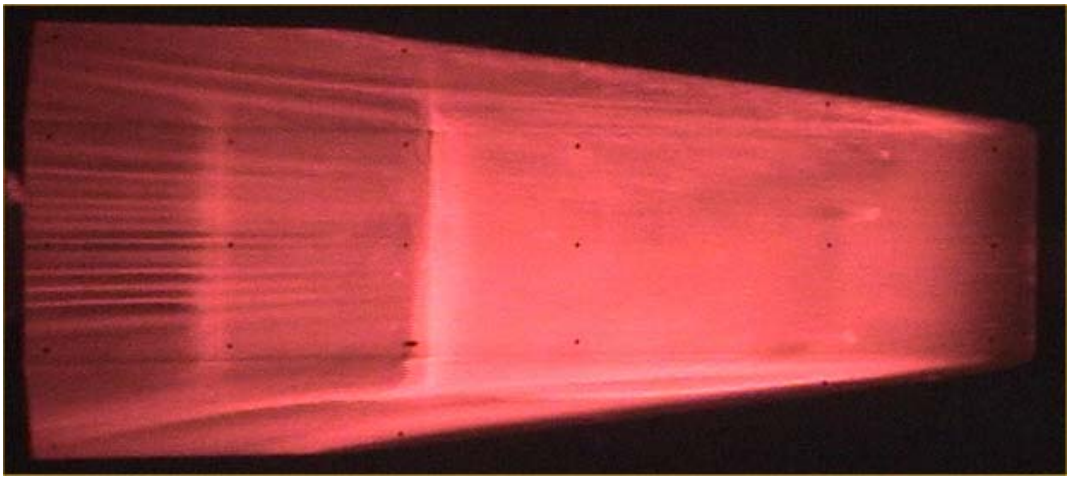

Figure 4.16. Oil-flow image clip taken immediately after tunnel unstart.

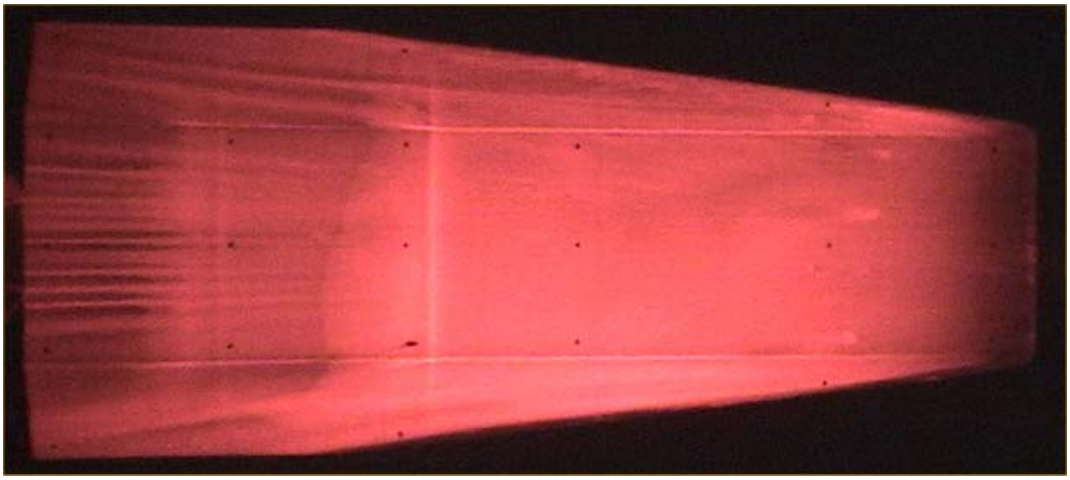

Figure 4.17. Oil-flow image clip taken 0.5 sec. after tunnel unstart.

5. IMAGE PROCESSING TECHNIQUE

5.1 Image Processing Overview

The ratio of the wind-on and wind-off images is used to obtain the temperature distribution on the model. However, this process will always show misalignment of the two images to some degree, due to model motion relative to the camera. In general the misalignment is usually caused by deflection of the model under aerodynamic load. Ref. [92] notes that this is usually the dominant error source in experiments performed using TSP. This misalignment must be corrected using image registration techniques. The aligned images must then be mapped to a grid so that the image coordinates can be related to model coordinates, using resectioning techniques. For the facility used for this research, the distortion of the image caused by the curved surface window must also be corrected.

Image registration requires calibration points in the wind-off and wind-on images, so that one image could be mapped to the other. Resectioning methods in addition require that model coordinates of the registration points be known. Natural model features such as junction points and wing tips are convenient to use, but when there are not enough such points, then registration marks must be added. These fiducial marks placed on the model are then used to construct equations that relate the coordinates of one image to another. Several basic classes of equations have been used in the past, such as the projective transform [93], the general power series [56, 94, and 95], the general polynomial series [89], and Delaunay triangulation [96, 97]. The general form of these equations is shown in Equations 5.1-5.4 respectively.

$$x = \frac{a_1 x' + a_x y' + a_3}{c_1 x' + c_2 y' + 1}, \; y = \frac{b_1 x' + b_x y' + b_3}{c_1 x' + c_2 y' + 1} \qquad \text{Projective Transform} \quad (5.1)$$

$$(x, y) = \left(\sum_{i,j=0}^{m} a_{ij} x'^{i} \, y'^{j} \, , \sum_{i,j=0}^{m} b_{ij} x'^{i} \, y'^{j} \right) \qquad \text{Power Series} \quad (5.2)$$

$$x = a_{00} + a_{10} x' + a_{11} y' + a_{20} x'^{2} + a_{21} y'^{2} + a_{22} x' y' + \ldots \qquad \text{Polynomial Series} \quad (5.3)$$

$$y = b_{00} + b_{10} x' + b_{11} y' + b_{20} x'^{2} + b_{21} y'^{2} + b_{22} x' y' + \ldots \qquad \text{Polynomial Series} \quad (5.4)$$

The aligned images are then mapped onto the surface coordinates using resectioning methods. Various techniques are available here as well, such as the affine transformation [89], perspective and isometric projection [99], and the direct linear transformation (DLT) [95, 100], which is a reduced form of the collinearity equations of photogrammetry. More sophisticated methods that involve techniques from fields such as computer vision are also being developed, and the theoretical foundations for such techniques are discussed in Ref. [101]. The DLT is quite useful because of its simplicity compared to the full collinearity equations, which requires sophisticated camera calibration and determination of the optical and geometrical properties of the imaging system [102]. On the other hand, simple calibration techniques and modeling of lens distortion effects for the DLT are readily available [94, 103, and 104].

5.2 Image Processing Approach

The two image processing steps were combined into a single step for the images acquired in this research. The wind-off and wind-on images, which showed at most a few pixel misalignments, were directly mapped to a two-dimensional grid. The grid was constructed by isometrically projecting the coordinates of the registration marks to a plane perpendicular to the back surface of the model. This grid construction technique essentially eliminates the z-coordinate of the registration marks, or the depth of the marks in and out of the image. This allows the entire image processing to be done in only two dimensions. This method does not require the use of more sophisticated and difficult resectioning methods either. The process appears as if an image registration step is being

performed, except that the coordinate to map the wind-off and wind-on images onto is the two-dimensional grid and not another image.

The Hyper-2000 geometry is essentially three flat plates at angles of attack, which is relatively simple compared to full aircraft geometries. For the Hyper-2000 geometry the simpler affine transformation and projective transform are very well suited. One concept would be to apply three sets of different transformations to each of the compression ramps. However the distortion from the window adds curvature effects into the image misalignment, which cannot be corrected using the affine transformation, which only takes into account magnification, translation, and rotation. Thus the power or polynomial series must be used. The unknown coefficients can be solved for each set of images by constructing a system of linear equations using the locations of the registration marks and the corresponding grid points. The advantage of this method is that very few fiducial marks are required, enough to solve the unknown coefficients. A second approach is to use more marks than there are unknowns, and solve the overdetermined system in a least squares sense. This method gave better results, and was adapted for this set of experiments, using the simulated annealing algorithm for the least squares fitting [105]. This particular version was significantly more user-friendly and efficient compared to the more readily available routine from Numerical Recipes [106].

5.3 Validation of Image Processing Approach

This image processing method was validated and tested on a set of sample images acquired on the Hyper-2000. The samples were processed specifically for this purpose, and all discussion here will focus on the image processing. In addition to the validation, a systematic attempt was made at understanding the optimal locations for the registration marks. The general rule of thumb is to spread out the marks throughout the image, and place them where the image movement is the largest. For this test experiment, more registration marks were applied than would generally be needed. The locations of the marks are shown in Figure 5.1. The third row of marks is placed on the centerline, and the rows above and below are near the edges of the compression surface. The top and

bottom rows are placed near the edge of the chines. A total of 56 marks were distributed throughout the model surface as evenly as possible, using a thin felt-tip permanent marker mounted in a milling machine with a coordinate readout display. In fact this was the standard method to apply the marks whenever the TSP was repainted.

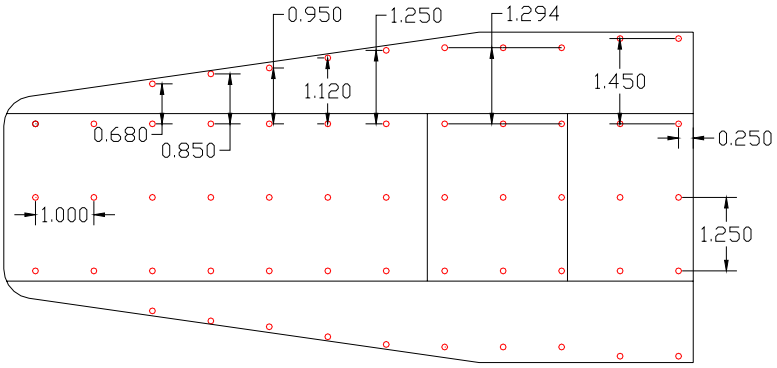

Figure 5.1. Locations of the registration marks used in the validation and optimization of the image processing method. All dimensions are in inches.

The wind-on and wind-off images from a particular set of experiments showed an rms misalignment by about a pixel. All 56 marks were used to compute this misalignment value. The misalignment of the wind-off and wind-on image is illustrated in Figure 5.2. The registration marks are clearly visible in this intensity ratio, showing that a misalignment of even a pixel results in significant effects. If the two images were perfectly aligned, then the marks should effectively cancel out.

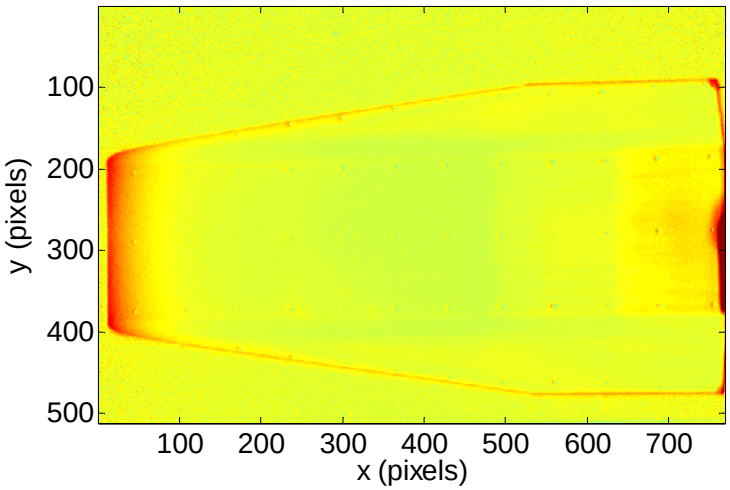

Figure 5.2. Intensity ratio of the wind-off and wind-on image, showing the misalignment.

The misalignment of the marks in the images to the specified grid coordinates is generally much larger than the misalignment between the wind-on and wind-off images. The particular dataset shown in Figure 5.2 has a rms misalignment of 10.8 pixels against the grid. The specified grid coordinates of each registration marks are added to the image in Figure 5.3.

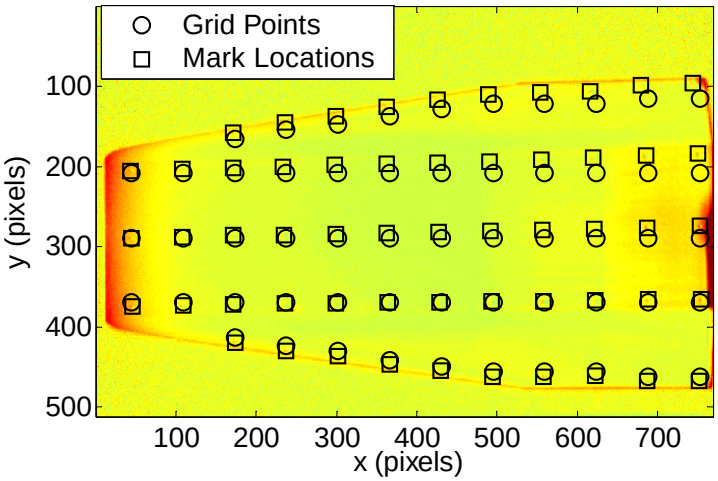

Figure 5.3. Intensity ratio of the wind-off and wind-on image, with the coordinates of the corresponding registration marks in the grid.

Many of the registration marks do not align with the marked grid coordinates. This misalignment results mostly from the distorting effect of the window, but also from the fact that the camera is not oriented perfectly perpendicular to the image. The misalignment is much more significant vertically because the window acts as a cylindrical lens and stretches the image in that orientation.

An optimization routine was used to attempt to optimize the locations of the registration marks, for a particular type and order of an image registration equation, and a set number of desired points to use. This discrete variable optimization was performed using the genetic algorithm routine [107]. This particular routine uses tournament selection and uniform crossover approach to generate subsequent populations. Each registration mark was a design variable represented by a bit, to “turn on” or “turn off” using that particular registration mark. The chromosomes for the design bit-string are coded using the gray coding technique. A standard penalty function was used to enforce the number of points to use. The objective function was the rms misalignment of the

marks to the grid, computed from using all 56 registration marks after applying the image registration equation. The image registration equation was constructed from the number and locations of the marks as determined by the optimization routine. The fitness function is shown below in Equation 5.5 and 5.6.

$$I = P_{rms} + z * MAX[\frac{Npts}{Ntotal} - 1,0] \qquad \text{if } N_{pts} > N_{set} \tag{5.5}$$

$$I = P_{rms} + z * MAX[\frac{Ntotal}{Npts} - 1,0] \qquad \text{if } N_{pts} < N_{set} \tag{5.6}$$

Here, P_{rms} is the rms pixel misalignment or the objective function, z is the penalty factor, N_{pts} is the number of points used to construct the image registration equation as determined from the iteration by the optimization routine, N_{total} is the total number of registration marks, and N_{set} is the desired number points to use in constructing the image registration equation. A penalty factor of 0.01 was used for all cases investigated, and seemed to enforce the number of points to use effectively. The optimization was stopped when the best fit did not improve over 5 generations.

The number of marks used ranged from only three for the lowest order equation tried, up to all of the points available. Four equation forms were tried, the 1st and 2nd order polynomial, the 1st order power series, and the projective transform. The specific forms of the polynomial and power series equations are shown below in Equations 5.7-5.12 respectively. Higher order equations were initially tried, however for this particular image they had too many degrees of freedom, which introduced waviness, and actually resulted in a larger misalignment than the unprocessed images.

$$x = a_0 + a_1 x' + a_2 y' \tag{5.7}$$

$$y = b_0 + b_1 x' + b_2 y' \tag{5.8}$$

$$x = a_0 + a_1 x' + a_2 y' + a_3 x' y' + a_4 x'^2 + a_5 y'^2 \tag{5.9}$$

$$y = b_0 + b_1 x' + b_2 y' + b_3 x' y' + b_4 x'^2 + b_5 y'^2 \tag{5.10}$$

$$x = a_0 + a_1 x' + a_2 y' + a_3 x' y' \tag{5.11}$$

$$y = b_0 + b_1 x' + b_2 y' + b_3 x' y' \tag{5.12}$$

The resulting rms pixel misalignments from this optimization problem are summarized in Figure 5.4. Up to a certain point, the results improve as the number of points in use is increased, but then when too many points are used, the misalignment actually increases significantly. This shows that there are an optimal number of points to include when constructing the image registration equations.

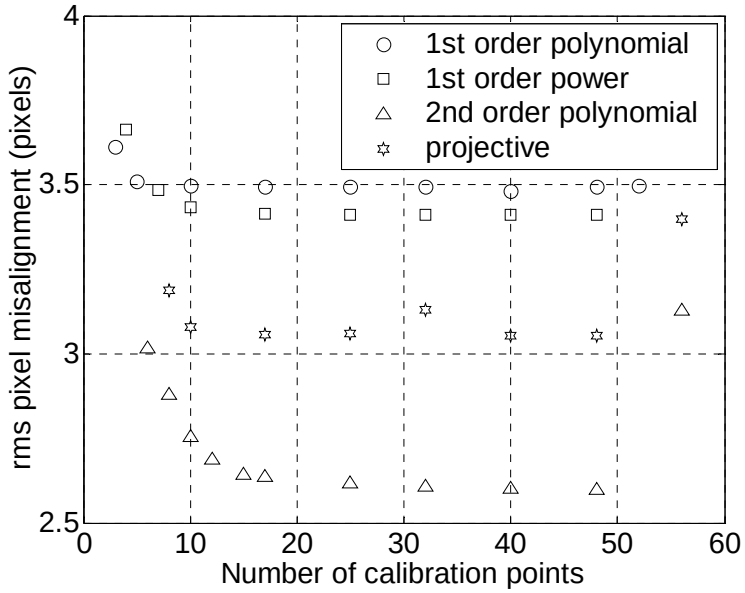

Figure 5.4. RMS Pixel misalignment after applying the image registration equations for the optimized mark locations.

The 2nd order polynomial consistently results in the least misalignment, followed by the projective transform. As expected, both the 1st order polynomial and the power series result in the least performance, because they cannot correct the curvature effects. As noted above, the sum of the grid misalignment of the raw wind-off and wind-on images was about 12 pixels. The 2nd order polynomial reduces this by a factor of about 5, and was adapted as the standard method for this research. It was also decided that using about 15 or more registration marks is good enough. The genetically-optimized mark coordinates are shown in Figure 5.5, for the cases where 6, 12, and 17 marks were used. All three of these cases were done for the 2nd order polynomial equation. The plot does not show any clear pattern as to which specific marks have the dominant effects. All three cases however do show a distribution of marks throughout the model surface, and are not all concentrated on a particular region of the model. This probably leads to the

conclusion that the number of marks being used and the type of image registration equation has the dominant effect on the alignment achievable, and that the location of the individual marks is of secondary importance, as long as the marks are distributed evenly along the model.

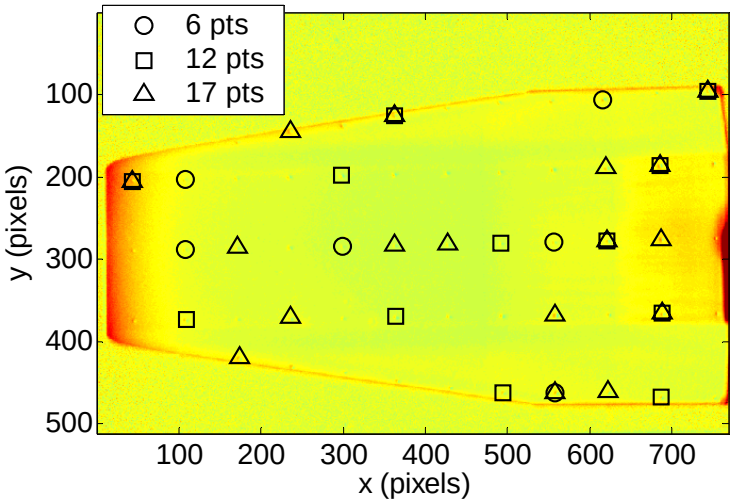

Figure 5.5. Optimized registration mark locations for the 2nd order polynomial image registration equation.

The image shown in Figure 5.2 and 5.3 were corrected using the 2nd order polynomial, calibrated using 41 points. The resulting image is shown in Figure 5.6. The registration marks that were clearly visible before are now effectively gone. This is due to the better alignment of the wind-off and wind-on images. This also reduces the noise level of the image, resulting in a smoother and sharper image.

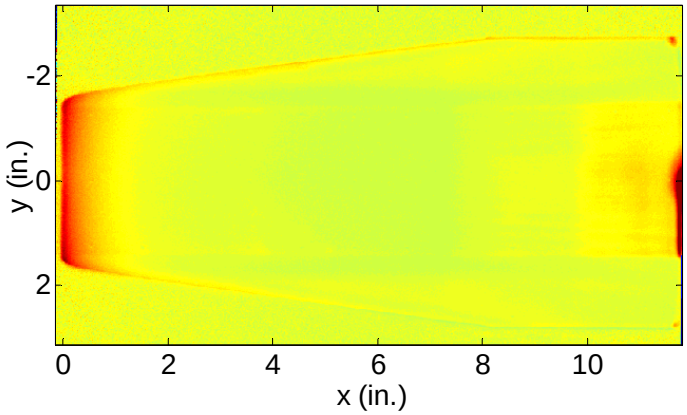

Figure 5.6. Intensity ratio image corrected using the 2nd order polynomial with 41 registration marks for calibration.

The horizontal edges of the model are now more or less straight, unlike before where a curvature and a vertical drift could be seen. The same is true for vertical edges as well, such as the leading edge and the compression corners. These effects result from correcting for the distortion from the window, and by virtually moving the camera position so that it is viewing the model perpendicular to the centerline. Most importantly, a dimensional coordinate can now be placed on the axis, which allows for quantitative spatial determination of any points of interest in the image.

A quantitative comparison of the uncorrected and corrected images is shown in Figure 5.7. Here, the centerline intensity-ratio distribution is shown, which was computed by averaging 275 pixel rows on the compression ramps. For both cases, the same pixel rows were used. The intensity ratios are more or less the same for the two cases up to about 4.5 in. The disagreement becomes significant on the third compression surface, which starts at about 9.5 in. The uncorrected case gives a significantly higher intensity ratio, which would correspond to a higher temperature and heat transfer rate.

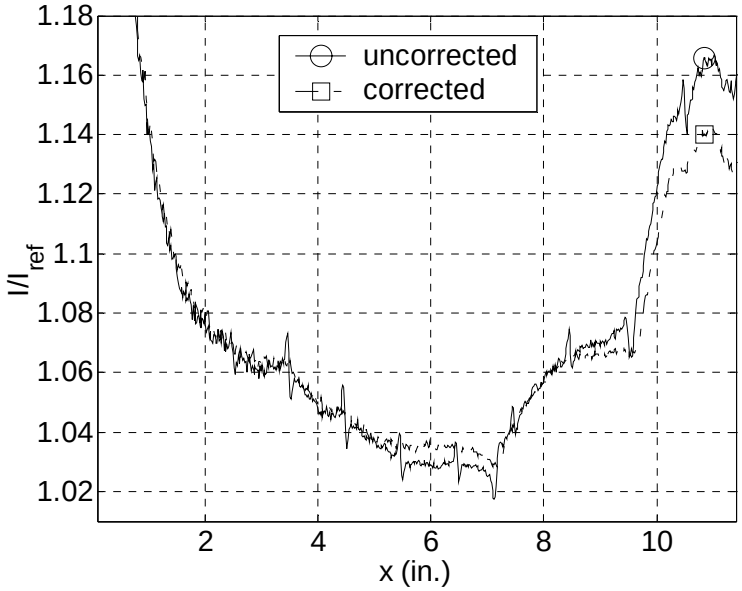

Figure 5.7. Comparison of the centerline intensity ratio distribution for the uncorrected and corrected images.

The uncorrected case also shows the regular occurrences of spikes. These are the results from the misalignment of the registration marks. The registration marks are about 4 pixels in width in the images, and there are three marks at each streamwise station on the

compression ramps. This means that out of the 275 rows of pixels averaged, 12 rows contain pixels for registration marks. This is only 4 % of the total number of pixels being averaged, but still has a significant effect on the overall results. This shows that image misalignments not only result in spatial uncertainty of the images, but also in the uncertainty of the quantitative heat transfer rates as well.

These images and results show the effectiveness of the image processing technique adapted for this research. The technique is not as sophisticated as might be preferred, but is simple to apply and works pretty well for this simple model geometry. However an even better alignment, on the order of a tenth of a pixel, should be achievable with the full DLT equations and this would be a logical improvement that should made in future experiments.

6. DATA REDUCTION MODEL

6.1. Heat Transfer Rate Model

The measured temperature distribution on the model is used to compute the heat transfer rate distribution. The unsteady heat transfer rate is governed by the semi-infinite one-dimensional heat conduction equation, shown in Equation 6.1.

$$\frac{\partial T}{\partial t} = \alpha \frac{\partial^2 T}{\partial y^2} \tag{6.1}$$

Here T is temperature, t is time, y is the distance from the surface, and α is the thermal diffusivity of the paint material. This form assumes that the thermal properties are constant within the paint layer. A diagram corresponding to this model is shown in Figure 6.1. The model is assumed to stay at a constant temperature, and that the temperature-sensing layer is thin compared to the insulating layer.

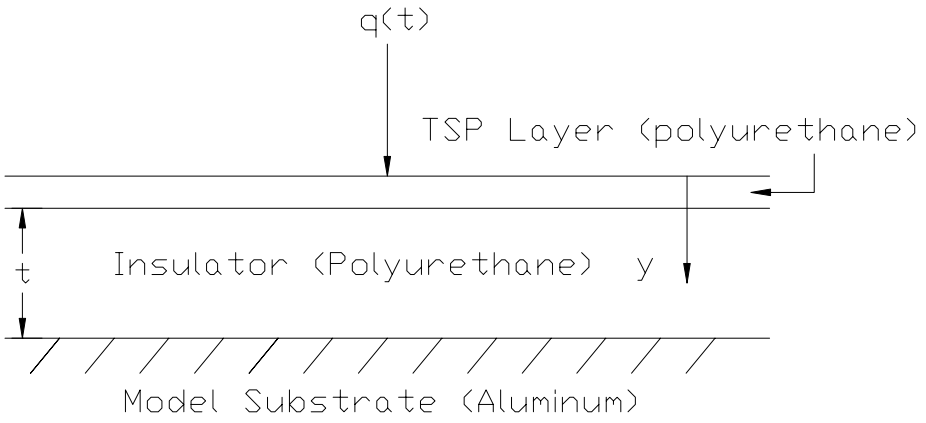

Figure 6.1. Thermal model of the heat transfer rate.

Various simplified forms of the partial differential equation governing the heat transfer process have been used to compute the heat transfer rates for various

measurement techniques. Ref. [108] outlines several models and assumptions that can be used, ranging from the simplest analytical forms to a full finite-volume numerical technique. For TSP experiments performed in the past, two techniques seem to be especially popular, the discrete Fourier Law [55, 58, 59, 61, 85, 109, and 110] and the transient model for unsteady heat transfer rates [55, 60, 84]. For this research the discrete Fourier Law is used, which is shown in Equation 6.2.

$$q = \frac{k}{t}(T - T_M) \tag{6.2}$$

Here, q is the heat transfer rate, k is the thermal conductivity, t is the insulator thickness, T is the temperature measured during the tunnel run, and T_M is the model substrate temperature.

This heat transfer model is advantageous in that it is very simple, and all of the required parameters can be measured with the current equipment and instruments available. The unsteady model on the other hand requires multiple images taken within a very short time frame to obtain accurate temperature gradients with respect to time. However, the CCD camera and acquisition system used is limited to about an image every 1 to 1.5 sec. Also, Ref. [110] compares the heat transfer rates computed using the discrete Fourier Law with that of a more sophisticated model, taking into account effects such as the finite thickness of the insulator and the heating from the front and back surfaces. The results agree very well, validating the use of the simpler model.

The modeling of the heat penetration process using the discrete Fourier Law results in a linear temperature profile with depth into the insulator. The response time τ of the TSP, which is a measure of how long it takes for this profile to form and reach steady state conditions, is given in Equation 6.3.

$$\tau \propto \frac{t^2}{\alpha} \tag{6.3}$$

For typical paintings the insulator is 3-5 mils thick, which result in a response time of about 0.01-0.06 sec, using a thermal diffusivity of 2.7×10^{-6} m^2/s, which is a binder

material property [86]. The unsteady startup process of the tunnel usually takes about 0.25 sec., so ideally an image should be taken about 0.3 sec. after the diaphragms burst. The imaging system however must be triggered manually at this time, and cannot be controlled to this precision. A triggering system to initiate the imaging should be developed in the future, so that the timing of the image acquisition can be controlled as desired.

6.2. Measurements and Treatment of the Insulator Thickness

The thickness of the paint layer was measured using Elcometer's Model 456 Coating Thickness Gauge, which uses the electromagnetic induction principle and the eddy current principle for measurements over magnetic and non-magnetic bases respectively. Measurements are taken at regularly spaced intervals along the model surface. Generally 400-500 total measurements are taken when a measurement is made about every 0.25 inches across the spanwise and streamwise coordinate. However, the measurement locations are not precisely controlled at the moment because the measurements are done by hand. The spatial coordinates of the measurement locations are accurate to only about an eighth of an inch. This however can be improved in the future by mounting the measurement probe in a milling machine with a digital readout. A CNC milling machine might also be used to automate the measurement process. This would significantly reduce the model preparation time.

The spatial variation of the insulator thickness varies for each painting, and it is difficult to quantify this variation in any general way. Some representative measurements for five painting trials are listed in Table 6.1. The mean insulator thickness and the RMS variation are quite consistent for different paintings. However, the maximum and minimum thicknesses can vary by almost a factor of two. The spatial variation for each painting can also differ significantly as well, which is not reflected in the data shown in Table 6.1.

Table 6.1. Overall insulator thickness variation for several painting trials.

Painting Trial #	Mean Thickness (mils)	Maximum Thickness (mils)	Minimum Thickness (mils)	RMS (mils)
1	3.36	7.7	0.98	0.70
2	3.21	8.7	0.9	0.97
3	3.21	4.79	0.09	0.65
4	3.54	6.8	1.54	0.96
5	3.45	5.5	1.78	0.76

The insulator thickness variation can be taken into account to various levels of sophistication when using the discrete Fourier Law, the simplest being a single mean value of the thickness for the entire image. However, the paint layer thickness might vary by a factor of two or so, which would introduce significant error into the computed heat transfer rates. Another method would be to use the average thickness for a particular region of the model, or for a range of coordinates. The windward surface of the Hyper-2000 is composed of five convenient surfaces, the two chines and the three compression ramps. A mean thickness can be measured for each of these surfaces, with this mean value used in the analysis. This probably would reduce the uncertainty compared to the first method, but the change in the thickness causes a discontinuity in the computed heat transfer rate distributions at the boundary between surfaces. The most sophisticated method is to measure the thickness at several controlled locations and create a look-up table of the thickness, or a thickness grid. Although this takes significantly more time than the previous methods, the error caused from the uncertainty in the thickness might be minimized.

A sample grid of the insulator thickness is shown in Figure 6.2. A false-color scale is used to illustrate the variation of the insulator thickness. This particular grid is composed of 495 measurements made only on the compression ramps. The thinner coating thickness very close to the two compression corners around 7.25 and 9.65 in. can actually be seen as faint vertical blue lines. Also shown in Figure 6.2 is a finer grid

constructed by a two-dimensional interpolation and extrapolation of the measured data. The thick and thinner spots in the paint layer are clearly illustrated. This process illustrates how the thickness measurements can be interpolated and applied to the acquired images. More sophisticated schemes such as bicubic and spline interpolations were tried, but these methods failed near the edges due to their nonlinearity, and overall the linear scheme seemed to be the most robust.

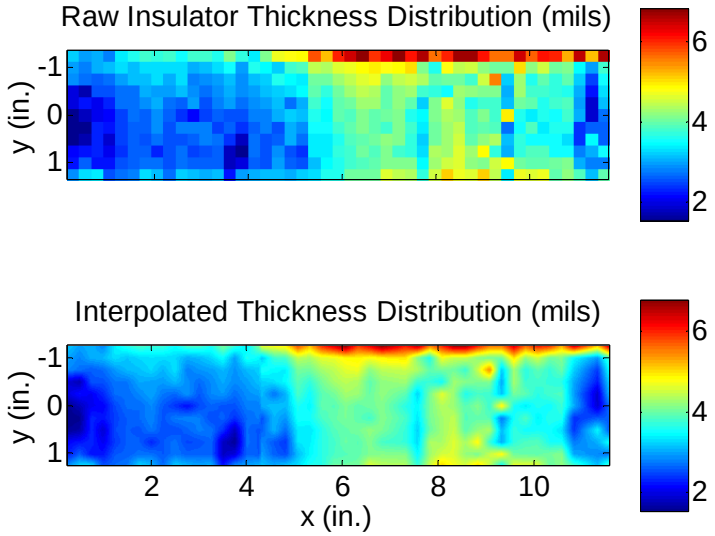

Figure 6.2. A typical coating thickness grid constructed from raw measured data and from interpolation of the raw data.

The qualitative effects on the heat transfer rate distribution of using the three treatments of the insulator thickness are illustrated in Figure 6.3. The total pressure, temperature, and unit Reynolds number for this run was 114.7 psia, 425 deg. K, and 2.48 million/ft respectively. The model was initially at 26.5 deg C, and the wind-on image was taken 0.9 sec. after tunnel startup. The first image uses a mean thickness value of 3.54 mils, the second image uses mean thickness values of 3.23, 4.28, 3.70, and 3.54 mils for the compression ramps and chines respectively, and the third image uses the thickness grid. The first image is very smooth, and the overall nature of the aerodynamic heating is clearly seen, with the high heating at the leading edge which quickly decreases downstream with the growing boundary layer, and then the heating increases with each compression corner. With the second method, the five separate regions used are clearly

visible. As expected, the discontinuous thickness distribution results in the discontinous levels between each region. The third image uses the thickness grid on the compression ramps, which is extrapolated out to the chine regions since no measurements were taken on the chines. The variation in the thickness again causes significant variations in the heat transfer rates. The correlation between this image and Figure 6.2 is evident. The thinner spots in Figure 6.2 show up as high heating areas in this image, and vice-versa. These variations will obscure the much smaller variations in the heat transfer rates caused by streamwise vortices, hindering the quantitative analysis of the stationary instabilities.

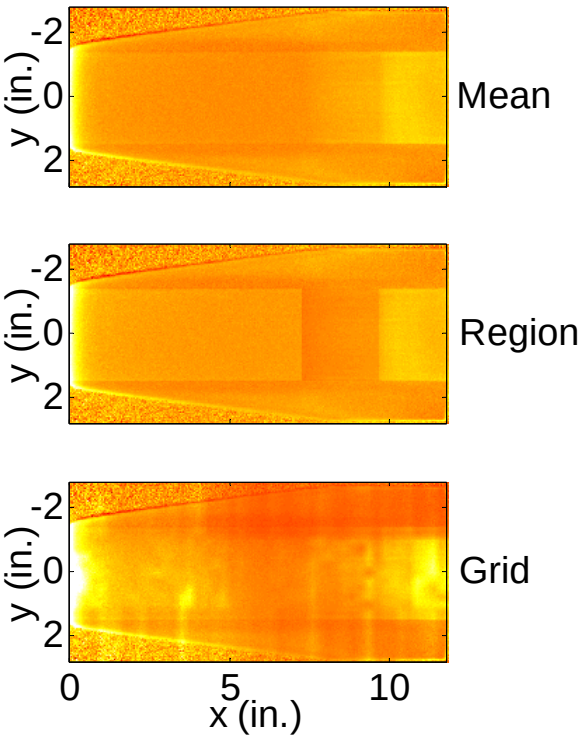

Figure 6.3. Heat transfer rate distributions computed with three different treatment of the insulator thickness distributions.

A quantitative comparison of the data shown in Figure 6.3 is shown in Figure 6.4. The heat transfer rates are plotted against the centerline coordinate. Each set of data is the spanwise average of 171 pixels. The data for the first two methods results in nearly an identical heat transfer distribution on the first ramp. However, in the second method, the discontinuous increase in the insulator thickness on the second ramp causes the heat transfer rate to discontinuously decrease. The third method contains several false peak

heating points, and it is even arguable that the trends are not correct either. The locations of the two compression corners are evident from the heating increase in the first technique, but this is not clear in the third technique. Also, the leading edge heating is greater by about 50 % compared to the first two methods. The significant differences in the heating distributions computed from the three methods, and the nature of these differences, makes it difficult to quantify the uncertainty in the heat transfer rates in terms of a single error value.

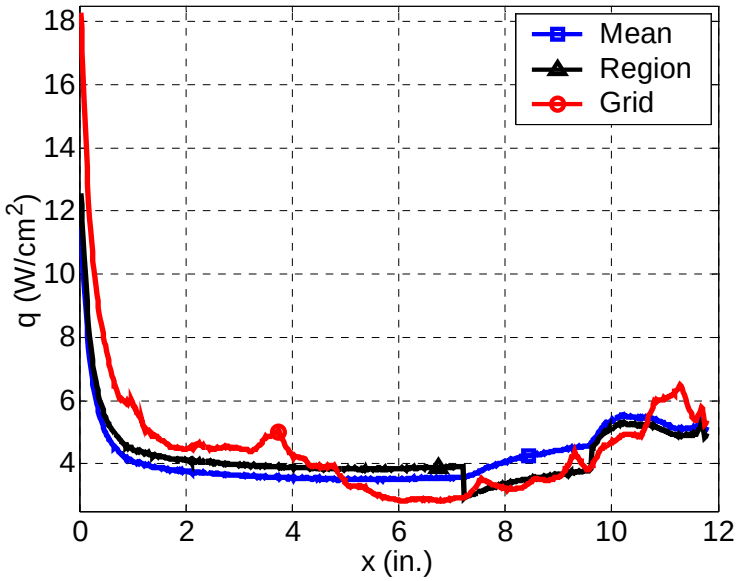

Figure 6.4. Comparison of the centerline mean heat transfer rate distributions on the Hyper-2000 compression ramps using various approximations of the insulator thickness.

In principle, the third method shown above should result in a smooth heating distribution. The regions where the insulator is thicker should result in a higher model surface temperature compared to the regions where the insulator is thin, for the same heat transfer rate. The two effects should effectively cancel each other out when the heat-transfer rate model is applied, resulting in a smooth heat-transfer rate distribution. Thus, the heat transfer variation seen with the third approach is the result of the temperature variation being significantly less than the insulator thickness variation. This might be caused by two possible issues. First, two-dimensional conduction effects might be significant enough to smooth out the measured surface temperature distribution. Second, the insulator material may not have a low enough thermal conductivity for the surface

temperature to increase linearly with the insulator thickness within the conditions of these experiments. This would also result in a smooth surface temperature distribution. However, it is clear that the first method will result in the cleanest data when analyzed for instability growth. Although using a single mean insulator thickness value is not desirable in some ways, this method was still preferred for the present research.

6.3. Comparison of Mean Heat Transfer Rate to Hyper-X Measurements

The mean heat-transfer rate distribution along the streamwise coordinate at two unit Reynolds numbers are compared to previously published CFD data [41] in Figure 6.5. The data only on the first compression ramp is shown, where the boundary-layer is most likely laminar. The data presented is a spanwise average at each streamwise location. The streamwise coordinate is normalized by the full vehicle length at the model scale, and the heat-transfer rates are normalized by the Fay and Riddell stagnation point heat-transfer rate [112] on a one-foot radius sphere scaled to the model size. The figure reveals two unexpected problems with the current data. The experimental heat-transfer rates are higher than the computations by an order of magnitude, and the data for the two unit Reynolds numbers show significant variations.

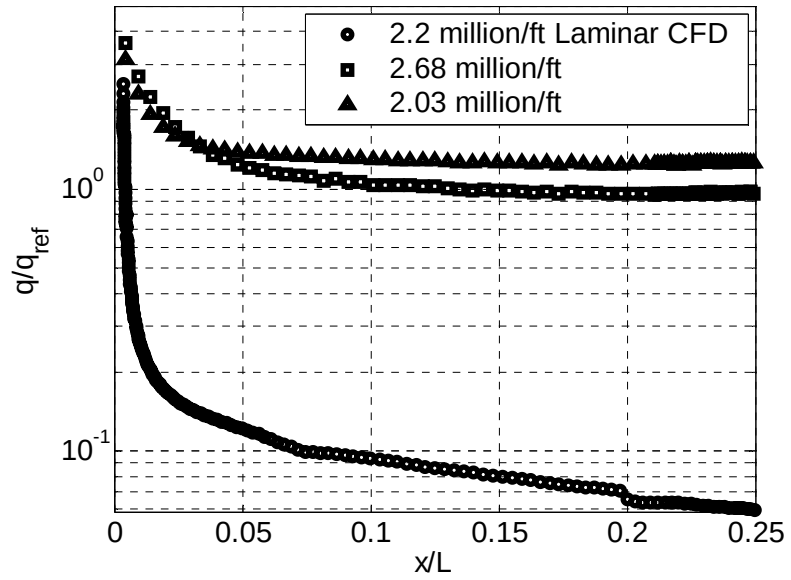

Figure 6.5. Comparison of the measured mean heat transfer rates on the Hyper-2000 to the measurements and laminar CFD data on the Hyper-X.

Four possible sources of these discrepancies have been identified and are listed below, along with possible approaches to resolve the problem.

1. The leading edge geometry of the model is different from the leading edge geometry used for the computations. The Hyper-2000 model's leading edge thickness varies significantly, whereas the computations used a smooth leading edge with a nose radius. Reworking the leading edge may result in a flowfield that resembles the computational results more closely.
2. The uncertainty in the computed heat-transfer rate is directly proportional to the insulator thickness variation. Instead, use an adhesive tape which would provide a constant thickness for the insulator. However, applying tape to this model is not trivial, since the geometry is three-dimensional with surface curvature, corners, and breaks. Using multiple pieces of tape is also not an option, because any gaps or steps would generate undesired disturbances which will contaminate the instability measurements.
3. The temperature of the model increases significantly between tunnel startup and image acquisition. This is especially likely near the leading edge where the model is very thin. Apply insulating material to the leeward side to reduce the net heating to the model. Use a more sophisticated heat-transfer model where unsteady, multi-layer, and multi-dimensional [113] effects are modeled.
4. The measured temperature distribution during the run is significantly higher due to the pressure sensitivity of the TSP. The effect of pressure on the TSP luminescence is small between atmospheric and vacuum pressures, but the sensitivity from vacuum to high pressures is not known. If the response time to pressure is on the order of seconds (due to the slow oxygen diffusion in the binder), then it might be more accurate to take the wind-off image at high pressure rather than at vacuum.

Currently the fourth point above is suspected to be the dominant error source. This issue was investigated by comparing two TSP images taken at no-flow conditions, with pressures of 0.05 and 127 psia. The model temperature was allowed to equilibrate

for a few hours, and for both images the model temperature was 28.4 deg. C. The ratio of these two images is shown in Figure 6.6. Because the two images are taken at the same temperature, the intensity ratio should more or less be 1.0, if there is no pressure effect. However, the figure shows that the image taken at 0.05 psia is about 30 % brighter than the image taken at 127 psia. This would result in significantly different surface temperature measurements and computed heat-transfer rates, depending on what pressure the wind-off image is taken at.

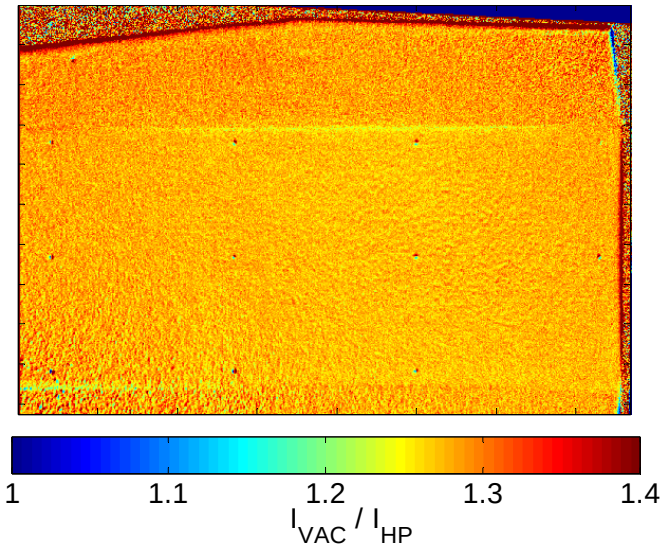

Figure 6.6 Ratio of TSP images taken at no-flow condition, with a temperature of 28.4 deg. C and pressures at 0.05 and 127 psia.

This effect is illustrated in Figure 6.7. Here, the normalized heat-transfer rate is shown near the first compression corner. As with Figure 27, the experimental data shown is an average over the span of the ramp portion. Depending on the pressure condition of the wind-off reference image, the heat-transfer rates are significantly different. The effect is large enough to change the sign of the heat-transfer rate. This data also implies that the response time of the TSP to pressure may need to be taken into account, since using a wind-off image at full stagnation pressure under-predicts the heating, and the use of a wind-off image at vacuum over-predicts the heating. Despite these problems, instability analysis was carried out on the available data using a wind-off image at vacuum. The fluctuating component of the spanwise heat-transfer rate distributions are normalized by

the mean heat-transfer rate. This should factor out most of the error, as long as the error in the mean heat-transfer rate is present in the magnitude of the fluctuations as well.

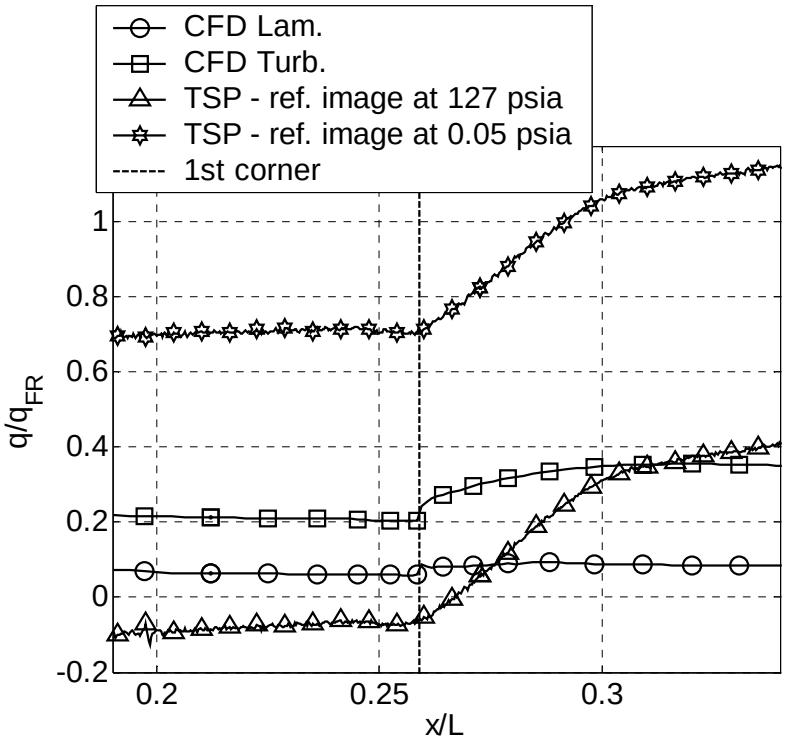

Figure 6.7. Comparison of the heat-transfer rates using a wind-off image taken at 0.05 and 127 psia to CFD data.

6.4. RMS of the Spanwise Heat Transfer Rate Fluctuations

The measured heat transfer rate distribution will show striation marks developing on the model surface, depending on the conditions. In order to relate these streamwise vortices to the instability of the boundary layer, the growth rate must be quantified, which requires some sort of a measure of the vortex amplitude. The amplitudes of the vortices can be compared along the model to obtain a growth rate. This concept is very similar to the cross-flow instability measurements that were made on a swept-wing at low speed [111]. This technique will be illustrated using a sample obtained from one of the earlier sets of data. A sample image of the heat-transfer-rate distribution is shown in Figure 6.8. The total pressure, temperature, and the unit Reynolds number were 105.3 psia, 396 deg. K, and 2.57 million/ft respectively. The initial model temperature was not measured for

this run, but is assumed to be 27 deg. C. The experimental uncertainty for this particular run is not known, but should not be a problem since the discussion here will focus only on the data extraction techniques. The heat-transfer-rate distribution was computed using multiple insulator thicknesses for each of the three compression ramps. However, a step is not visible across the two compression corners in this image because the mean insulator thickness does not change enough across the corners to show a significant discontinuity in the heat-transfer rate. The mean insulator thicknesses were 2.95, 3.65, and 3.99 mils respectively for the first, second and third compression ramp.

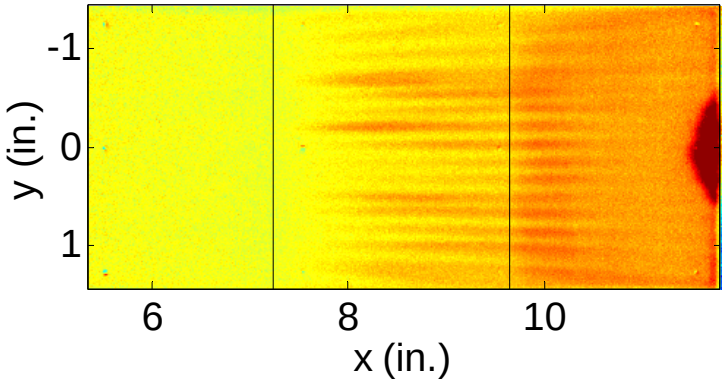

Figure 6.8. Heat transfer rate distribution on the Hyper-2000 near the compression corners.

The development of striation patterns past the first compression corner is clearly visible. These striations are the instabilities of interest. The high heating spot at the trailing edge was the result of an older model sting, which protruded past the windward surface, causing a stagnation region. Two methods have been used to quantify the amplitude of the instability, the simpler being an RMS of the fluctuating component of the heat transfer rate distribution (q'_{RMS}). This technique is relatively simple to use, but has the drawback that only the magnitude of the fluctuation is quantified, and not the wavenumber. The second approach is a spectral analysis of the heat transfer rate fluctuations. This can isolate the individual wavenumbers of importance and the magnitude as well.

For the RMS technique, the fluctuating component of the spanwise heat transfer distribution must be extracted from the images. This is done either by using a single pixel column, or by taking the average of several adjacent columns. Averaging several

columns reduces the noise level significantly, at the expense of spatial resolution. This averaging effect is illustrated in Figure 6.9. Here, the spanwise heat transfer rate distributions are shown at three streamwise stations at representative locations on each of the compression ramps. When only a single column is used, the distribution is quite noisy. As the number of averaged columns increases, the fluctuations become better defined.

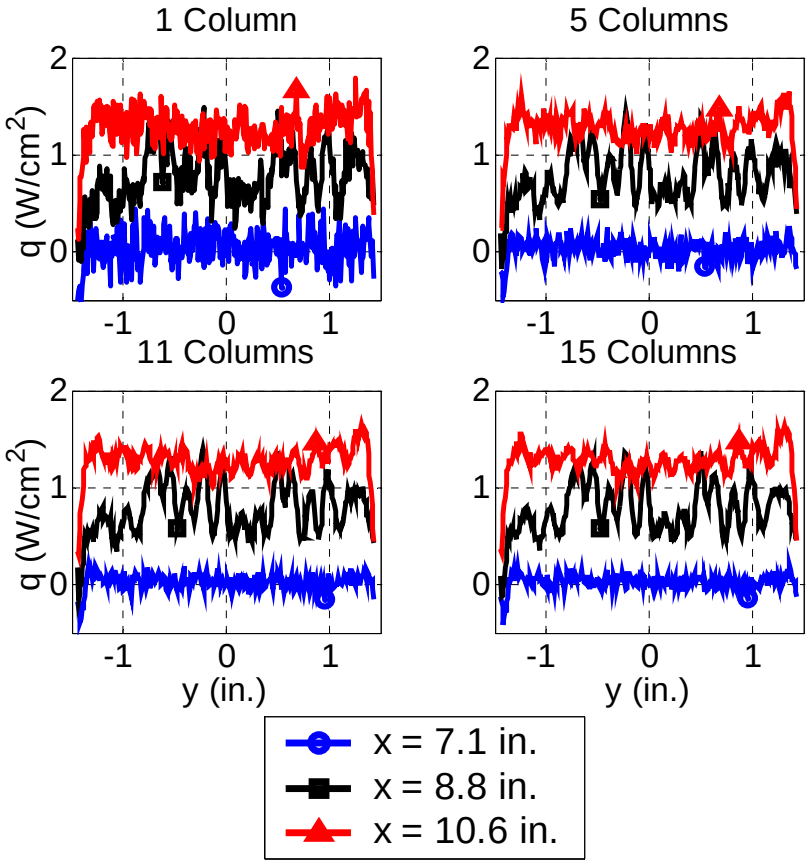

Figure 6.9. Effect of averaging multiple columns to obtain the spanwise heat transfer rate distribution at representative streamwise stations.

This is very clear on the first ramp, where the fluctuations have not developed to a large enough amplitude, and the heating level stays constant. Also, the oscillations on the second and third ramp become clear only with five or more columns averaged. There does not seem to be much of a difference between 11 and 15 columns, a result similar to a grid-convergence criterion.

It is probably advantageous to average several columns and reduce the background noise, but at the same time if too many columns are averaged then the spatial

resolution will become too limited. For example, the image in Figure 6.8 contains 114 pixels per inch, so the averaging of 15 columns is equivalent to averaging over a length of 0.13 inches. This limitation will become especially important in regions where the flow characteristics change significantly over a short distance, such as across the first compression corner shown in Figure 6.8 where the instability waves first start to become visible. The effect of the averaging on the computed q'_{RMS} was examined, and the results are summarized in Figure 6.10.

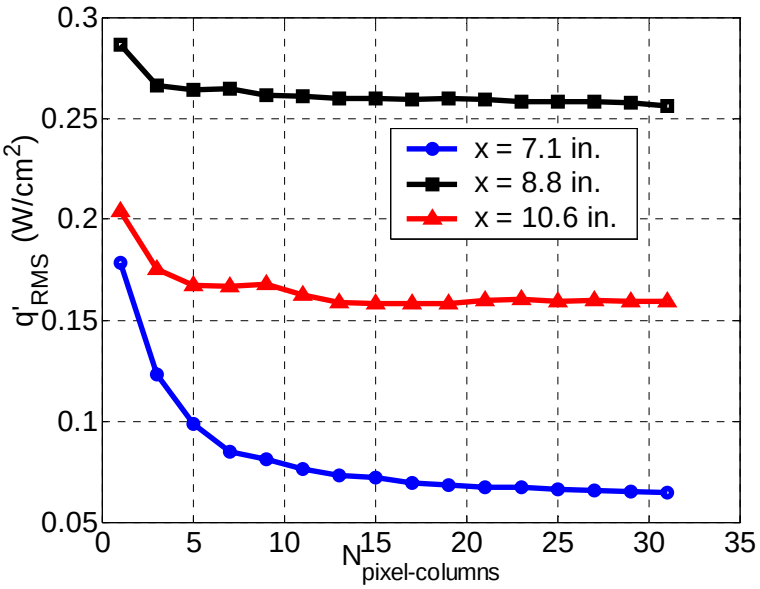

Figure 6.10. Variation of q'_{RMS} for different number of columns averaged (N) to obtain the spanwise heat transfer rate distribution.

This study used the same three streamwise locations used in Figure 6.9. The effect of the averaging is greatest on the first compression ramp, where the signal-to-noise ratio is small. The benefit of using extra columns diminishes quickly, and it was judged that 15 columns would be a reasonable value. This technique is applied to the image in Figure 6.8, and the q'_{RMS} distribution along the centerline is shown in Figure 6.11. The fluctuations are nearly constant on the first ramp, and increase quickly on the second ramp. The decrease around 8.5 inches might be the onset of turbulent flow, although this cannot be concluded from the available data.

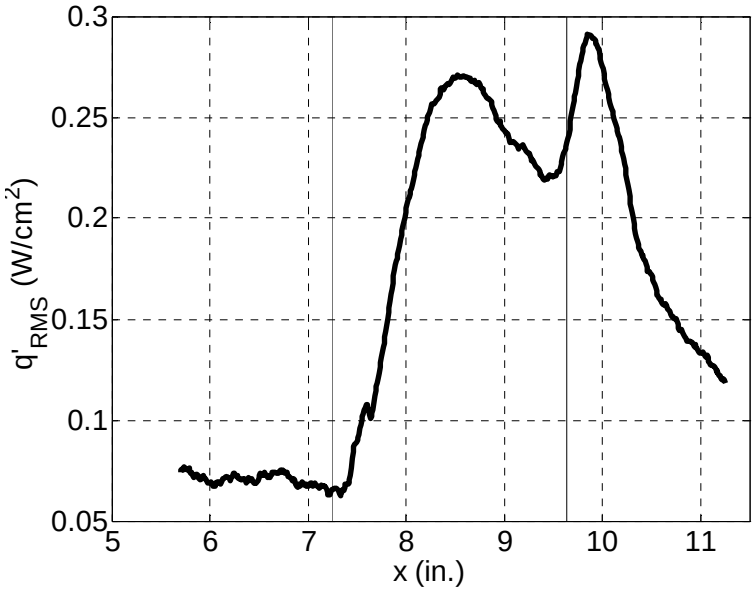

Figure 6.11. Variation of the q'_{RMS} along the centerline, with an averaging of 15 pixel columns.

6.5. Spectral Analysis Technique

The second approach for the instability analysis is to use a spectral approach. The dominant wavenumber can be determined in addition to the power density distribution. For this research Welch's method of averaged modified periodograms in Mathworks Inc.'s Matlab software is used. Five adjacent columns are averaged to obtain the spanwise heating distribution, before extracting the fluctuating component. The spectral analysis routine is then applied using a Hanning window with 256 points, 255 of which are overlap points. These settings result in each FFT window being shifted one pixel at a time. This extremely large number of FFT windows was necessary to reduce noise in the power spectra because of the limited number of fluctuation cycles in each image. The power spectral densities at three streamwise stations are shown in Figure 6.12 using these settings. These locations are the same stations used for the study of the RMS technique. A peak is clearly seen around 5.8 cycles/in. on the second compression ramp. The heat transfer rate image in Figure 6.8 shows about 12.5 streaks spaced over about 2.5 in., resulting in a wave-number of about 5 cycle/in.

The precision and resolution of the resolvable wave-number is limited by the pixel resolution available. For this particular data set, only 330 pixels are available. The streamwise vortices spread outwards due to cross-flow. This will result in a shift in the dominant wave-number, which might be the reason why the peak on the third compression ramp occurs at a lower wave-number, as shown in Figure 6.12. However, close examination of the spreading rate seen in Figure 6.8 shows that the variation of the dominant wave-number along the streamwise coordinate is only about 0.3 cycles/in. This variation was too small to quantify with the available image resolution and the resulting wavenumber resolution attainable with this spectral analysis routine. The wavenumber variation along the streamwise coordinate might be measurable using a spectral technique with more sophisticated algorithms, but this was not attempted here. Instead, the wavenumber variation was examined in a manual fashion when necessary, by drawing a line through the streaks and examining the spacing between them with a ruler.

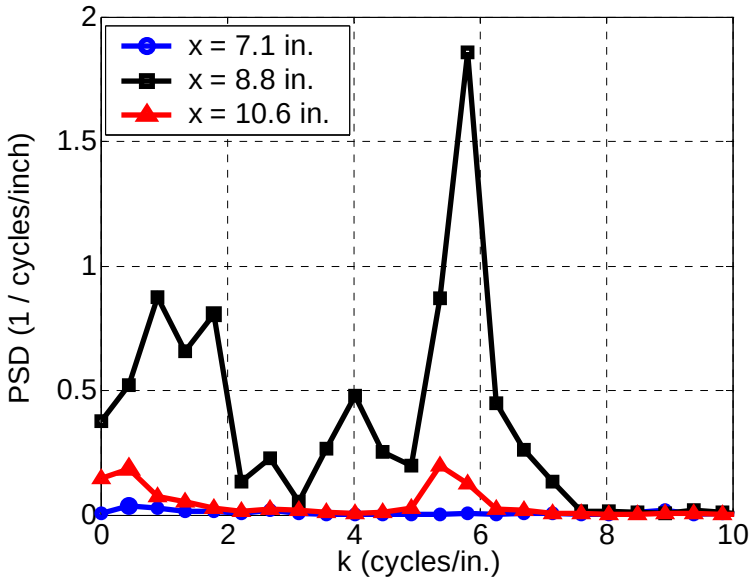

Figure 6.12. Power spectral density of the spanwise heat transfer rate fluctuations.

The study addressing effects of averaging columns of data was repeated for the spectral technique. The variations in the power density for several numbers of averaged columns are shown in Figure 6.13. Four wave numbers are shown, which defines the main peak near 5.8 cycles/in., seen in Figure 6.12. On the first ramp where the instabilities have not grown to sufficient amplitude, the power density converges rapidly

when seven or more columns are used. On the second ramp, convergence is established with about 13 columns. However, the power density for 5.81 cycles/in. still shows slight variations. Similarly on the third compression ramp, the power density for 5.36 and 5.81 cycles/in. never seems to converge. To reduce spatial uncertainty, 31 columns are chosen to be averaged for the spectral analysis shown here. This is equivalent to averaging data over a streamwise length of 0.27 in.

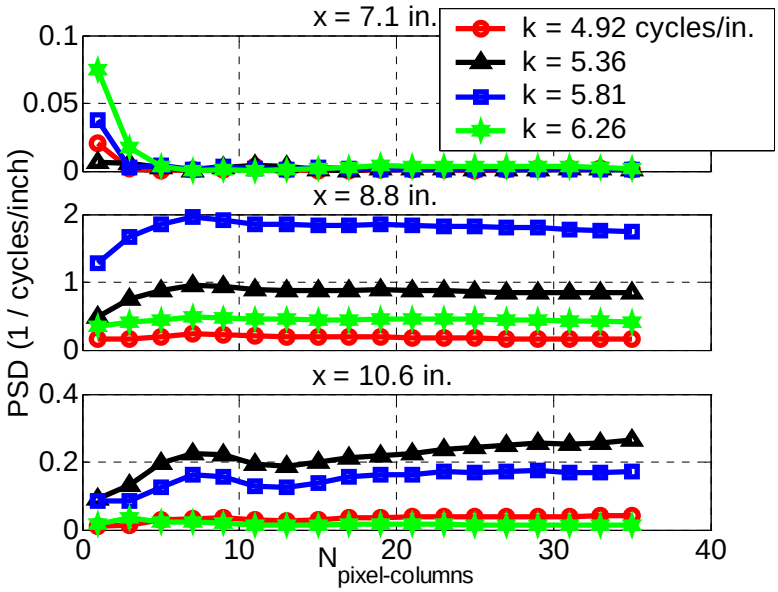

Figure 6.13. Power density magnitude variation for different number of columns averaged.

This technique is applied to the image shown in Figure 6.8, and the power density variation along the centerline is shown in Figure 6.14. The four wave numbers near the main peak seen in Figure 6.12 are shown. The variation of the power is also shown as part of this analysis. The power was computed by integrating the power spectral density from 4.92 to 6.26 cycles/in. The qualitative nature of the streamwise distributions of the 5.81 cycles/in. wave and the power is very similar to the results of the RMS approach shown in Figure 6.11. The value is nearly zero on the first compression ramp, and increases on the second ramp. The streamwise location of the second peak is around 9.9 in., which agrees with the RMS results as well. This agreement provides some level of confidence and validity in the application of this spectral analysis approach.

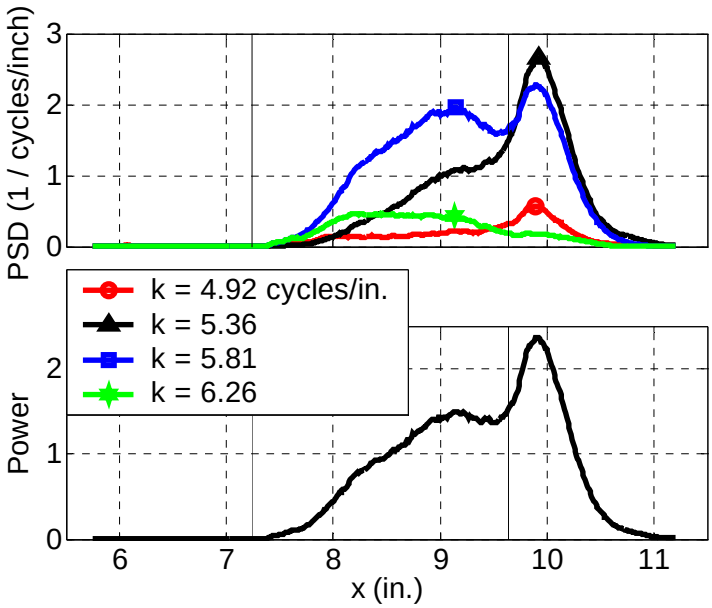

Figure 6.14. Power spectral density and power distribution along the centerline.

7. STREAMWISE VORTEX GENERATOR DEVELOPMENT

7.1. Effect of Paint Layer Roughness

The purpose of any roughness or perturbers used in studying boundary layer instability is so that the instability waves can be generated in a controlled manner, where the location and growth can be quantified. Any experiments will contain background disturbances, which must be reduced as much as possible, so that they do not contaminate the controlled disturbances. For this research where streamwise vortices are the primary interest, the roughness of the paint layer must be reduced through polishing. Wall roughness is known to have an effect on cross-flow and Görtler instability, which are the possible instability modes of relevance here. The effect of the wall roughness condition on the striation patterns will be briefly addressed, although the mean roughness height is not known. The comparisons were done only for qualitative purposes, and all images shown here are left as the uncalibrated intensity ratios. All cases presented here were performed at total pressure and temperature of 125.5±0.7 psia and 160±1 deg. C respectively, resulting in a unit Reynolds number of 2.49 million/ft ± 1.2 %.

The insulator layer is usually quite rough and has several high spots in the finish. Figure 7.1 shows the temperature distribution and a raw wind-off image obtained from such a painting. The striation patterns are clearly visible developing on the second ramp, although no artificial roughness placed was anywhere on the model surface. The wind-off image is quite smooth, with no significant random variations caused by the rough insulator.

These striation marks do not appear as clearly in an image with a polished insulator, as shown in Figure 7.2. The color scale used for Figures 7.1 and 7.2 are identical. Although the striations are still faintly visible on the third ramp, polishing the insulator layer clearly has a large effect on the formation of the striations. The wind-off image looks almost identical in terms of the smoothness of the image. The insulator layer

is usually significantly rougher than the TSP layer due to the larger thickness, and because the insulator layer often contains clumped TiO_2 powder, which deposits onto the surface. When the TSP layer is painted over a polished insulator layer, the "orange-peel" finish creates a slight roughness.

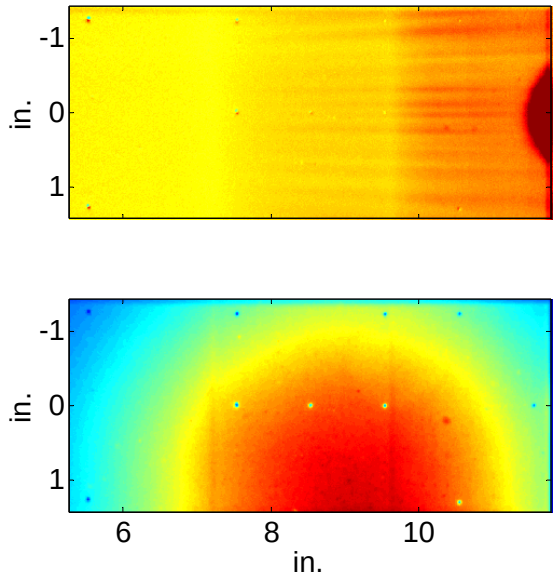

Figure 7.1. Uncalibrated temperature image and the wind-off image taken with an unpolished insulator layer.

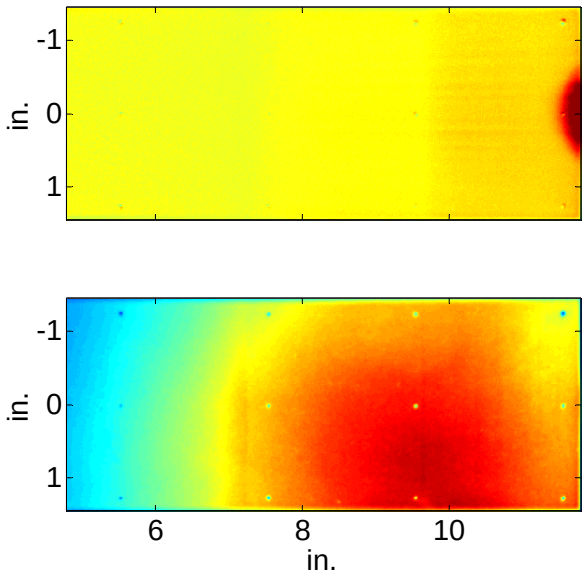

Figure 7.2. Uncalibrated temperature image and the wind-off image taken with a polished insulator layer.

This TSP layer was polished in addition to the insulator layer, and the results are shown in Figure 7.3. It might be arguable that the striation patterns are even weaker than that shown in Figure 7.2, but the benefit is probably not worth the loss of paint layer uniformity as shown by the wind-off image. Here, the thinner regions are clearly visible from the polishing. Achieving a uniform polishing of the TSP layer is almost impossible because the layer is only a mil or so to begin with. These three figures show that in order to minimize the naturally occuring streamwise vortices the insulator layer must be polished, but the TSP layer probably should be left untreated.

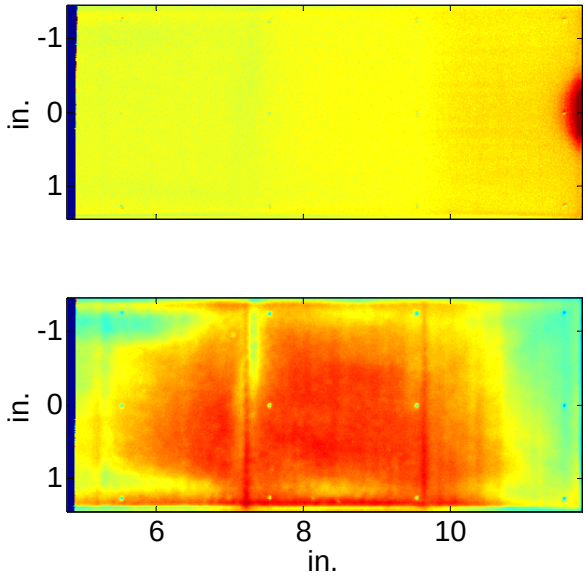

Figure 7.3. Uncalibrated temperature image and the wind-off image taken with a polished insulator and TSP layer.

7.2. Boundary Layer Trips

One technique to introduce streamwise vortices is to use discrete roughness elements on the windward surface, similar to boundary layer trips. This was done in previous experiments in the Mach-4 tunnel [35], and also in unpublished experiments in the Mach-6 facility on a blockage cone model. If the discrete roughness elements are too efficient at disturbing the boundary layer, they will act as ‘effective’ trips, where transition occurs almost immediately behind the trips. However, the size, height, and

streamwise location of the trips can be chosen so that they effectively act as perturbers, and not as trips. This technique was only briefly investigated, because most of the past experiments on compression corners seem to suggest that instability and transition due to streamwise vortices is most sensitive to the leading edge geometry. It seems like changing the leading edge geometry is the most effective means of disturbing the boundary layer, and the use of trips were investigated only for qualitative comparison, and to verify that changing the leading edge geometry is indeed the more effective of the two methods.

Two types of trips were investigated: plastic shim-stocks and round dry transfer lettering. For the shim-stocks, thicknesses of 0.01 and 0.06 in. were tried. Equilateral triangles with side lengths of about 0.1 in. were cut by hand using a razor blade. The round transfer lettering used had a diameter of about 0.1 in., which was the closest size available to the triangular trips. The triangular trips were glued directly onto the TSP surface at two locations. All trips had one of the vertices pointing upstream. The thicker trips of 0.06 in. were placed about 3.9 in. from the leading edge, which is similar to where the trips are located on the Hyper-X model [77]. Computations for the Hyper-2000 however are not available, and the discrete roughness Reynolds number for this case is not known, and consequently the effectiveness of the trips is not really known either. The thinner triangular trips of 0.01 in. were placed about 0.25 in. from the leading edge. For both locations, only four trips were used, spaced about 0.2-0.3 in. apart. For the transfer lettering roughness, multiple layers were stacked together to achieve thicknesses of 1 and 2 mils. These trips were also placed near the leading edge about 0.015 in. downstream, and were about 0.2 in. apart. All cases were performed with the initial total pressure and temperature at about 126±1.25 psia and 160±1 deg. C, which would result in a unit Reynolds number of about 2.4-2.5 million/ft. The exact freestream conditions for these runs are not available.

The uncalibrated temperature image using the triangular trips is shown in Figure 7.4. The relevant regions of the model for the two trip locations are marked, where the “Trip 1” are the thicker trips. The streak marks from these trips are visible which convect downstream. However it seems like the disturbances caused by the smaller “Trip 2” are

too small to measure with the available resolution of the CCD camera. Streak marks however can be seen developing on the second ramp, confirming the existence of some sort of streamwise disturbances. Unfortunately the striation patterns from both of these trips are not of sufficient quality or clarity to enable a quantitative measurement of the growth of the vortices.

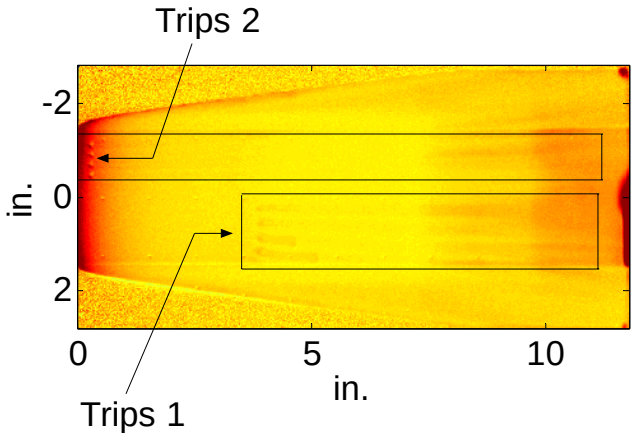

Figure 7.4. Uncalibrated temperature image using triangular trips about midway on the first ramp and near the leading edge.

This was the justification for attempting to use the much thinner transfer lettering near the leading edge, for which the results are shown in Figure 7.5.

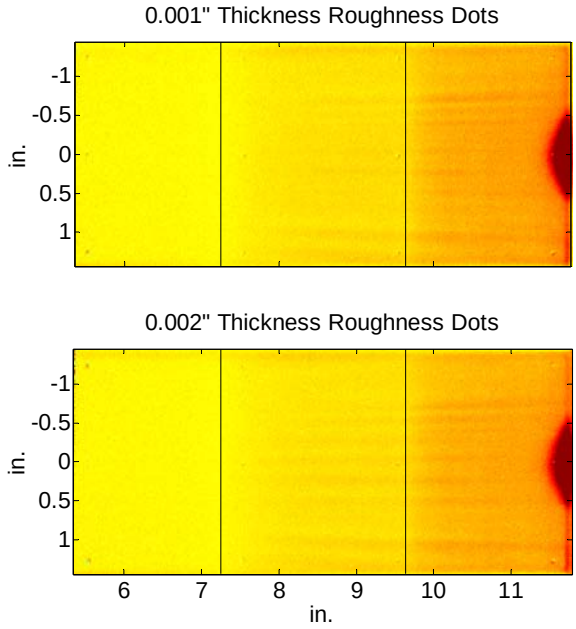

Figure 7.5. Uncalibrated temperature image using roughness dots placed about 0.015 in. from the leading edge.

For both thicknesses, the striation patterns are visible very faintly. However, the result shown in Figure 7.1 with the rough paint layer still shows the striations clearer. Also the two images in Figure 7.5 do not show any significant differences, ruling out the possibility of using this very thin roughness on the compression ramp to measure and quantify the parametric trend of the striation growth rates for different roughness heights. However, this might be measurable in the future if the sensitivity and resolution of the imaging system could be improved.

7.3. Tape Strips Wrapped Around the Leading Edge

To change the geometry of the leading edge, strips of various thickness, width, and height were cut from a few types of tape and wrapped around the leading edge. Two types of tape were initially tried, an aluminum metallic tape which is 0.004 in. thick, and standard scotch tape, which is 0.002 in. thick. Aluminum tape adhered very well to the model because not only does it have an adhesive surface, it yields to the leading edge geometry when wrapped around it. However, it was thought that it was too thick. Scotch tape was then used to decrease the thickness, but often times it peeled off from the surface during the wind tunnel runs, and consequently abandoned due to low reliability.

A schematic of the strips at the leading edge are shown in Figure 7.6. The relevant dimensions of the strips are the width, thickness, and spacing, and the lengths on the leeward and windward side, as labeled. It is expected that the spacing will have the dominant effect on the spacing of the streamwise vortices, or the wave number of the instability waves. The thickness along with the unit Reynolds number will most likely affect the amplitude and growth rate of the disturbances. However, the effects of the width and the two lengths were not as clear, and were briefly investigated. It was desirable to use as small as possible of a width, so that a large number of strips could be applied to the leading edge, if necessary. A small length on the leeward side was also desired from a vehicle development standpoint, so that the flow on the leeward side would not be disturbed unnecessarily.

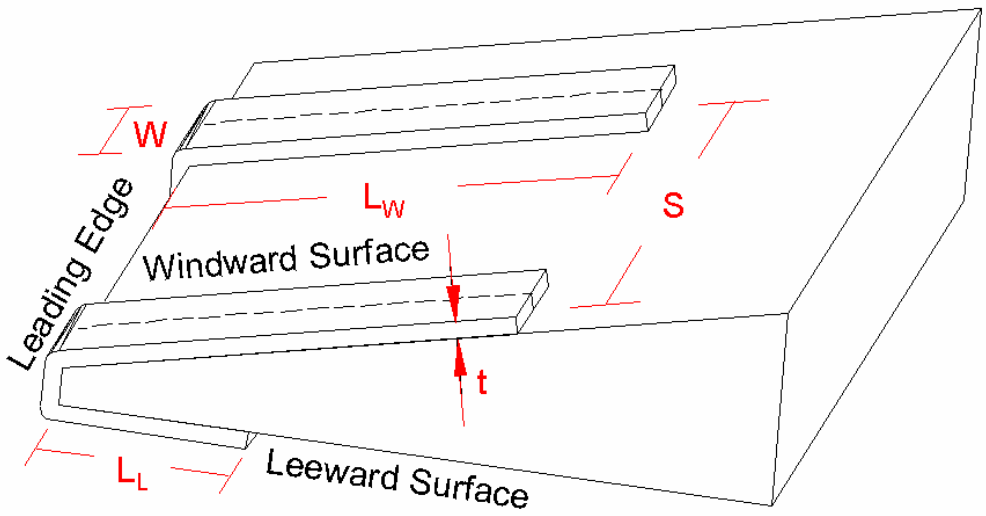

Figure 7.6. Schematic of the leading edge roughness strips.

A series of experiments were performed using the aluminum tapes, to investigate the effects of the width and length of the roughness strips. The effects of the spacing and thickness are investigated as part of the final data set obtained for this research, and will not be discussed here. The experiments were done only for qualitative comparisons, and all images presented are left as uncalibrated temperature images. All cases presented used five strips of aluminum tape at the leading edge. Two layers of tape were used, resulting in a roughness strip thickness of 0.008 in. The length of the roughness strip on the leeward side was about an inch for all cases. The total pressure, temperature and unit Reynolds number for all cases were 106±5.3 psia, 398±6.5 deg. K and 2.56±0.07 million/ft. respectively. Every result for these studies had a hot-spot near the trailing edge of the model. This high heating region was caused by the model sting used earlier, which protruded slightly above the third compression ramp and created a stagnation region.

7.4. Effect of Leading Edge Roughness Strip Width

Three values for the width of the roughness strips were tried, 0.03, 0.1, and 0.2 in. During the preliminary phase of this research, a width of 0.1 in. was used as a standard, and showed promising results [32]. This width was adapted as the baseline here, and the

width was increased and decreased by a factor of two. However, the dry transfer lettering strip was a candidate material to use in place of the aluminum tapes because of its much smaller thickness. The smallest width available for these was 0.03 in., so this value was used as the lower bound for this study.

The uncalibrated temperature images for the three roughness strip widths are shown in Figure 7.7. Although five roughness strips are used, only three of the corresponding striations stay on the compression ramps. The vortices from the outer two roughness strips get swept off onto the chine due to cross-flow.

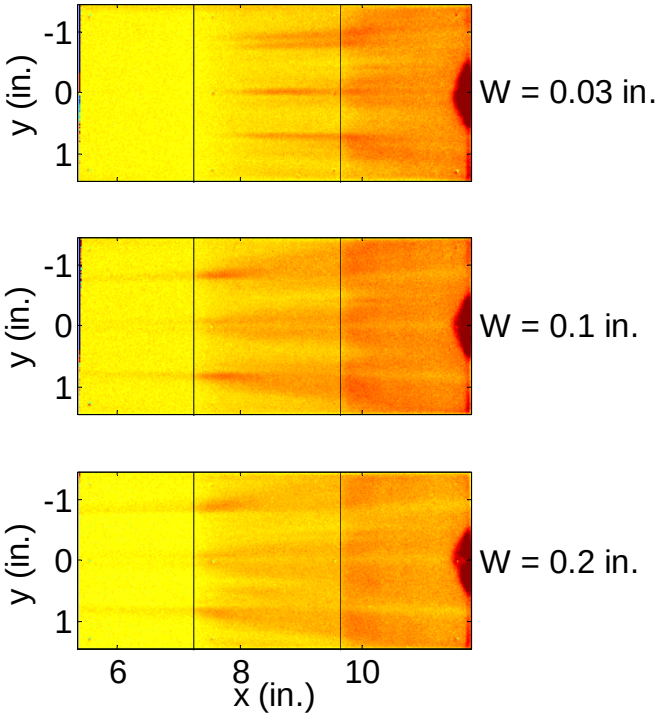

Figure 7.7. Uncalibrated temperature images for various roughness strip widths.

The spreading of the vortices is significantly reduced for a width of 0.03 in. The widths of 0.1 and 0.2 in. seem to result in a more or less identical spreading of the vortices with regions of laminar flow in between, which is implied by the lower temperature. This suggest the onset of turbulent flow in the higher heating wedges seen on the second compression ramp, but hot-wire measurements will need to be taken to confirm this hypothesis. The width of the roughness strips seems to influence the amplitude of the vortices on the region of the model shown, but does not seem to influence the width,

location, or spreading rate due to cross-flow. The breakdown of the vortices on the second compression surface prohibits a spectral analysis of the instability waves on this part of the model for the larger width roughness strips. However, the vortices are clearly visible on the first compression surface. For a width of 0.03 in., the vortices are not visible on the first compression ramp. Most of the past research done on compression corner flows seems to focus on the corner itself or downstream of the corner, and it is probably reasonable to do so for this research as well. For this reason, a width of 0.03 in. was adapted as a standard dimension for future experiments.

7.5. Effect of Leading Edge Roughness Strip Length

As with the roughness strip width, a standard length of 0.5 in. was used in previous experiments, and was also used as the baseline length here [32]. However, if a roughness strip of this size was scaled to flight conditions, it would be an enormously large trip device, and is probably unrealistic. Also, the amplitude of the vortices decreases with a decreasing roughness strip width, but even with the smallest width of 0.03 in. in Figure 7.7, it is not clear if the disturbances on the second compression surface are strong enough to be measurable, yet weak enough that they do not break down. It was hoped that this vortex breakdown could be reduced even further by decreasing the length of the roughness strips on the windward side.

This study used a roughness strip width of 0.1 in, and not the standard width of 0.03 in. as determined above. Lengths of 0.5, 0.1, and 1/64-1/32 in. were tried, and the resulting uncalibrated temperature images are shown in Figure 7.8. For the smallest length, it was too difficult to maintain a consistent length for all roughness strips. The data for the 0.5 in. length is the same data shown in Figure 7.7 for the 0.1 in. width case. The effect of the roughness strip length is identical to the effect of the width. As the length is decreased, the amplitude and spreading of the vortices seems to become reduced, and this seems like the only effect. Again, the smallest length of 1/64-1/32 in. was adapted as a standard length on the windward side for the roughness strips.

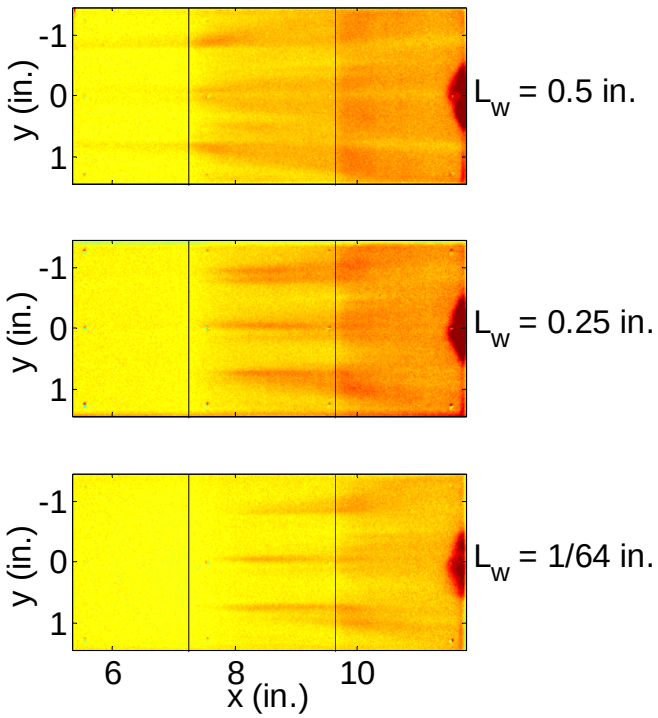

Figure 7.8. Uncalibrated temperature images for various roughness strip lengths on the windward side.

Another important issue with the roughness strips is the fact that they are wrapped around the leading edge. As stated earlier, this is not desirable from a vehicle development point of view. The roughness strip extending around the leading edge onto the leeward surface would create unnecessary disturbances on the leeward surface as well. A sample test run was performed to investigate the effect of not wrapping the roughness strips around the leading edge. The roughness strips were applied onto the leading edge on the windward surface as with the other cases presented, but were cut off so that they would not extend around the leading edge. The standard dimensions for the length and width of 0.5 and 0.1 in. were used for this study.

This roughness strip configuration is compared to the original case with the strips wrapped around the leading edge in Figure 7.9. The case with the strips wrapped around the leading edge is the same data set shown in Figure 7.7 for a width of 0.1 in. At a glance the two images look identical. The break down of the vortices on the second compression surface appears to be of identical magnitude. However, the vortices on the

first compression ramp are slightly visible for the original case, but are not visible with the roughness strips unwrapped from the leading edge. This shows that wrapping the roughness strips around the leading edge increases the amplitude of the vortices just enough so that they are measurable, but does not seem to change the qualitative breakdown process on the second surface. All else equal, it would be advantageous to measure the vortices on the first compression surface as well, so it was decided that the roughness strips should be wrapped around the leading edge.

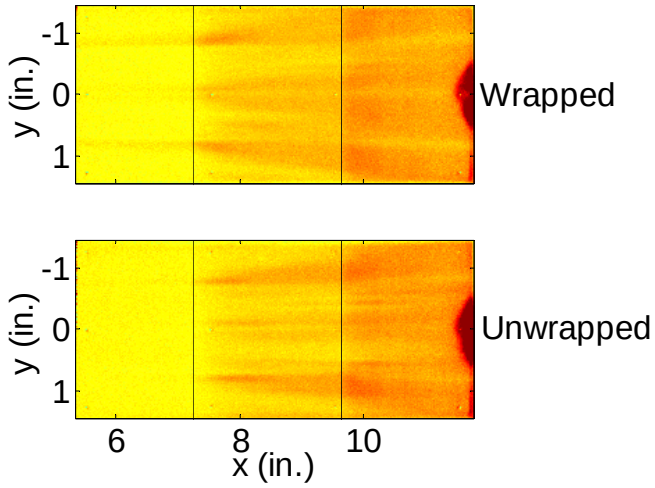

Figure 7.9. Uncalibrated temperature images with the roughness strips wrapped and unwrapped around the leading edge.

As a side note, these results combined with the results shown in Figure 7.8 raise an important issue regarding the receptivity process of these streamwise vortices. In Figure 7.8, when the length of the roughness strips was reduced from 0.5 to 0.25 in., the vortices became too weak to measure on the first surface. In Figure 7.9, if the roughness strips are unwrapped from the leading edge, the vortices on the first compression surface also become too weak to measure, even with a roughness strip length that was shown to generate vortices which were measurable on the first compression surface.

Most boundary layer trip devices work by generating streamwise vortices from the trailing edge or from the wake behind the trip, and it would be logical to expect that these roughness strips are generating streamwise vortices in a similar manner. However, if that were the case, then the critical roughness strip dimension that determines the amplitude of the vortices would be the thickness at the trailing edge relative to the local

boundary layer thickness. This value is determined by the length of the roughness strips, for a set roughness strip thickness. But because the results in Figure 7.8 and 7.9 show that the amplitude of the vortices changes either by wrapping or not wrapping the roughness strips from the leading edge, it seems like the streamwise vortices are being generated not only at the trailing edge, but elsewhere as well. Two possibilities are from the modified shock wave geometry due to the presence of the roughness strips, or an effect from the modified shock layer. Unfortunately this question cannot be answered with the data presently available. More experiments specifically targeting this issue will be required, along with computations of the receptivity process.

The final study performed addressed the effect of the length of the roughness strip on the leeward side. This dimension probably does not affect the amplitude or the growth rate of the vortices on the windward side, but this assumption was checked since it was simple to do. The length of the roughness strip on the leeward side was decreased from about an inch to about 0.1 in. The results are shown in Figure 7.10. The width of the roughness strips was 0.03 in., and the length on the windward surface was about 1/64 in.

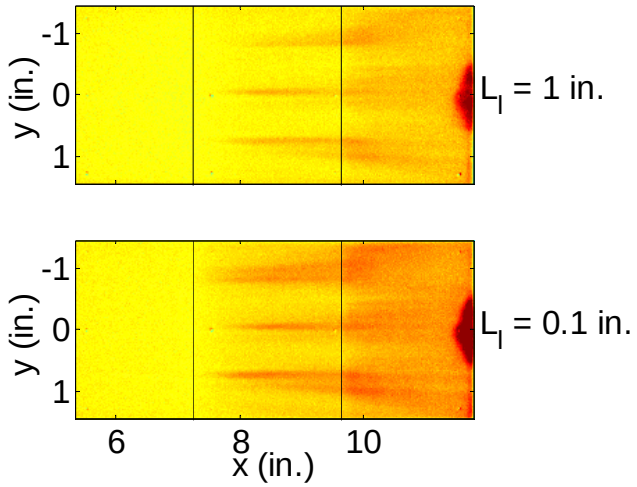

Figure 7.10. Uncalibrated temperature images for two roughness strip lengths on the leeward side.

The baseline case with a leeward side roughness strip length of an inch is the same data shown in Figure 7.8 for the smallest length on the windward surface. The two images are identical, except that the overall temperature is higher for the shorter leeward surface length case. This is most likely because the total pressure was about 10 psia lower for

this case. Although the data are not as thorough as desired it was concluded that the length of the roughness strips on the leeward surface has no influence on the amplitude and growth rate of the vortices on the windward surface.

7.6. Final Roughness Strip Configuration

The results and conclusions from the above experiments determined the standard values of some of the roughness strip dimensions. In summary, the length on the windward surface was set to 1/64-1/32 in, the width was set to 0.03 in., the roughness strips should be wrapped around the leading edge, and the length on the leeward surface can be anything. The dry transfer lettering was chosen to replace the aluminum tapes because it is much thinner, only 0.00025 in. thick. The particular dry transfer lettering used was strips of the same width specified above, and with a total length of only about 1/8 in. Consequently these would not extend too far downstream on the leeward surface. A close view of the leading edge with these roughness strips applied is shown in Figure 7.11.

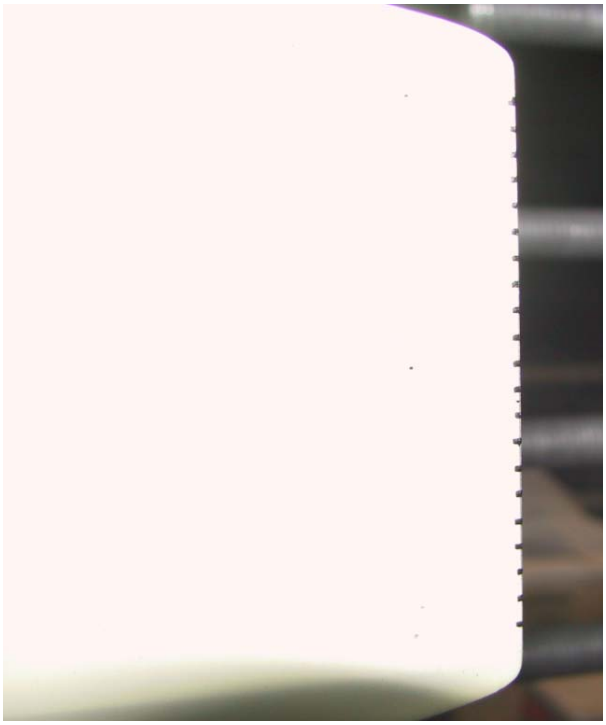

Figure 7.11. Image of the leading edge roughness strips.

8. RESULTS AND DISCUSSION

8.1. Oil-Flow Experiment Results

Oil-flow experiments were performed only with the no-leading-edge-roughness condition, at initial total pressures of 65, 77.5, 90, 102.5, and 115 psig. The initial total temperature for all runs was 160 deg. C. These flow conditions corresponds to initial unit Reynolds numbers of 1.67, 1.93, 2.20, 2.46, and 2.72 million/ft. Images taken at the lowest, medium, and highest unit Reynolds numbers are shown in Figures 8.1-8.3. These images have been processed using the image registration technique, and the color scale has been converted to grayscale in order to enhance the contrast.

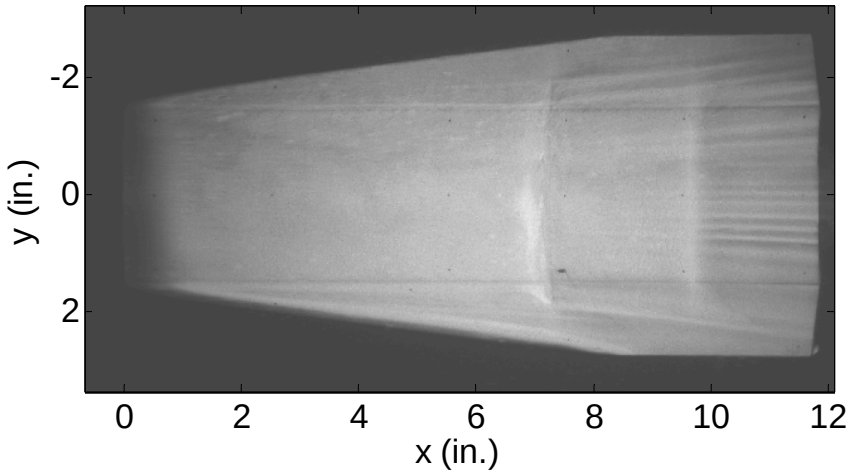

Figure 8.1. Oil-flow image at an initial unit Reynolds number of 1.67 million/ft.

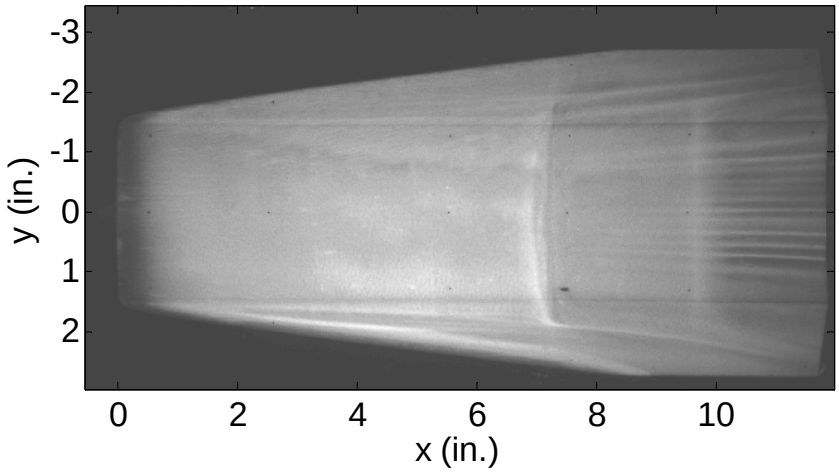

Figure 8.2. Oil-flow image at an initial unit Reynolds number of 2.20 million/ft.

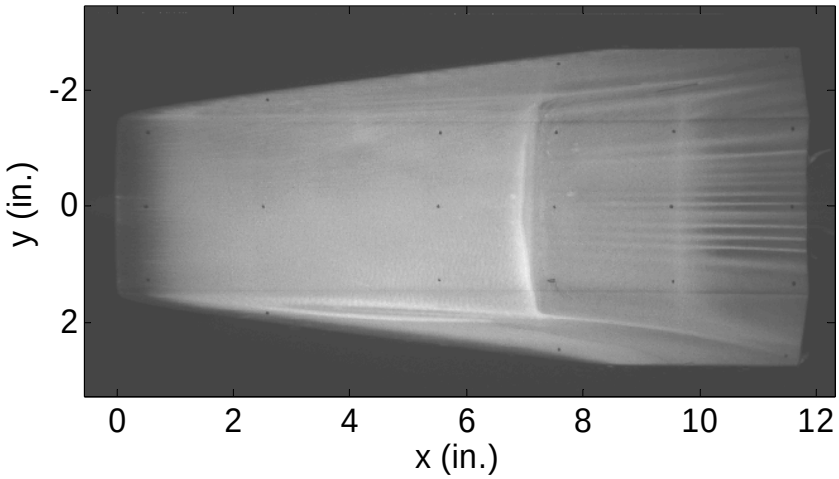

Figure 8.3. Oil-flow image at an initial unit Reynolds number of 2.72 million/ft.

The separation line immediately upstream of the first compression corner in each image is evident from the bright line, which is caused by the accumulation of the oil at the separation line. The separation onset becomes clearer with increasing Reynolds number because the oil motion increases. The separation line seems to be symmetric about the centerline for the most part. The separation line is brighter on the lower part of the model because of the tendency of the oil to flow downwards in the time it takes to prepare for tunnel run after painting the oil onto the model. Another flow feature which is evident is the presence of streamwise vortices on the second and third compression surfaces. The vortices first become visible around 8 inches from the leading edge, which

is 0.75 inches downstream of the first compression corner, but are not present on the first compression ramp. This suggests that the initial disturbances, which are probably introduced by the freestream noise and/or the leading edge, are being significantly amplified by the separation zone, which is known to be highly unstable. This implies that the characteristics of the separation point and the extent has a first order impact on the instability of streamwise vortices for these geometries.

The separation lines from these oil-flow images were extracted in a manual fashion, and are shown in Figure 8.4 at several initial unit Reynolds numbers. A second order polynomial is fitted to each set of data. The location of the first compression corner is also shown for reference.

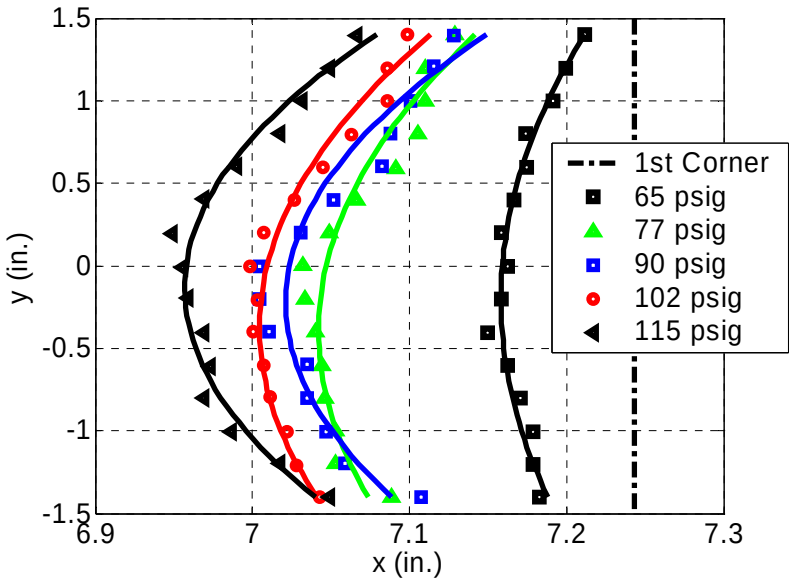

Figure 8.4. Effect of initial total pressure on the separation line.

A slight asymmetry is present in each data set, which is probably caused by the combined effects of an asymmetric leading edge, a slight yaw in the model orientation, a non-uniform oil layer, the spatial uncertainty in the image-processing of about 0.05-0.07 in., and error in extracting the data points from the images. This also makes it difficult to assess whether the crossing of the separation lines for the 77 and 90 psig cases at the edges are real effects. However, the general trend of the separation line moving upstream with increasing Reynolds number seems to be consistent. This is characteristic of laminar separation bubbles near compression corners at high-speed conditions, where the

upstream influence of the adverse pressure gradient caused by the corner increases with Reynolds number. If the experiments could be performed at much higher Reynolds numbers, the separation line can be expected to start moving back downstream when flow above the separation zone becomes transitional.

The images shown in Figures 8.1-8.3 do not show the reattachment point clearly. Reattachment is another flow feature which can be expected to influence boundary layer instability. The reattachment line can be better seen with the images taken with the sprit technique, shown in Figures 8.5 and 8.6 for the lowest and highest unit Reynolds numbers. The separation zone is evident by the region at about 7 inches from the leading edge where the oil sprits have not been washed away significantly. The quality of the images makes it difficult to quantify the reattachment point, but it is clear that the separation zone is larger for the higher unit Reynolds number case. This implies that for the range of freestream conditions performed as part of these experiments, the reattachment point moves downstream with increasing unit Reynolds number, and that the extent of the separation zone increases with unit Reynolds number.

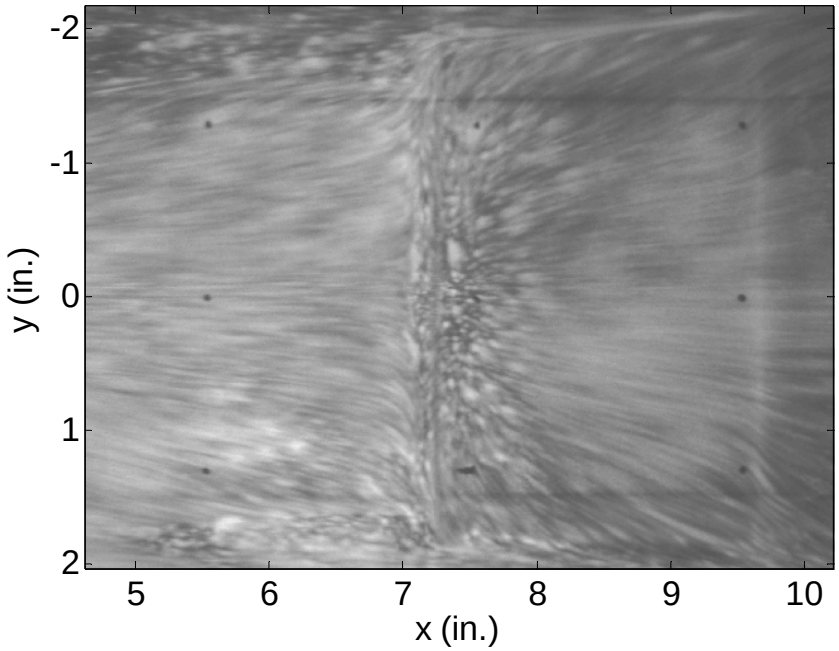

Figure 8.5. Oil-flow image near the first compression corner using the oil-sprit technique at a unit Reynolds number of 1.67 million/ft

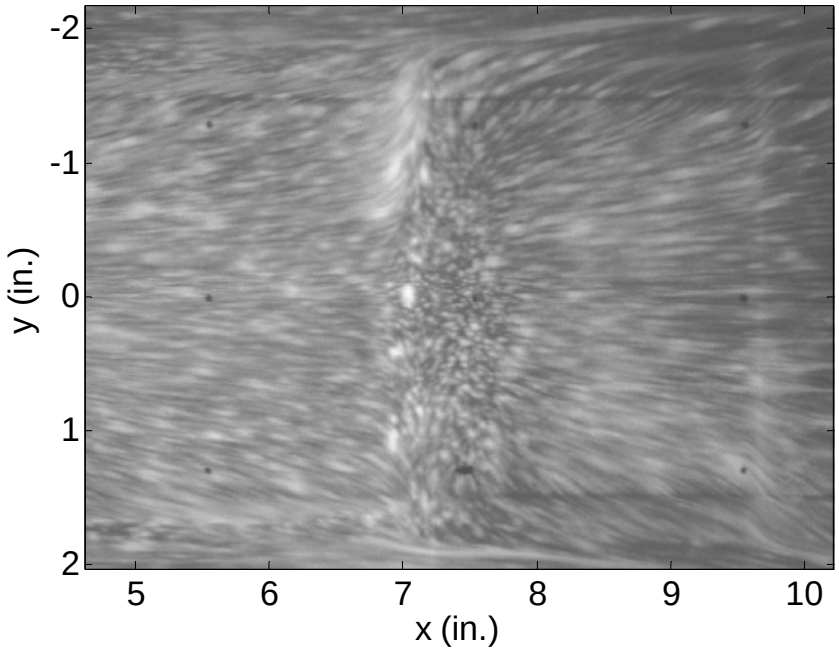

Figure 8.6. Oil-flow image near the first compression corner using the oil-sprit technique at a unit Reynolds number of 2.72 million/ft

The instability of the streamwise vortices will thus increase with unit Reynolds number, not only because of its direct effect but also because of the increased effect from the larger separation zone.

The streamwise vortices seen on the compression ramps are the naturally occurring disturbances, because of their existence without any controlled disturbance generators. They also represent the most unstable wavenumber, which is either amplified the most or selectively generated by the receptivity process from the combination of the freestream noise, leading edge imperfections, and the separation zone. The spanwise fluctuations seen in the image in Figure 8.3 are extracted and shown in Figure 8.7 for several unit Reynolds numbers. Here, approximately 200 pixel columns were averaged to reduce the background noise level, which corresponds to a streamwise distance of 1.5 inches starting from a streamwise location of about 10 inches. The vortices seem to be located in the same location from run to run, showing that the occurrence of these disturbances is repeatable, and that their wavenumber is not affected by the unit Reynolds number.

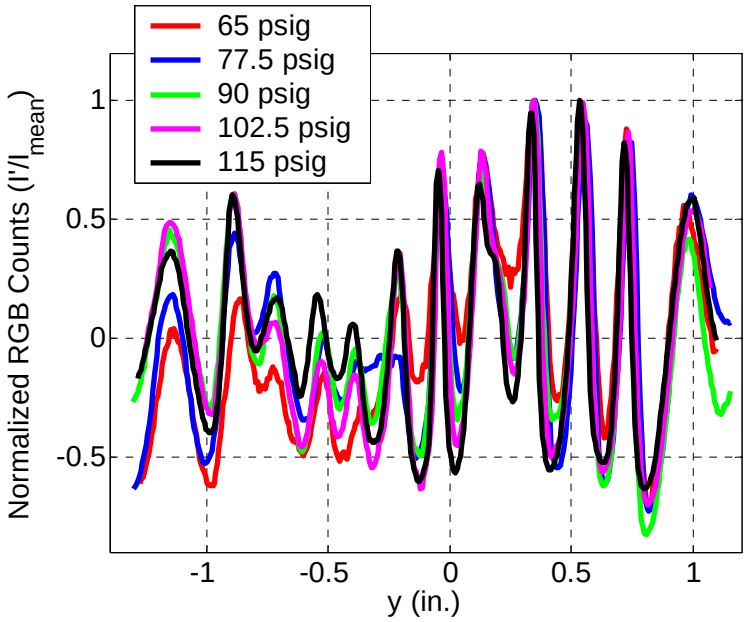

Figure 8.7. Streamwise-averaged spanwise fluctuations seen in the oil-flow images.

Approximately 12 cycles are present in this data, which results in an average wavenumber of 5.3 cycles/inch. The power spectral density of these fluctuations also shows a peak around 5-5.5 cycles/inch, which is shown in Figure 8.8. This wavenumber corresponds to an average vortex spacing of 0.19 inches.

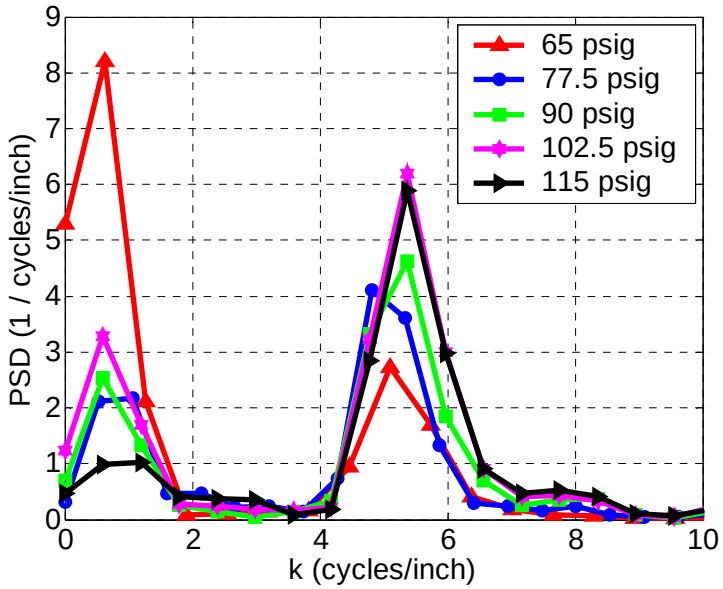

Figure 8.8. Power spectral density of the spanwise fluctuations seen on the third compression ramp in the oil-flow images.

This wavenumber probably represents the most unstable wavenumber, which will be confirmed in the quantitative experiments using TSP. Another important conclusion that can be drawn from this analysis is that the when leading edge roughness strips are applied, a spacing of 0.19 inches should show the largest amplification of the resulting streamwise vortices because it would enhance the flow structures in the leading edge region.

8.2. Temperature-Sensitive-Paint Heat-Transfer-Rate Images

TSP experiments were performed using various thicknesses and spacings of the leading edge roughness strips, for a range of total pressures. The roughness spacings tried were 0.21, 0.18, 0.16, 0.14, and 0.125 inches. These spacings correspond to applying 13, 15, 17, 19, and 21 strips equally spaced, with the two outer strips placed 1.25 inches from the centerline. Three thicknesses of 1.25, 1.75, and 2.25 mils were tried, which corresponds to stacking 5, 7, and 9 layers of transfer-lettering strips. For each combination of the spacing and thickness, tunnel runs were performed at initial total pressures of 79.5, 92.0, 104.5, 117.0, and 129.5 psia. These total pressures results in unit Reynolds numbers of approximately 1.67, 1.93, 2.20, 2.46, and 2.72 million/ft with a total temperature of 160 deg. C.

The qualitative trends seen in the resulting heat-transfer-rate images will be shown. The complete dataset consists of a total of 75 images. However, only representative cases will be shown to illustrate the qualitative parametric trends. The effect of total pressure is shown in Figure 8.9. Here, the lowest, medium, and highest total pressure cases are shown for the cases where 17 strips of 2.25 mil thickness were applied. The streamwise vortices are clearly visible, and the location and the vortex axes seem to be independent of the total pressure. The overall mean heating level increases with total pressure, which is an expected result.

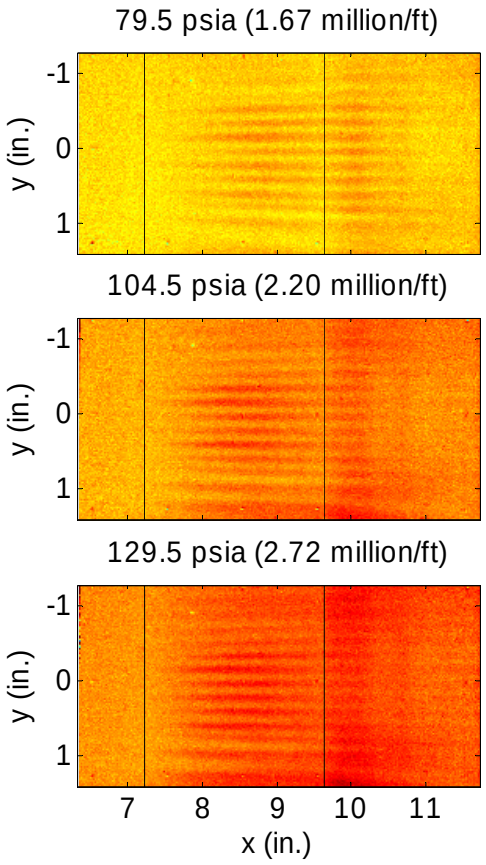

Figure 8.9. Effect of initial total pressure on the heat-transfer-rate images. The cases shown used 17 strips (0.16 inch spacing) with three layers (2.25 mils).

The effect of roughness spacing is illustrated in Figure 8.10. Here, the largest, medium, and smallest roughness spacing cases are shown. All three cases used a thickness of 2.25 mils, at the highest total pressure of 129.5 psia. The individual vortices are clearly visible for the 17 and 21 strip cases, but are not as clear for the 13 strip case. The 13 strip case seems to show a few streaks very clearly, with weaker vortices in between, whereas for the other two cases, there does not seem to be this significant of a difference between each vortex. However, the general trend of the increase in the number of vortices with increasing number of roughness is clearly illustrated. This trend shows that the streamwise vortices are the results of some sort of disturbances initially generated by the roughness at the leading edge.

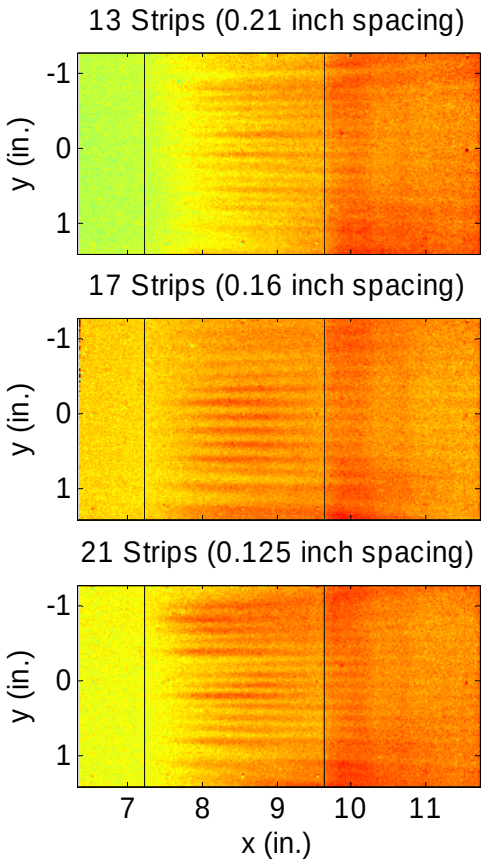

Figure 8.10. Effect of leading edge roughness spacing. The cases shown used three layers (2.25 mils) of roughness strips, all at a total pressure of 129.5 psia (2.72 million/ft).

Finally, the effect of the roughness thickness is shown in Figure 8.11. All three of these cases were performed with 17 strips at the highest pressure (129.5 psia). The overall heating rate seems to be mostly unaffected by the roughness thickness. The vortices in all three images seem to start growing at the same location. There is however a difference in the clarity of the streamwise vortices. The vortices in the image using a thickness of 1.25 mils are hardly visible. The thickness of the roughness probably affects the initial amplitude of the disturbances. A thicker roughness can be expected to generate stronger vortices, which show more clearly in these images because of the higher heating.

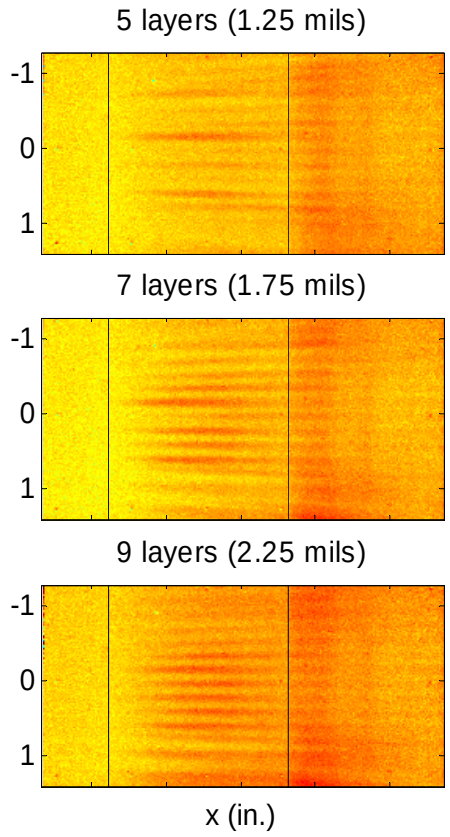

Figure 8.11. Effect of leading edge roughness thickness. The cases shown used 17 strips (0.16 inches spacing), all at a total pressure of 129.5 psia (2.72 million/ft).

8.3. Spanwise Heat-Transfer-Rate Fluctuations

The fluctuations seen in the heat-transfer-rate images are shown in more detail in this section. For each case of data presented, only the spanwise heat-transfer-rate distributions at selected representative stations are shown. These stations are 6.90, 8.97, and 10.09 inches from the leading edge, which corresponds to the first, second, and third compression ramps. Also, each set of data presented were smoothed by averaging 61 adjacent columns, centered at the stations mentioned above. This corresponds to averaging over a distance of 0.45 inches.

As a representative set of data, the spanwise heat-transfer-rate distributions for the case applied with 17 strips of 2.25 mils thickness at the highest total pressure is shown in

Figure 8.12. The fluctuations on the second ramp are clearly visible in this figure. The cross-flow washes away the vortices near the edges of the ramps, and the figure shows only 13 peaks. The magnitude of the fluctuations are smaller on the third compression ramp, but the mean heating value is slightly higher, which suggests that transition has occurred somewhere in between these two stations.

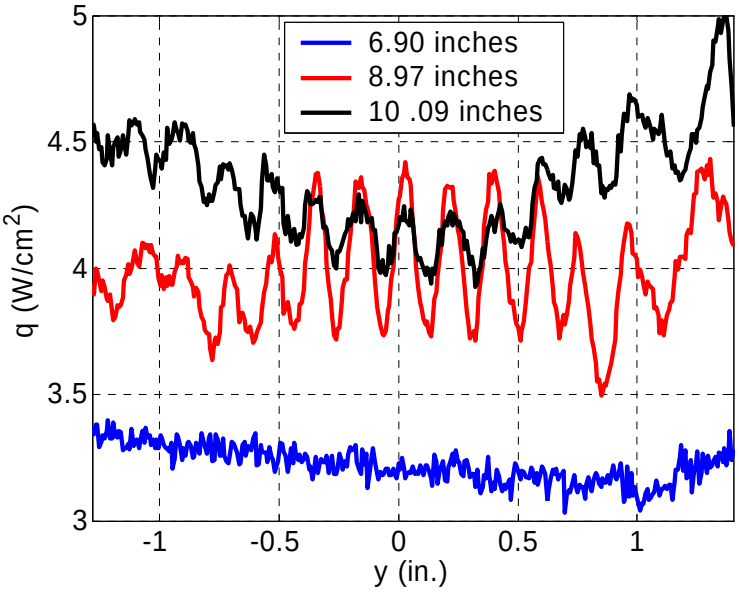

Figure 8.12. Comparison of the spanwise heat-transfer-rate distributions on the three compression ramps.

Near the centerline, the fluctuations (and hence the streamwise vortices) are still in the same spanwise locations, but some spanwise movement is seen for the outer vortices. The influence of cross-flow on the spanwise location of the vortices increases away from the centerline. The mean heating is much smaller on the first compression ramp, where the boundary-layer is probably laminar. Visually, there is no sign of the fluctuations at this station, although very small amplitude disturbances must be present which grow into the large fluctuations on the second compression ramp.

The effect of total pressure on the fluctuations is shown in Figure 8.13. For clarity, only the data on the second ramp is shown. Here, the case employing 17 strips of 2.25 mils thickness are shown at the lowest, medium, and highest total pressures. The fluctuations seem to stay in the same spanwise location regardless of the total pressure. This result is consistent with the oil-flow results, where the location and spacing of the

naturally occurring vortices were the same for all total pressures tried. Also, the magnitude of the fluctuations seems to be more or less the same at all three total pressures, and the total pressure affects only the mean heating value.

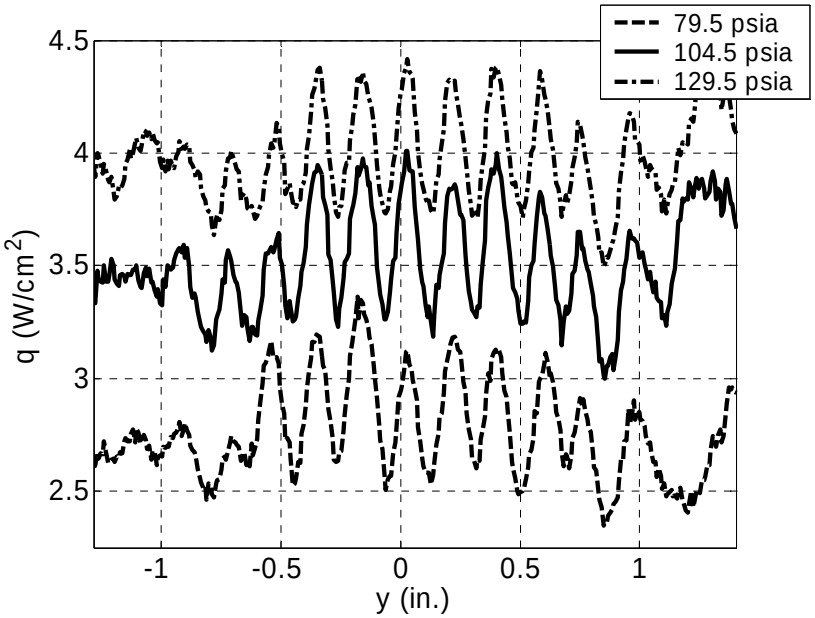

Figure 8.13. Comparison of the spanwise heat-transfer-rate distribution on the 2nd compression ramp against the initial total pressure.

The effect of roughness spacing is shown next in Figure 8.14. Here, the cases with 13, 17, and 21 strips of 2.25 mils thickness roughness are shown, at the highest total pressure of 129.5 psia. The wavelength of the fluctuations is clearly affected by the roughness spacing, seen by the increasing number of cycles with decreasing roughness spacing. The mean heating value for the 17 and 21 roughness cases are more or less the same, but the mean heating value for the 13 roughness is considerably smaller. It is possible that the roughness spacing somehow affects the meaning heating value, such as by generating vortices which are more efficient at promoting transition and raising the meaning heating value. However, the initial model temperatures for these three cases were 34, 31, and 30 deg. C. respectively. The higher model temperature for the 13 roughness case explains the lower mean heating value. This issue will be examined further in the next section.

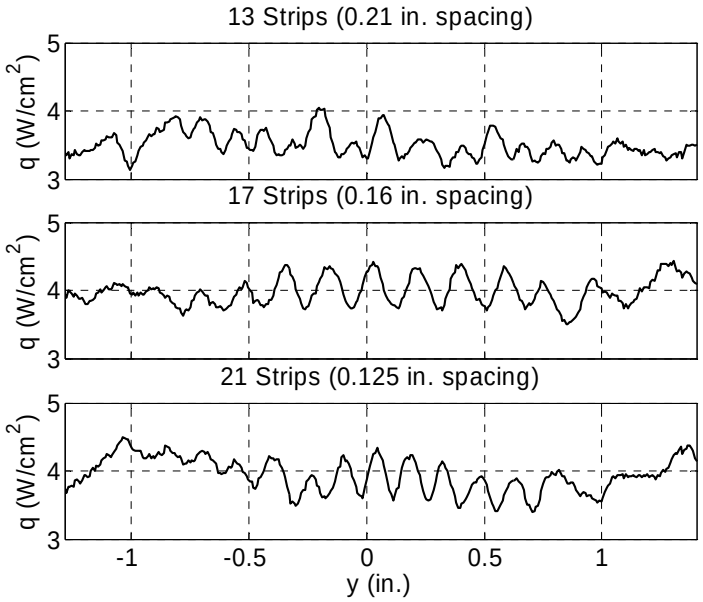

Figure 8.14. Comparison of the spanwise heat-transfer-rate distribution on the 2nd compression ramp against the roughness spacing.

The effects of roughness thickness on the heating distribution are shown in Figure 8.15. Here, the case using 17 strips at the highest total pressure is shown. The fluctuations seem to occur at the same spanwise location regardless of the roughness thickness.

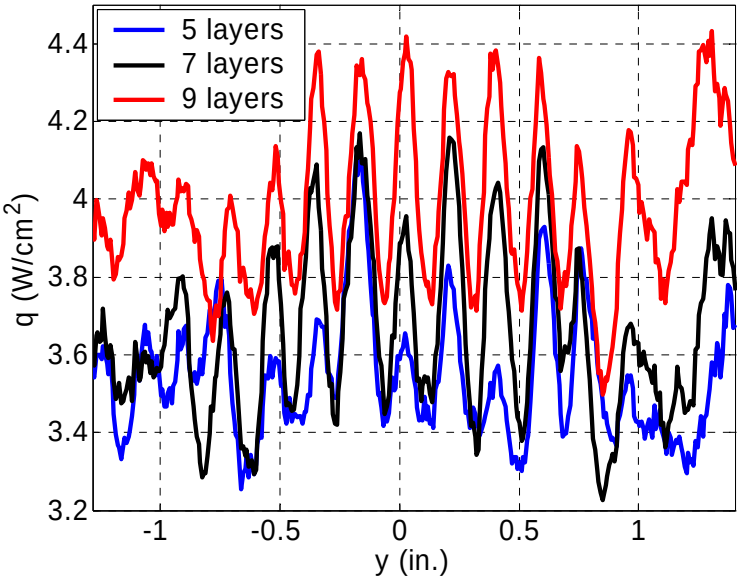

Figure 8.15. Comparison of the spanwise heat-transfer-rate distribution on the 2nd compression ramp against the roughness thickness.

However for the smallest thickness case near the centerline, every other vortex seems to be much weaker. The cause of this is not known, but analysis of the other cases not shown here also shows this trend. The roughness thickness also seems to affect both the mean heating value and the magnitude of the fluctuations. This is an expected result, since the roughness thickness influences the magnitude of the initial disturbances generated. This would result in larger disturbances downstream causing larger fluctuations, and also will generally tend to increase the overall heating rate and promote transition more.

The magnitudes of the fluctuations seen in the spanwise heat-transfer-rate distributions are quantified in terms of the fluctuating component of the heating distribution normalized by the mean heating value. This process should help to factor out some of the offsets seen in the heat-transfer-rate distributions in the previous section, assuming that they are the result of slightly different conditions, such as the model temperature. The fluctuations shown in Figure 8.14 are normalized and re-presented in Figure 8.16.

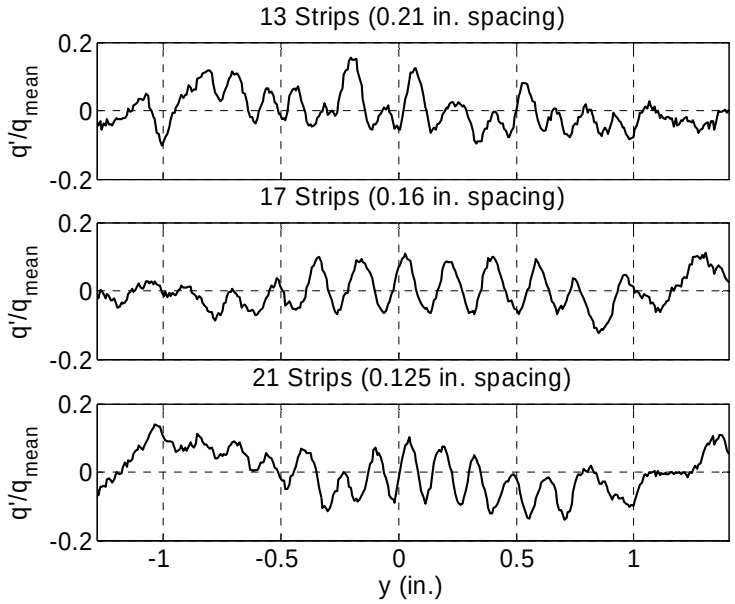

Figure 8.16. Comparison of the normalized fluctuating component of the spanwise heat-transfer-rate distribution on the 2nd compression ramp against the roughness spacing.

The significant offset seen in Figure 8.14 is not as apparent in this figure. Also, the fluctuations seem to be of the same order of magnitude, of about 10 % of the mean value.

However, it must be stressed that this normalization scheme is strictly valid only if the error in the mean heating value is more or less the same as the error in the fluctuating component of the heating.

Assuming that this assumption holds, the magnitudes of the fluctuations are quantified for all 75 cases available, and are presented in Figure 8.17.

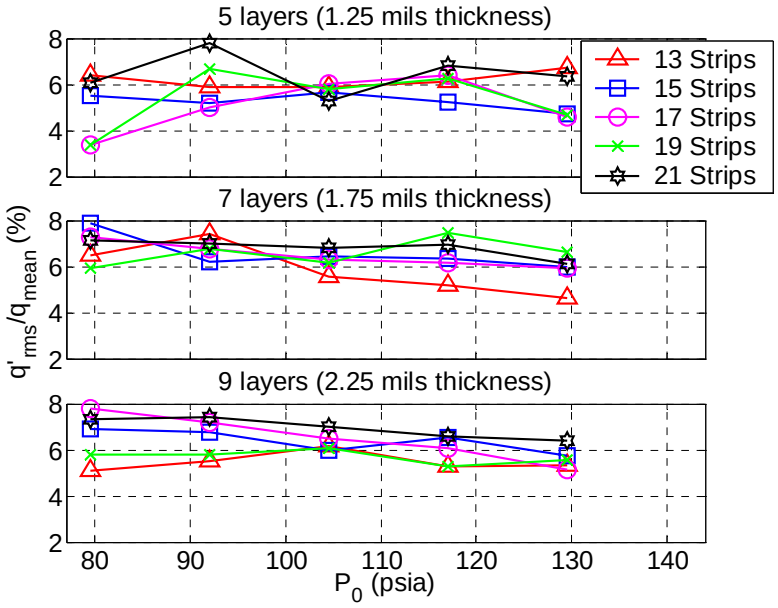

Figure 8.17. Comparison of the magnitudes of the fluctuations normalized by the mean heating value on the 2nd compression ramp.

Here, the RMS of the fluctuations is computed for each case available and then normalized by the mean heating value. On average, the fluctuations are about 6±2 % of the mean heating value. However, these values are only representative of the fluctuations specifically at the streamwise station of 8.97 inches. The figure does not show any clear trends with total pressure, roughness spacing, and roughness thickness, as would be expected. This might be evidence that all three of the parameters which are investigated in this research (unit Reynolds number, roughness spacing and thickness) affect the mean heating value and possibly the magnitude of the initial disturbance, the instability growth rate and amplification ratio, but does not have an effect on the normalized fluctuations. Another possibility is that for all conditions investigated the disturbances become saturated at this point and cannot grow any further, which would result in disturbances of

the same amplitude. These hypotheses will be investigated in the coming sections by investigating the growth of these instabilities.

8.4. Spacing and Spreading Rate of the Streamwise Vortices

In addition to the magnitude of the fluctuations seen in the spanwise heat-transfer-rate distributions, the spacing and spreading of the fluctuations is an important aspect of these instability mechanisms. This information will surely be important for computational model development, especially because it is not clear whether these vortices are influenced only by the Görtler mode, only the cross-flow mode, or both. The spacing of each fluctuation cycle can be extracted from the dataset in two ways. The number of cycles over a determined spanwise distance can be visually counted from the spanwise heating distributions. A more sophisticated method would be to use spectral methods to determine the frequency, or wavenumber content. Such a computation is shown in Figure 8.18. Here, the cases employing the thickest roughness at the highest pressure, for each roughness spacing cases, are shown. The peak wavenumber increases with increasing number of roughnesses as expected.

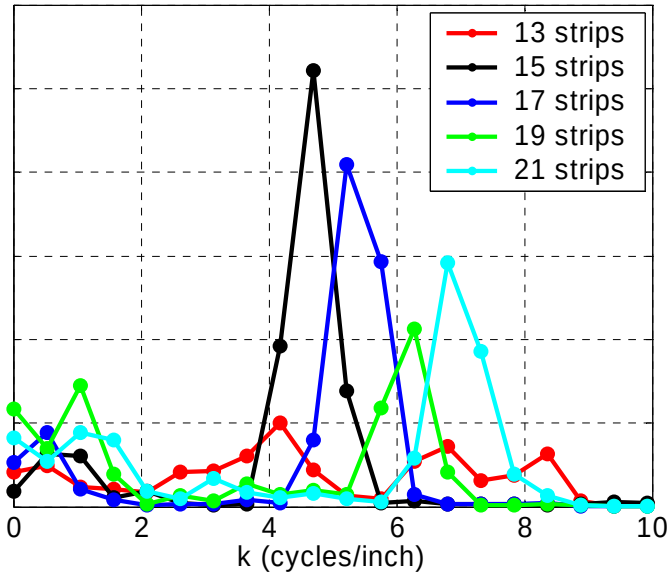

Figure 8.18. Power spectral density of the fluctuating component of the spanwise heat-transfer-rate distributions.

The peak for the 13 roughness case is not as clearly separated from the other wavenumbers due to the lower clarity of the streaks in the images. However, a peak seems to be present at about 4.2 cycles/inch.

The average spacing of the fluctuations, or the inverse of the wavenumbers, is plotted against the spacing of the roughness in Figure 8.19. As a reference, the fluctuation spacing determined from visual inspection is shown as well. This reference data for the largest spacing using 13 strips has been omitted because of the low quality image and the difficulty in visually counting the fluctuations. However, for the remaining cases the values agree very well, validating the spectral method. The error bars shown represent the attainable resolution in the spectral analysis, which is limited by the CCD camera pixel resolution and/or the span of the compression ramp. The uncertainty here is computed using the wavenumber values adjacent to the dominant wavenumbers from the spectral analysis. The streamwise vortices slightly spread spanwise from the leading edge, evident by the slightly higher disturbance spacing value, for each roughness spacing cases.

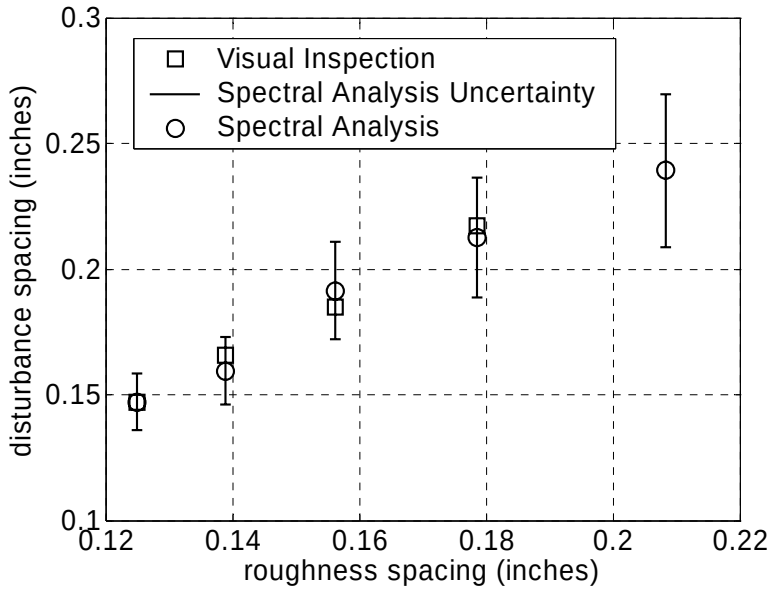

Figure 8.19. Spacing of the streamwise vortices against the roughness spacing.

This spreading is illustrated in Figure 8.20. Here, the case with 17 roughness strips of 2.25 mil thickness 2.72 million/ft unit Reynolds number is shown. Lines are traced from the locations of the roughness strips to the streaks seen in the heat-transfer image.

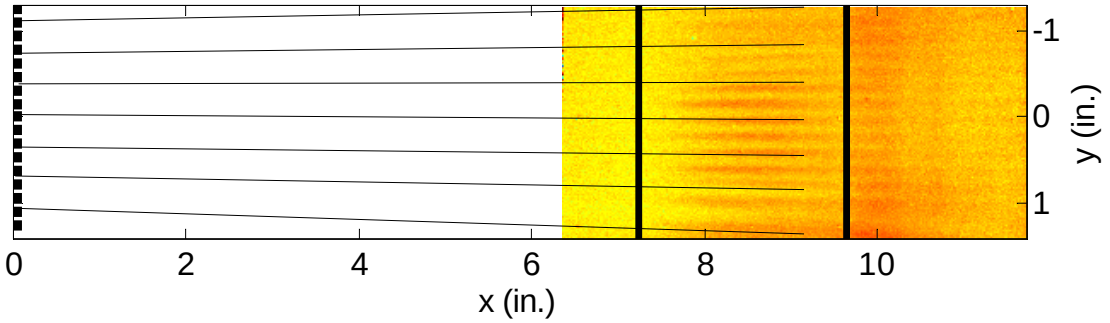

Figure 8.20. Spanwise spreading of the streamwise vortices on the compression ramps from the roughnesses.

Figure 8.20 shows that the spreading is more significant away from the centerline. Neglecting this variation in the spreading rate along the span, the spreading rate of the streamwise vortices is shown in Figure 8.21. This spreading of the streamwise vortices is an average spreading value. Here, the spreading rate is defined as the difference between the roughness spacing and average disturbance spacing over the streamwise distance between them.

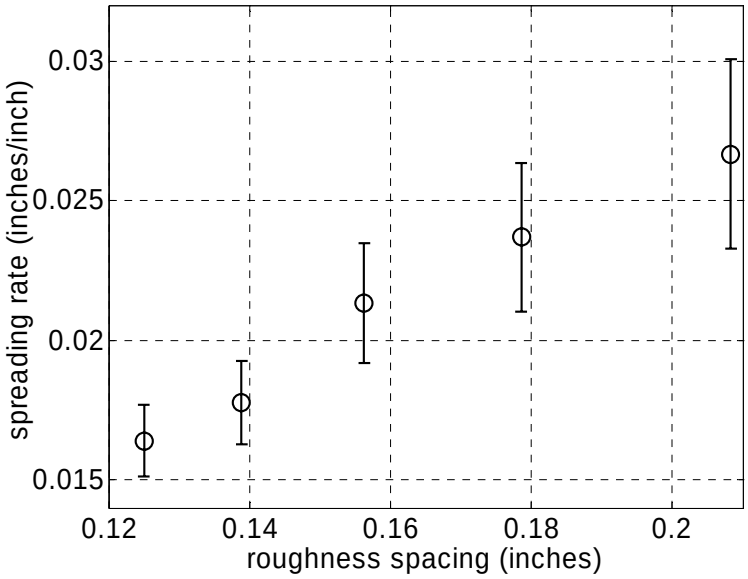

Figure 8.21. Spreading rate of the streamwise vortices against the roughness spacing.

Only the data computed from the spectral analysis is shown here, along with the uncertainty value propagated. The uncertainty is quite large, but in general the spreading rate increases with increased roughness spacing. This shows that this type of spatial instability waves characterized by streamwise vortices is nonlinear, in the sense that the spreading rate changes with the dominant wave number.

This variation seen in the spreading rate might be evidence that the cross-flow instability mechanism is playing a role for these types of instabilities and transition mechanisms. In general the Görtler mode is the result of wall curvature and the resulting pressure gradient that acts on the flow. It is difficult to imagine that it can have an effect on the spreading rate, which would seem to be influenced by the spanwise pressure gradient and the resulting cross-flow. The role of the separation bubble is not clear either, but it probably has an effect by coupling with the Görtler mode and/or the freestream noise, or possibly the shear-layer above the bubble is a separate instability mechanism. No attempt is made in this research to answer some of these questions, but surely these questions are important and must be addressed in future research in order to develop an understanding of the physics governing these types of flowfields.

8.5. RMS Heat-Transfer-Rate Fluctuation Growth

The variation of the heat-transfer-rate fluctuations along the streamwise direction is quantified in terms of the fluctuating component normalized by the mean heating rate. A representative set of data is shown in Figure 8.22. The data shown here is for the case employing 15 roughness strips (0.18 inch spacing). The data is grouped according to the three roughness thicknesses tried, and the data for each initial total pressure are shown. The fluctuations clearly grow mostly on the second compression ramp immediately downstream of the first corner. The fluctuations grow to some maximum value and then decay, but for many cases a slight increase is seen immediately past the second corner as well. The decay in the fluctuations on the second ramp is one sign that suggests transition has occurred, but it can be misleading to use this as a generalized criterion for transition onset.

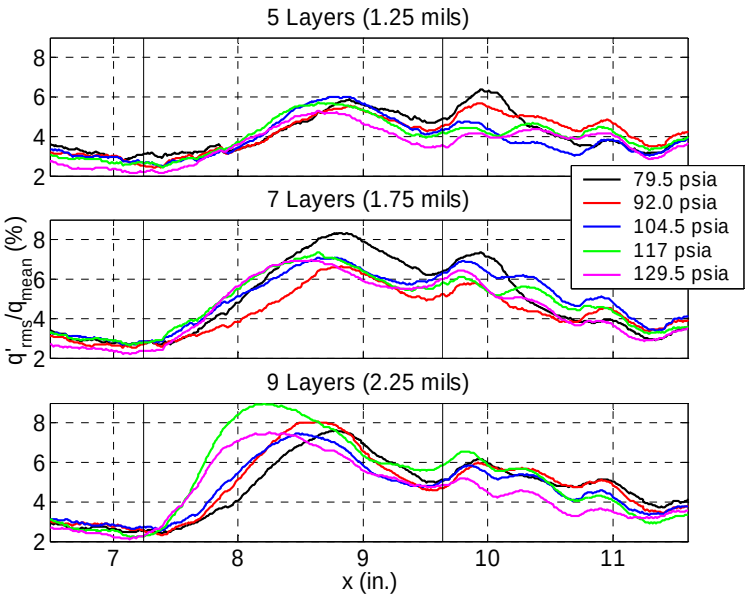

Figure 8.22. Streamwise growth of the RMS heat-transfer-rate fluctuations. All cases shown are for the cases with 15 roughness strips (0.18 inch spacing).

It is possible that at the lower pressures, transition actually takes place on the third compression ramp rather than on the second ramp. Some other measurements such as hot-wire data, and/or more accurate and reliable mean heating data are required to quantify the transition onset.

However, this dataset does not seem to show any clear trends in the fluctuation growth. Overall, increasing the roughness thickness seems to increase the fluctuations, which is an expected result. However, when each case of data is compared more carefully, and the effect of total pressure is considered simultaneously, the trends are not clear. The variation with total pressure for the smallest roughness thickness case is not as clear as the other two thickness cases. For the 1.75 mil thickness case, the highest total pressure seems to peak the earliest, but the magnitude of the peak is actually the highest for the lowest total pressure. Similarly, the peaks in the 2.25 mil thickness case shows a general increasing trend and an earlier growth with total pressure, but when all the details are considered the trend is not as clear.

This might be influenced by the fact that the fluctuation growth is illustrated in these plots using the raw normalized fluctuation values. One possibility is to convert the dataset into some sort of amplitude ratio, such as by normalizing the normalized

fluctuations by the initial disturbance magnitudes. This is shown in Figure 8.23. The initial disturbance amplitudes used here are the averaged fluctuation values over the first compression ramp. It is arguable that systematic trends for some of the cases are evident, especially for the case with the 1.25 mil thickness roughnesses. The amplitude ratio seems to grow earlier and to a higher value as the total pressure increases. However, this trend is not consistently seen for the other two roughness thickness cases. One problem is that this technique has a severe drawback that the initial disturbance magnitude is very difficult to quantify. The roughness geometry and locations are controlled and known, the disturbances introduced by them are probably repeatable, but the receptivity process and the quantitative effects immediately downstream of the roughness are not known. The RMS fluctuation values upstream of the first corner are mostly noise. Therefore there would be no physical basis or consistency from case to case for such comparison.

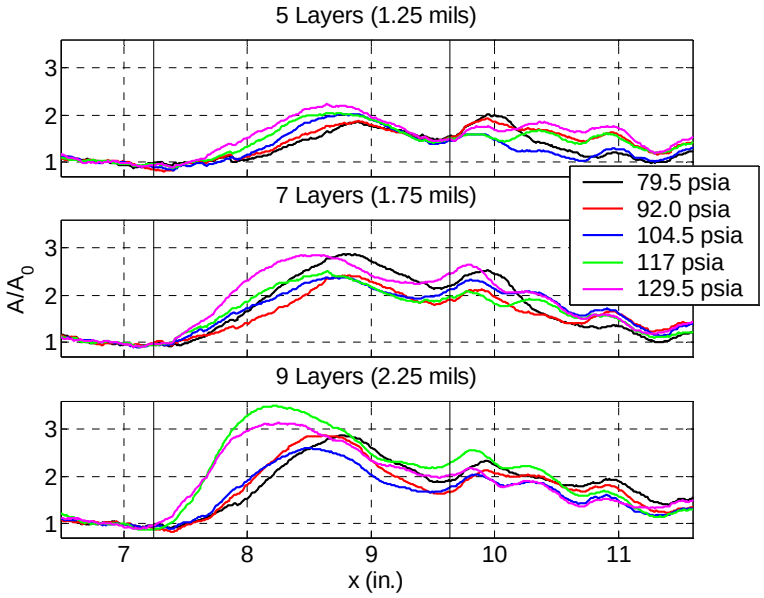

Figure 8.23. Streamwise growth of the RMS heat-transfer-rate fluctuation amplitude ratios. All cases shown are for the cases with 15 roughness strips (0.18 inch spacing).

The maximum value of the disturbances was used instead of the initial value as the point of normalization. The application of this to the data shown in Figure 8.22 is illustrated in Figure 8.24. The streamwise location of the normalization point is marked for each case. This figure shows much more clearly the general forward movement of the peak fluctuation, and the earlier growth as the total pressure is increased. For the 1.25

mil thickness case, the two lowest pressure cases show a peak on the third compression ramp, whereas the remaining three total pressures show a peak on the second ramp. This might be a sign that transition initially takes place on the third ramp, and moves forward to the second ramp as the Reynolds number is increased. The roughness thickness might be small enough here for transition to take place on the third ramp at the lower pressures, but at the higher roughness thicknesses, the initial disturbances are large enough that for this pressure range transition will always occur on the second ramp. Again, the data and the trends shown in these plots support these hypotheses, but do not prove or disprove it.

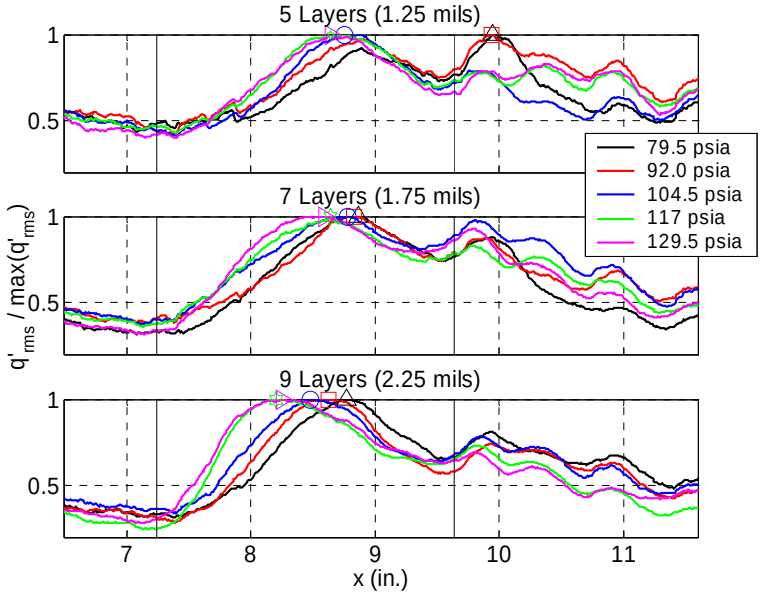

Figure 8.24. Streamwise growth of the RMS heat-transfer-rate fluctuations normalized by the value of the maximum fluctuation. All cases shown are for the cases with 15 roughness strips (0.18 inch spacing).

This normalization scheme seems to give reasonable results, so an investigation on the effect of the choice in the maximum fluctuation value is performed. Figure 8.25 shows the same dataset, but this time the normalization point is kept consistent to the maximum value on the second ramp. For this dataset, this only affects the data for the smallest roughness thickness case, and there is no significant difference between Figures 8.24 and 8.25. This process is repeated by consistently using the maximum value on the third ramp, and the results are shown in Figure 8.26. Here, streamwise location of the maximum values marked with the symbols probably has no significance, in terms of

transition onset, except for the two pressure cases for the smallest roughness thickness case discussed previously.

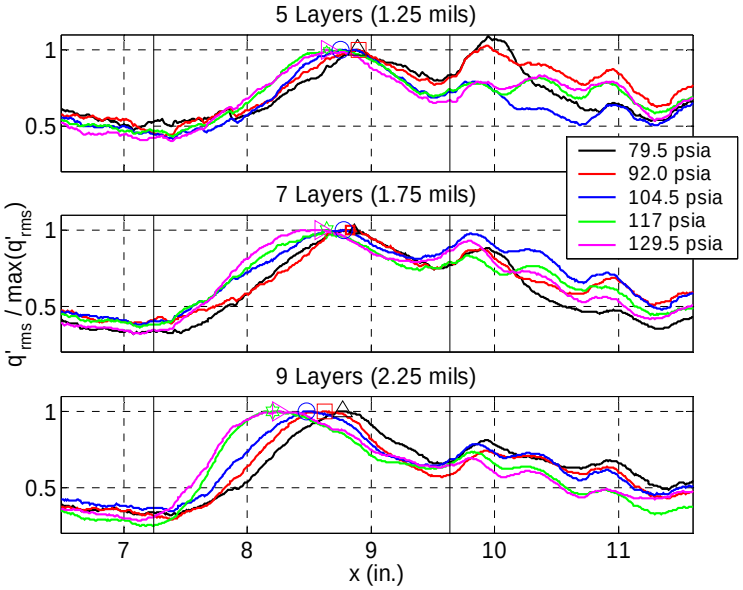

Figure 8.25. Streamwise growth of the RMS heat-transfer-rate fluctuations normalized by the value of the maximum fluctuation on the second compression ramp. All cases shown are for the cases with 15 roughness strips (0.18 inch spacing).

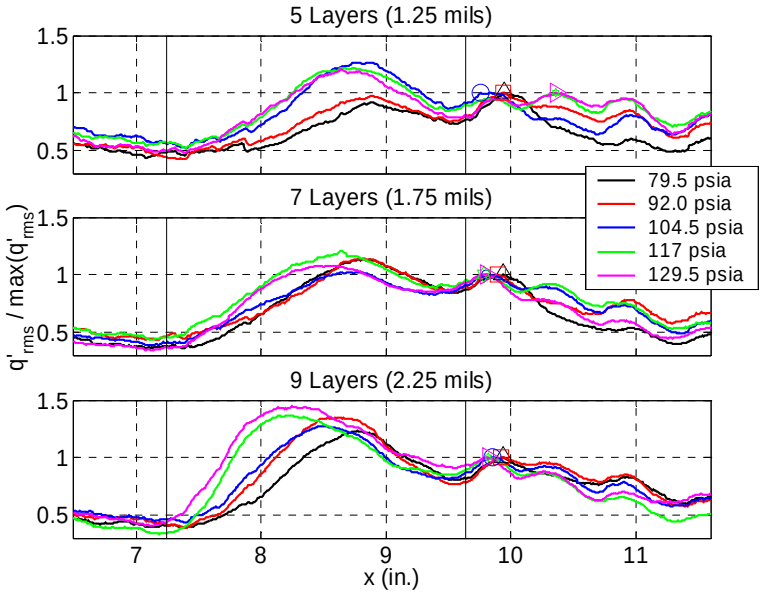

Figure 8.26. Streamwise growth of the RMS heat-transfer-rate fluctuations normalized by the value of the maximum fluctuation on the third compression ramp. All cases shown are for the cases with 15 roughness strips (0.18 inch spacing).

The variation of this streamwise location is very small compared to the previous two normalization schemes. The overall trends on the second ramp are not as clear here either. The magnitude and location of the peak on the second ramp does not show a good correlation with total pressure.

Each of these data processing schemes shows similarities and subtle differences, but it is difficult to conclude which one overall gives the best results. It is very possible that the root of the problem lies within the raw fluctuation data shown in Figure 8.22, and has nothing to do with how the normalized fluctuations are then normalized. One known problem with quantifying the fluctuations with an RMS is that it represents an integrated magnitude of the fluctuations, including noise. The leading edge flaws may also feed into this issue. These effects might be significant enough to give false trends as seen in Figure 8.22, especially in the region immediately downstream of the first corner where the fluctuations initially start growing. On the other hand, quantifying the fluctuations with the spectral analysis and using the power content only in the frequency range of interest might give better results, due to the filtering process of this technique.

8.6. Heat-Transfer-Rate Fluctuation Growth Using the Spectral Method

The analysis presented above is repeated in this section using the spectral analysis method. The same set of data with 15 roughness strips (0.18 inch spacing) is used to be consistent with the previous section. The spectra of the fluctuations on the second compression ramp show a peak wavenumber at 4.7 cycles/inch, for this roughness spacing (Figure 8.18). The streamwise variation of the power spectral density (PSD) at this wave number is shown in Figure 8.27. Here, only the lowest, medium, and highest total pressure cases are shown for the largest roughness thickness (2.25 mils). Also shown are the PSD's of four adjacent wavenumbers, two wavenumbers below the peak and two wavenumbers above the peak. For the most part, the PSD of the peak wavenumber stays higher than the other wavenumbers. The PSD's at 4.18 and 5.23 cycles/inch are also consistently greater than the PSD's at 3.66 and 5.75 cycles/inch. The PSD in this wavenumber range is integrated, and the streamwise power distribution is

shown in Figure 8.28. The trends shown here are very similar to the trends seen in Figure 8.22 with the RMS of the fluctuations. In general the power increases with increasing roughness thickness, but there is no clear trend with the total pressure for each roughness-thickness case.

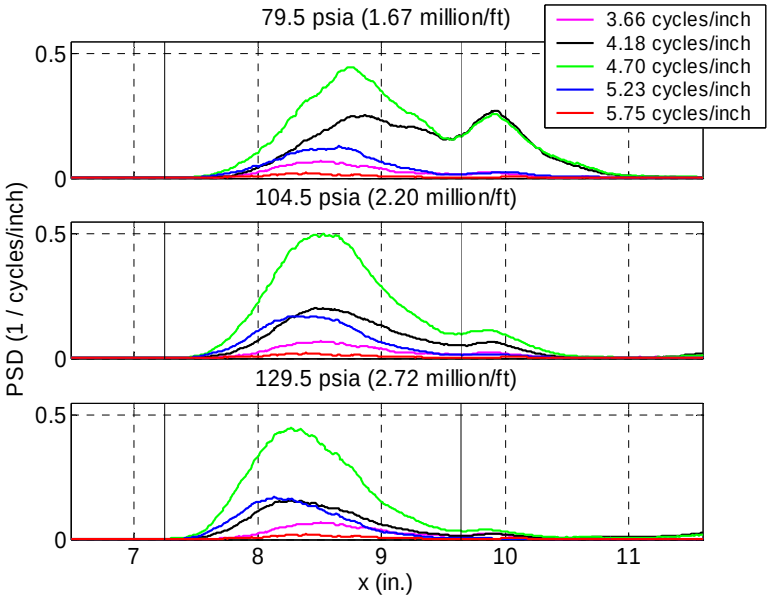

Figure 8.27. Streamwise variation of the power spectral density. All cases shown are with 15 roughness strips (0.18 inch spacing) of maximum thickness (2.25 mils) applied.

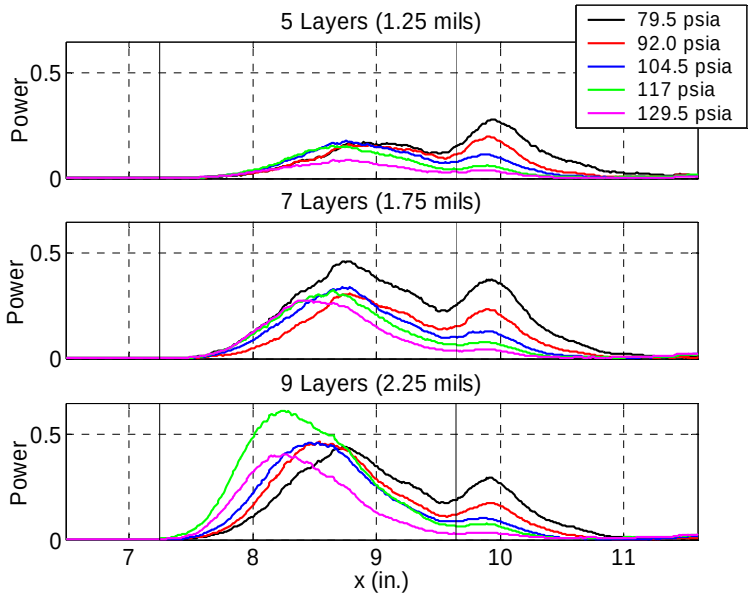

Figure 8.28. Streamwise growth of the power. All cases shown are for the cases with 15 roughness strips (0.18 inch spacing).

The power increases past the first corner to a maximum, and then decay, with a second local maximum on the third ramp.

The streamwise amplitude ratios are shown in Figures 8.29-8.33 for all five roughness spacing. The streamwise power distribution is normalized by the initial power. The initial power is computed by averaging the power over the first compression ramp, similar to the analysis shown in the previous section. The 17 roughness case (0.16 inch spacing) seems to show the largest growth, when 7 or 9 layers are used. Overall, the amplitude ratios decrease as the roughness spacing is decreased and increased. However, this trend is not as clear when 5 layers are used. The 5 layer roughness may not be large enough to generate disturbances of sufficient initial amplitude which would show systematic trends. Close examination of each set of data does not show any consistent systematic trends with total pressure. For example, the highest total pressure case does not necessarily show the earliest or largest growth. This very well may be the result of effects such as saturation. However, it is most likely the result of inconsistent initial amplitudes due to the signal content on the first compression ramp being mostly noise, as with before.

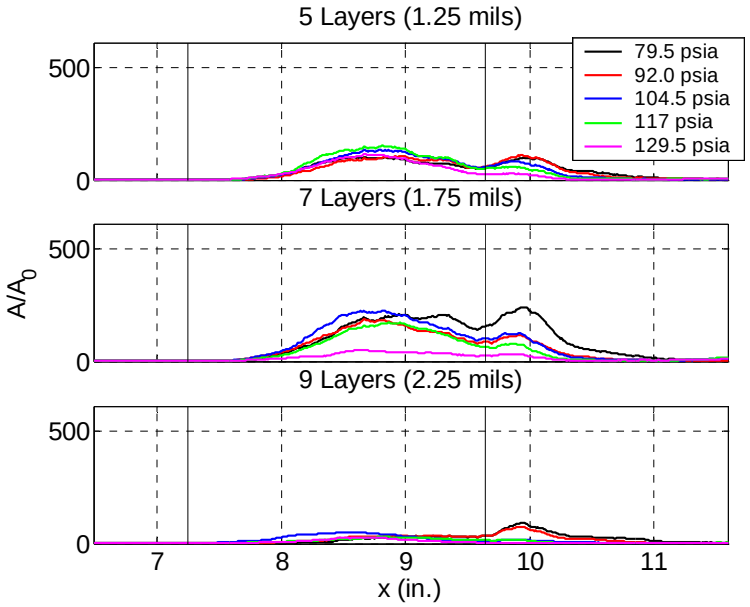

Figure 8.29. Streamwise growth of the amplitude ratio. All cases shown are for the cases with 13 roughness strips (0.21 inch spacing).

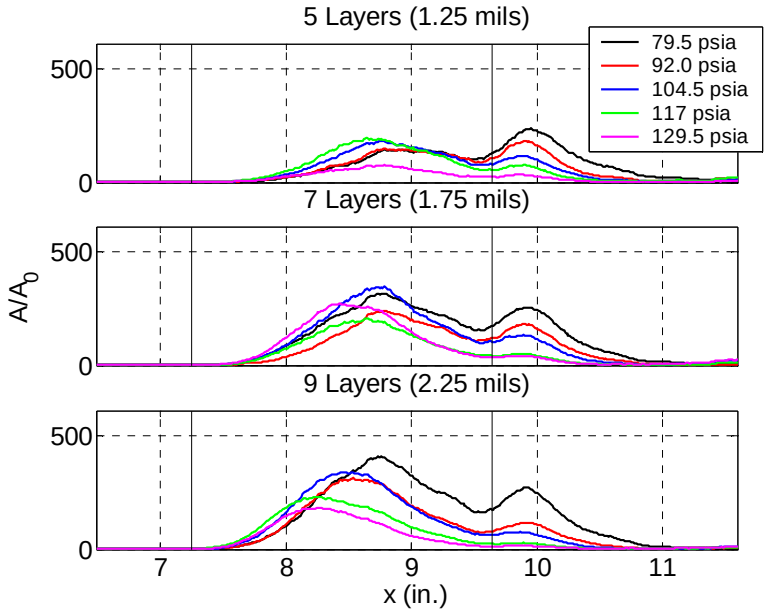

Figure 8.30. Streamwise growth of the amplitude ratio. All cases shown are for the cases with 15 roughness strips (0.18 inch spacing).

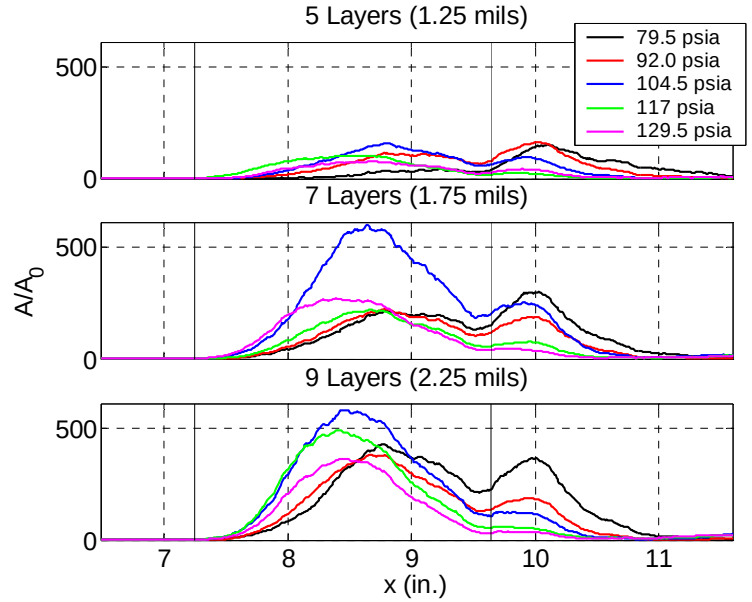

Figure 8.31. Streamwise growth of the amplitude ratio. All cases shown are for the cases with 17 roughness strips (0.16 inch spacing).

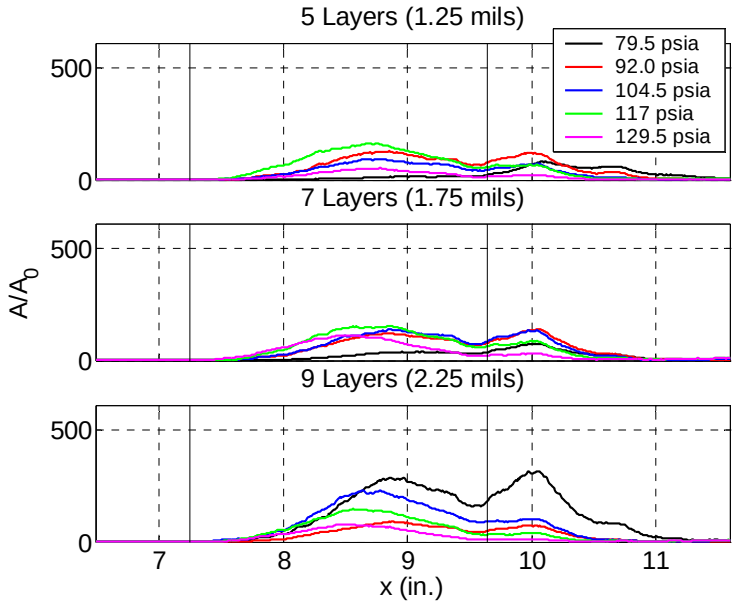

Figure 8.32. Streamwise growth of the amplitude ratio. All cases shown are for the cases with 19 roughness strips (0.14 inch spacing).

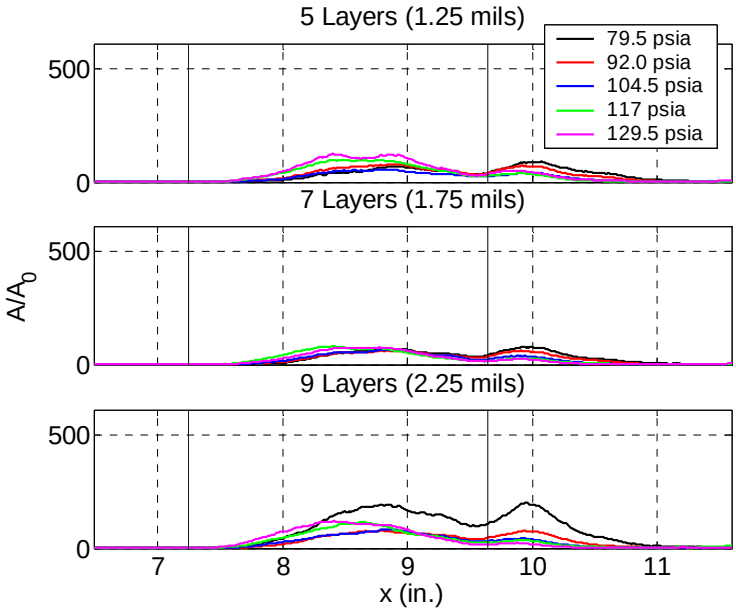

Figure 8.33. Streamwise growth of the amplitude ratio. All cases shown are for the cases with 21 roughness strips (0.125 inch spacing).

The initial disturbance amplitudes are shown in Figure 8.34. The figure does not show any systematic trends with total pressure, roughness spacing, nor roughness thickness. Future research must examine different means of quantifying the initial amplitude.

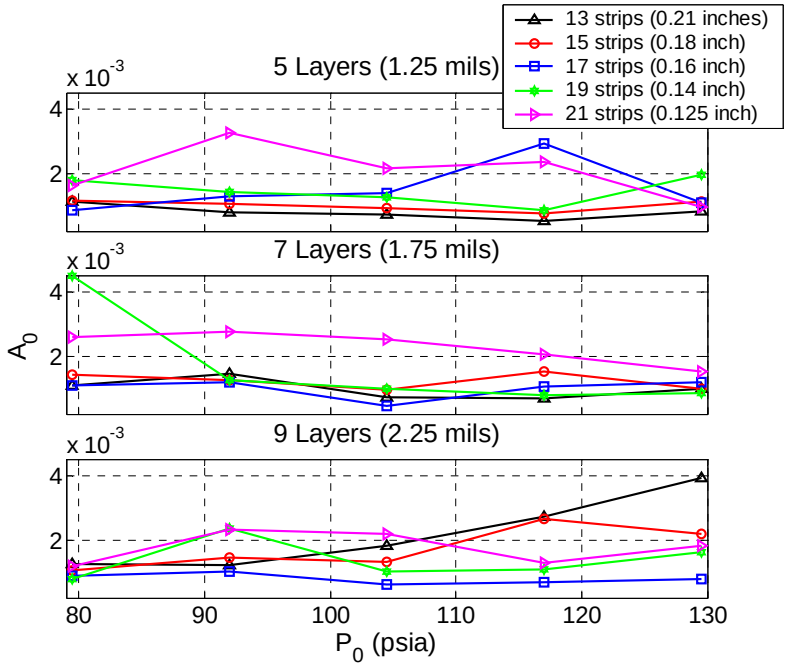

Figure 8.34. Variation of initial disturbance amplitudes.

The power distribution is normalized by the maximum power for each case, and is re-plotted in Figure 8.35. The process is repeated using the maximum power values only on the second ramp, and are shown in Figure 8.36.

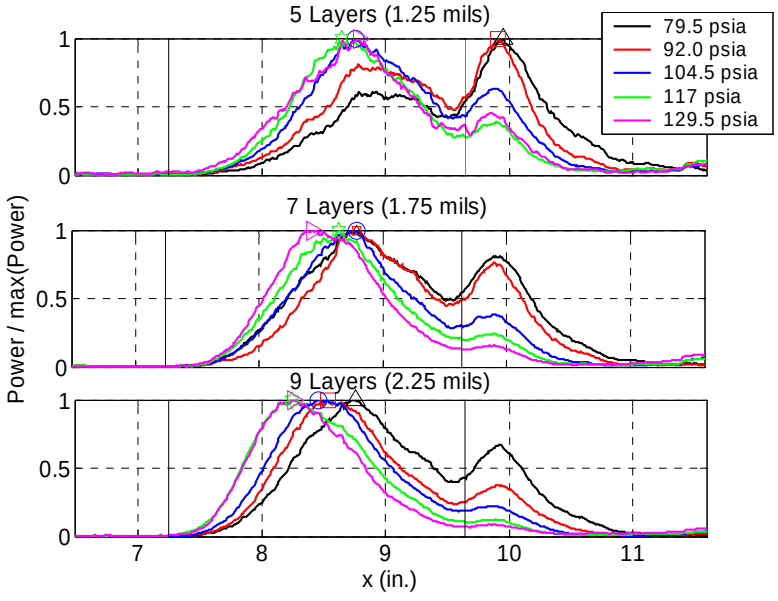

Figure 8.35. Streamwise growth of the power normalized by the maximum power. All cases shown are for the cases with 15 roughness strips (0.18 inch spacing).

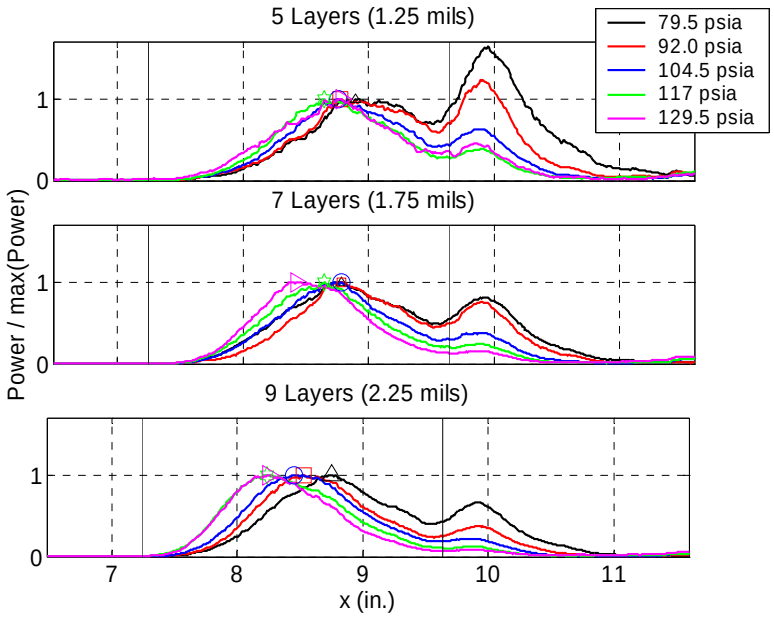

Figure 8.36. Streamwise growth of the power normalized by the maximum power on the second compression ramp. All cases shown are for the cases with 15 roughness strips (0.18 inch spacing).

The first two cases result in similar trends to the data shown previously with the RMS fluctuations. The normalization procedure tends to improve the presentation of the data, and some of the expected trends become visible. Again, there is not much of a difference between the first two normalization schemes, because only the two lower total pressure cases with the smallest roughness thickness is affected.

However, normalizing the power with the maximum value strictly on the third compression ramp seems to result in consistent trends for several cases of the complete dataset. This was still chosen as the preferred normalization method for the spectral approach here. The power distribution along the streamwise coordinate are shown in Figures 8.37-8.41 for all five roughness spacing investigated. The general expected trend is seen for the majority of the cases. The cases with 13 strips with a thickness of 1.75 mils, and all roughness spacing cases with a 1.25 mil thickness show some abnormal trends, where the power for some of the lower pressure cases grow earlier and more than the higher pressure cases. The causes of these anomalies are not known. In some respects, it can be expected that the smallest thickness roughness cases will tend to show disagreement with expectations and with cases with thicker roughness.

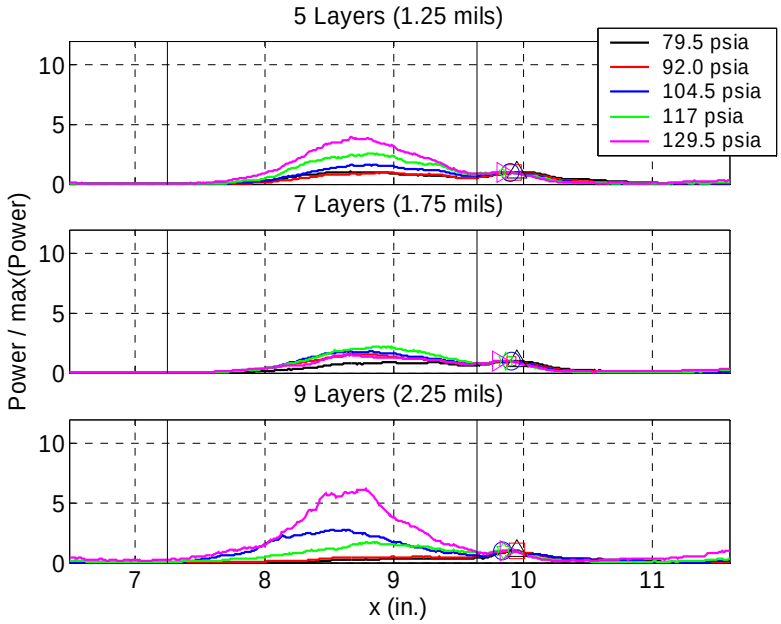

Figure 8.37. Streamwise growth of the power normalized by the maximum power on the third compression ramp. All cases shown are for the cases with 13 roughness strips (0.21 inch spacing).

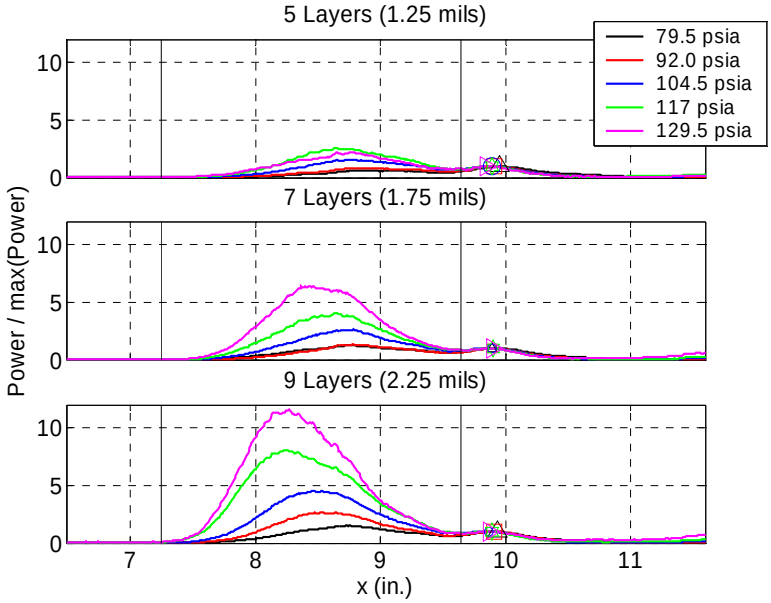

Figure 8.38. Streamwise growth of the power normalized by the maximum power on the third compression ramp. All cases shown are for the cases with 15 roughness strips (0.18 inch spacing).

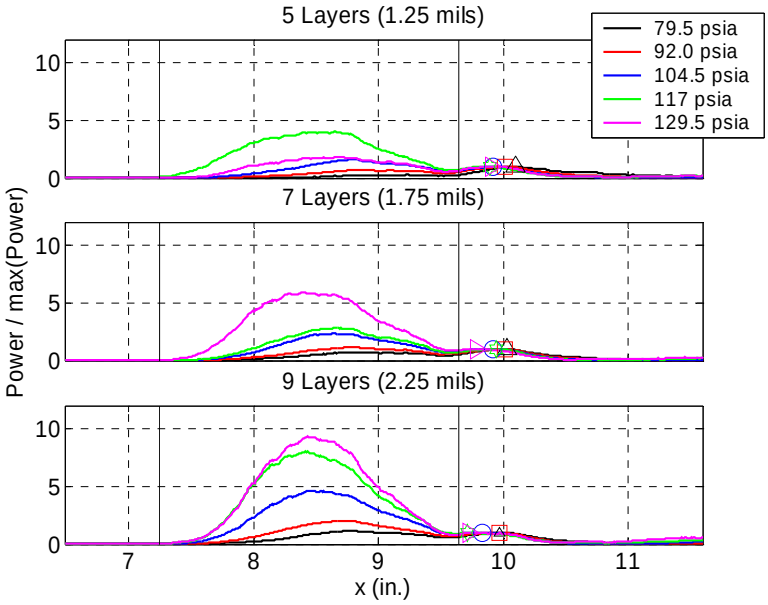

Figure 8.39. Streamwise growth of the power normalized by the maximum power on the third compression ramp. All cases shown are for the cases with 17 roughness strips (0.16 inch spacing).

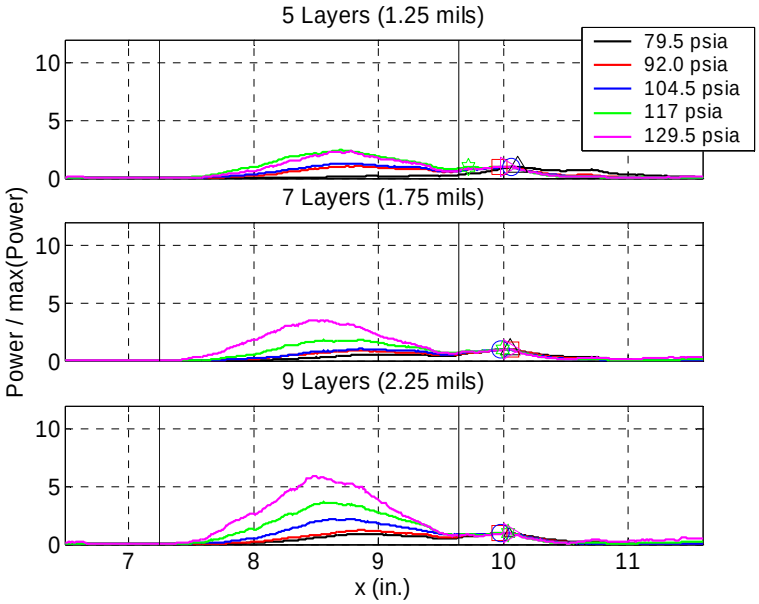

Figure 8.40. Streamwise growth of the power normalized by the maximum power on the third compression ramp. All cases shown are for the cases with 19 roughness strips (0.14 inch spacing).

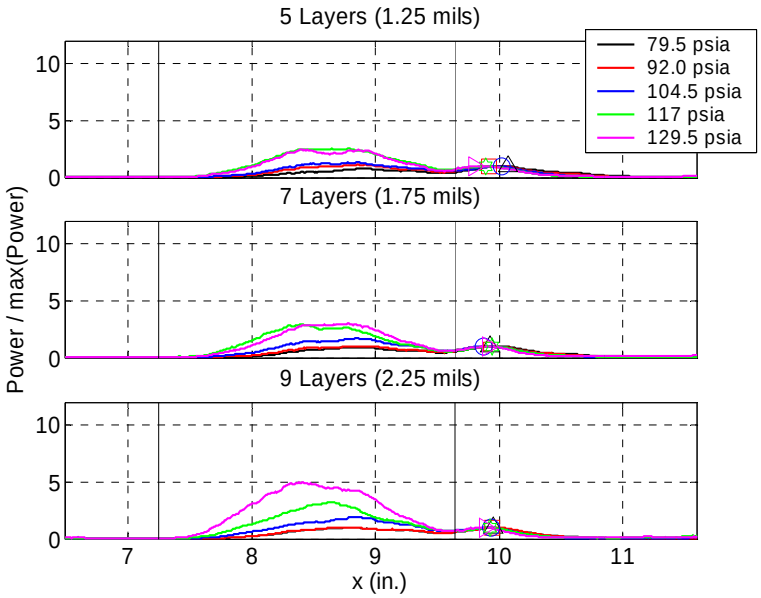

Figure 8.41. Streamwise growth of the power normalized by the maximum power on the third compression ramp. All cases shown are for the cases with 21 roughness strips (0.125 inch spacing).

The streamwise vortices for these small thickness cases are not as strong, which does not cause a large enough heating to show clear fluctuations in the TSP images. However, this problem is potentially seen only for the two highest total pressure cases. If the above hypothesis is indeed the problem, then the disagreements and problems should be seen at the lower pressures, and not so much at the higher pressures.

Some of the representative cases are re-plotted in Figures 8.42 and 8.43 to illustrate the effects of roughness spacing and thickness more clearly. All cases shown in Figure 8.42 are for the highest total pressure of 129.5 psia. It was previously discussed that the vortex spacing of 0.19 inches seen with the oil-flow experiments is probably the most amplified, or dominant wavelength. The 15 and 17 roughness strips have spacings of 0.18 and 0.16 inches respectively, and the spacings of the resulting streamwise vortices on the second compression ramp are 0.024 and 0.021 inches respectively, taking into account the spreading due to cross-flow. All else equal, the cases with these two roughness spacings should result in the largest and earliest instability wave growth. This is seen for the case with 1.75 and 2.25 roughness thickness cases, but not with the 1.25 mil thickness case. This discrepancy is most likely caused by whatever was causing the

problems seen in Figures 8.37-8.41 for the smallest thickness cases. However, it is encouraging to see the expected trends show very clearly in Figure 8.43.

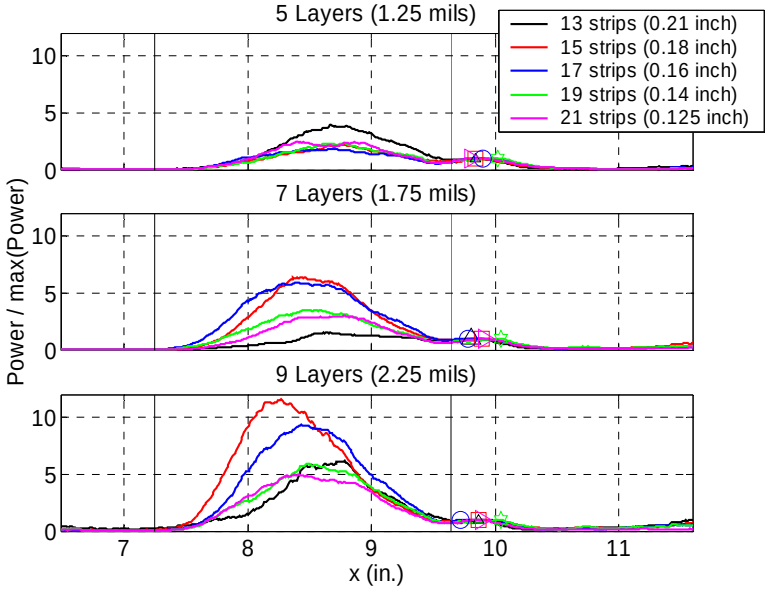

Figure 8.42. Streamwise growth of the power normalized by the maximum power on the third compression ramp. All cases shown are for the cases at the highest total pressure of 129.5 psia (2.72 million/ft).

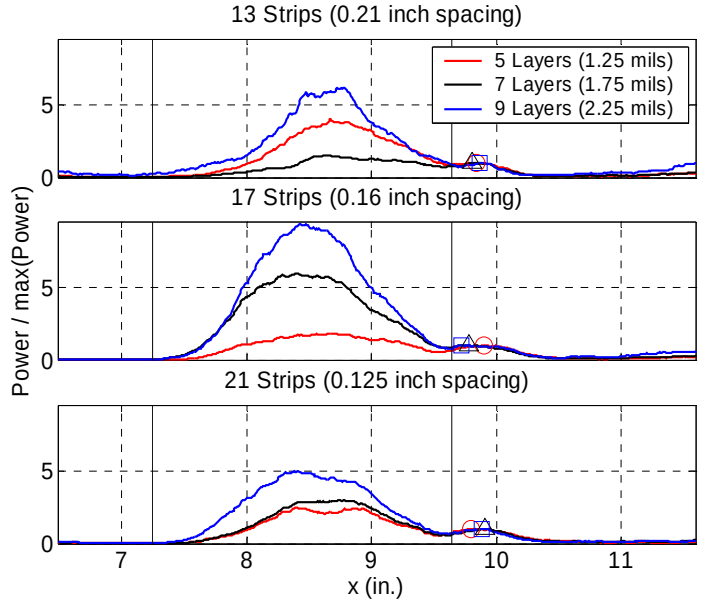

Figure 8.43. Streamwise growth of the power normalized by the maximum power on the third compression ramp. All cases shown are for the cases at the highest total pressure of 129.5 psia (2.72 million/ft).

Here, all cases shown are at the highest total pressure of 129.5 psia. The thickest roughness case which probably generates the strongest disturbances shows the largest growth and earliest growth. This trend is seen for the 17 and 21 roughness cases.

Although many of these figures that use the maximum power as the normalization value show systematic trends and correlations, it is not known what this type of amplitude ratio physically represents. Because of this lack of a physical understanding, it is difficult to assess whether the systematic trends with the total pressure, roughness spacing, and roughness thickness really are related to instability and transition. If the transition onset could be determined, then these amplitude ratios could possibly be related to it and assessed if they have any significance. Until the transition onset becomes available through improvement of the experimental technique, instability computations will be necessary to examine the data presented here more thoroughly.

8.7. Maximum Amplitude Ratio

The normalized power distributions shown in the previous section are in some sense an amplitude ratio, which describes the integrated total growth of the instability waves. This information is generally used to correlate the N-factor in the e^N method with the transition onset. Strictly speaking the N-factor describes the wave growth referenced to the magnitude of the initial disturbance. However, the data presented above was in some sense the inverse of the integrated amplification ratio, using the maximum amplitude as the reference point. Nonetheless, the maximum value of the normalized power for each cases presented above should be useful information, and are summarized in this section.

It was hypothesized earlier that the streamwise location corresponding to the maximum normalized power might be intimately related to transition onset. Because the power distribution is normalized strictly by the maximum power on the third compression ramp, the first peak in the normalized power distribution on the second compression ramp seems to show some of the expected trends. These values are defined here as the maximum amplitude ratio, and are shown in Figure 8.44 for the complete dataset. In

general, this value increases with total pressure, and also for the 1.75 and 2.25 mil roughness thickness cases, the cases with 15 and 17 roughness strips show the largest values. This result is consistent with the anticipated most amplified wavelength determined from the oil-flow experiments.

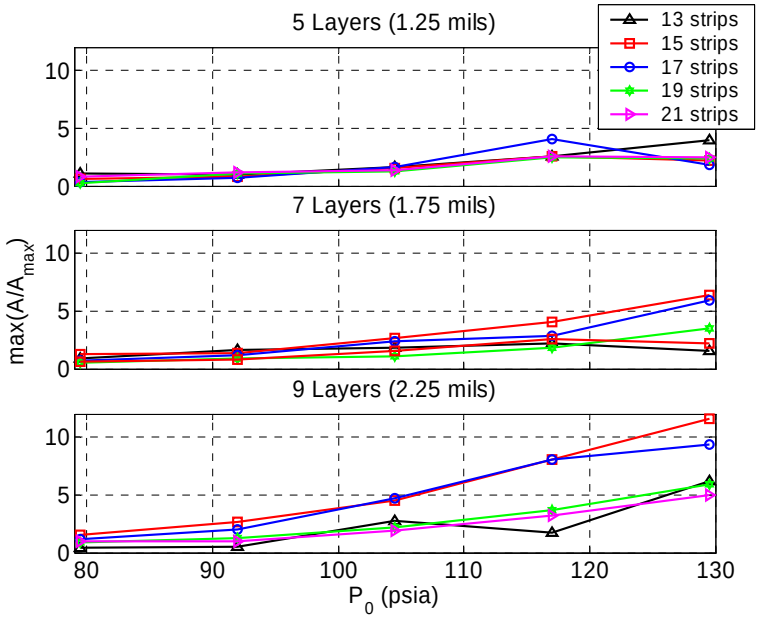

Figure 8.44. Maximum amplitude ratios on the second compression ramp.

The streamwise coordinates of this maximum amplitude ratio are shown in Figure 8.45. It is expected that these values should in general decrease with total pressure, signifying that the disturbances are growing earlier and faster. Overall the data seem to show this, but as with before, some of the cases show discrepancies. This trend is most clearly seen for the cases with 15, 17, and 19 strips of roughness. The roughness spacings for these cases are the closest to the spacing of the naturally occurring streamwise vortices, so it is very possible that these cases are resulting in the cleanest set of data.

The data shown in Figures 8.44 and 8.45 are shown against the roughness spacing in Figures 8.46 and 8.47. As with presenting the data against the total pressure, these figures also tend to show the expected trend in a general sense, although they do have inconsistencies. Each series of plots should reach a peak value near 0.19 inch spacing. This trend is only seen for few of the cases. Similarly for Figure 8.47, the streamwise

coordinates of the maximum amplitude ratio should have a minimum point near 0.19 inch spacing, but the trend is only seen for few of the cases.

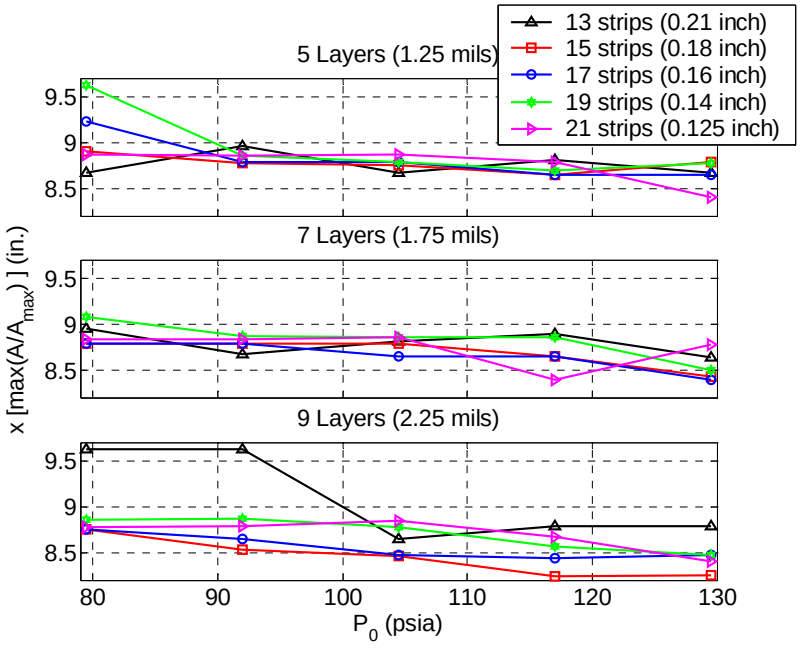

Figure 8.45. Streamwise coordinate of the maximum amplitude ratio on the second compression ramp.

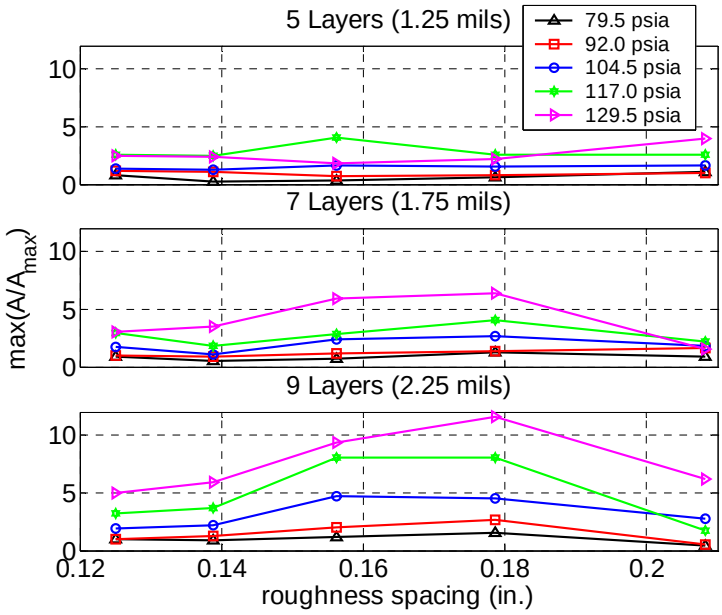

Figure 8.46. Maximum amplitude ratios on the second compression ramp.

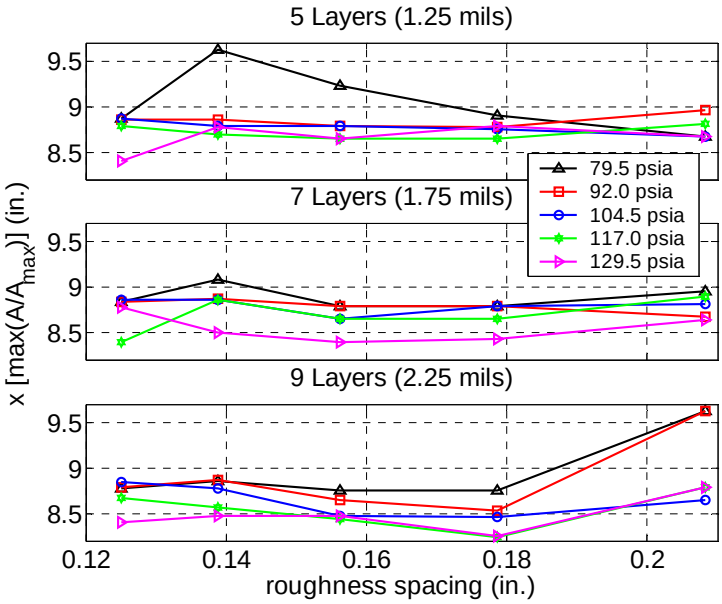

Figure 8.47. Streamwise coordinate of the maximum amplitude ratio on the second compression ramp.

9. CONCLUSIONS

Oil-flow visualization and temperature-sensitive-paints measurements were used to infer the instability of streamwise vortices on a scramjet forebody model. The experiments were carried out in a conventional facility in terms of the freestream noise levels. Oil-flow visualization was used to map the separation line upstream of the first compression corner, and to measure the spacing of "naturally" occurring streamwise vortices in the absence of controlled disturbance generators. The addition of fluorescent pigmentation to the oil and the use of a blue light source successfully eliminated reflections off the window. The oil-flow experiments mainly provide qualitative information about the overall flow structures, but quantitative measurements such as the separation onset were also obtained. Two oil-flow approaches were tried as part of this research. The traditional oil-dot technique shows the separation zone, but the 200 cs viscosity oil does not move enough during the limited tunnel run time to be able quantify the spatial extent of the separation zone. On the other hand, the painted-oil approach does not show the reattachment point, but the separation onset shows up very clearly.

Temperature-sensitive-paint was then used to infer the presence of streamwise vortices and the computed heat-transfer rates were used to quantify the instability. The systematic trends seen with Reynolds number suggests that the growth of the spanwise-varying heat-transfer rates is related to boundary-layer instability and transition. However, several problems with the current implementation of the TSP technique to this facility have been identified through comparison of the results to CFD data. A constant thickness adhesive tape should probably be used for the insulator. The thickness variation with the painted approach results in significant uncertainty. This problem could not be corrected even if several thickness measurements are made and used in the form of a thickness grid. The need to pressurize the test section to full stagnation pressure introduces difficulty in obtaining a reasonable wind-off reference image. The use of a

wind-off image at high pressure under-predicts the heating, and a wind-off image at vacuum pressure over-predicts the heating. The sensitivity of the TSP to pressure thus has a significant impact on the quantitative results. The pressure sensitivity of the TSP and its response time to pressure change must be quantified and known to improve the quantitative measurements.

The streamwise vortices appeared immediately after reattachment downstream of the first compression corner in the oil-flow experiments, which might suggest a Görtler-like instability mechanism. This observation is consistent with oil-flow images available from other conventional facilities such as Langley's 20-inch Mach 6. The spacing of the streamwise vortices in the oil-flow was not affected by unit Reynolds number. One would expect that changing the unit Reynolds number changes the boundary-layer thickness, which would change the spacing of the vortices as well. This lack of variation with unit Reynolds number might be an indication that the disturbances were generated from imperfections in the leading edge. The leading edge imperfections were found to be substantial in simple measurements. On the other hand, the Hyper-X model used by Langley had a much higher quality leading edge, and also showed vortices in the absence of applied roughness.

The quantitative measurements using temperature-sensitive-paints seem to show systematic trends, and provide information about this instability mechanism involving streamwise vortices. For all the final roughness configurations and flow conditions tested here, the vortices first appeared also on the second compression ramp. Vortices were visible on the first compression ramp upstream of the first compression corner when larger roughnesses were used in the preliminary experiments. The vortex spacing directly relates to the roughness spacing, and was independent of unit Reynolds number as with the oil-flow experiments. A statistical and spectral analysis showing the magnitude of the spanwise heat-transfer fluctuations seems to show a systematic trend with unit Reynolds number. As unit Reynolds number increases, the peak in the fluctuations moves upstream. However, this trend was not consistent for the entire parameter space, making it difficult to reach a definitive and generalized conclusion. Comparison with computations is needed. Whether the two sets of data agree or not, this

will provide a further knowledge of this type of instability mechanism, and also help to guide future experiments which should be performed once the measurement technique is refined.

10. RECOMMENDATIONS

10.1. Imaging System

The digital still cameras used for this present research did not have an external electronic triggering capability. In some sense this forced the use of the digital video camera to capture the oil movement during the entire tunnel run. However, the video camera generally did not produce high quality images because of the significantly lower pixel resolution. Investment in a digital still camera with an external triggering capability, together with some sort of timing device (such as an oscilloscope) would eliminate the need for a video camera and provide much higher quality images. Although for this present research the frames from the video were of sufficient quality, a higher resolution camera should be used for future experiments to capture detailed flow structures. This would allow the visualization of flows around boundary-layer trips, surface disturbance generators, etc.

The advantage of a higher-resolution CCD camera for the TSP experiments is not clear. However, the use of a 14-bit camera investigated for this research, seemed to result in lower noise levels. This has the potential of measuring smaller amplitude instabilities, which would allow for improved amplitude ratios. The spectral resolution was also limited by the spatial resolution of the CCD camera. The TSP images showed a spanwise spreading of the vortices from the second to the third compression ramp. However, this variation was too small to quantify with the spectral analysis approach. A camera with a higher spatial resolution would increase the attainable spectral resolution, resulting in a more precise measurement of the wavenumber and spreading rate of the instabilities.

10.2. Oil-Flow Visualization Experimental Method

The oil-flow visualization experiments suffered mostly because of the small oil movement. The run time is limited to less than 10 seconds in this facility, so the oil movement must be enhanced by either using thinner viscosity oil, applying some sort of surface repellant substance such as Rain-X®, or both. Both of these options must be thoroughly tested to insure that they do not craze the Plexiglas window. 50 cs oil was applied to a sample Plexiglas for several days, with no visually noticeable effects. However, the manufacturer quoted possible effects to the Plexiglas, and it must be extensively investigated to draw definitive conclusions.

Two oil-flow techniques were employed in order to visualize different aspects of the flow structure. It may be possible to combine the two approaches so that the disadvantages of each method could be covered by the advantages of the other. Oil-dots with a pigmentation that is of different color than the base layer could be applied. This approach may require two cameras with separate filters, but it might be possible to acquire the surface streamlines from the dots, and the separation zones from the painted layer simultaneously, increasing the productivity of the facility.

10.3. Temperature-Sensitive-Paint Experimental Method

Comparison of the streamwise heat-transfer rate distribution with CFD results showed an order of magnitude difference. At present the overall TSP technique is suspected to be the main cause. Improvements are necessary in three specific areas. First, the uniformity of the insulator must be improved. This showed to have significant effects in the computed heat-transfer rates. The thickness can be made more uniform by spraying several thin layers while taking measurements of the thickness distribution and sanding down accordingly after each coating. However, this would potentially be extremely time-consuming, perhaps taking weeks to achieve a desired insulator painting. An alternative would be to use an adhesive tape, such as those used for model airplane applications. This might be practical on the main compression ramps of the Hyper-2000

model. However, these would be difficult to smoothly apply to models with significant curvature, corners, and edges.

The luminescence response of the TSP to pressure must also be thoroughly measured. Preliminary data showed that the pressure at which the wind-off reference image is acquired has a significant effect on the computed heat-transfer rate. The extent to which pressure sensitivity is introducing experimental error has not been quantified, but it is clear that a calibration against pressure between the full pressure ranges of the facility is necessary. In addition, the response time of the TSP to pressure should be measured so that the appropriate pressure value could be used when applying the calibration. A new binder material with lower oxygen permeability could also be sought to reduce the pressure sensitivity.

As stated above, the method in which the wind-off reference image is acquired must be re-worked. Using a wind-off image acquired at vacuum pressures over-predicts the heat-transfer rate, whereas a wind-off image acquired at full stagnation pressure under-predicts the heating. The wind-off image may need to be acquired at some intermediate pressure to take into account the response time, or a separate pressure correction may need to be applied to the images.

10.4. Data Processing Method

The image-processing and the heat-transfer model developed for this research was an elementary model, with room for significant improvements. The image-processing software used a two-dimensional equation, which has limitations in terms of the achievable spatial accuracy. These two-dimensional equations may not correct the window distortion to the maximum extent possible either. These issues were not a problem for this research because the model geometry was relatively simple, consisting of three flat plates at angle of attack. However, more complicated geometries which may be of interest for future research will require the use of the collinearity equations or the direct linear transform with lens distortion terms. Depending on how these techniques are employed, a camera calibration methodology may also become necessary.

The error in the computed heat-transfer rates may also be the result of the heat-transfer model, in addition the problems with the TSP experimental technique discussed above. The present heat-transfer model may not be accurate enough to model all of the necessary effects seen for this heat-transfer problem. Effects such as multi-layer, finite thickness, and unsteadiness, may be necessary especially for thin models such as the Hyper-2000. In addition, multi-dimensional effects may need to be considered to improve the instability measurements and analysis.

10.5. Model Improvement

Measurements of the leading edge thickness of the model showed significant variations along the span. Many of the parametric trends observed in the experiments are suspected to be caused by these leading edge imperfections which set the instability characteristics. The leading edge should be worked to a more uniform thickness distribution. In addition, it is desirable to round the edges and create a smooth radius. However, it is not trivial to hand-work a leading edge which is only 10 mils thick to begin with. It may be easier to manufacture a new steel model using a 5-axis CNC machine. This would of course make the model much more costly.

10.6. Additional Experiments

Many of the flaws in the TSP experimental technique and data reduction models were discussed. The experiments performed for this research should be repeated once the experimental issues are worked out. This may result in a better dataset which shows consistent parametric trends. Also, it will be possible to relate the instability measurements to the transition onset, allowing for a thorough comparison to computational results when they are available. This will open up the possibilities to exploring many other issues, such as the effect of the leading edge imperfections, tunnel noise, and so on.

LIST OF REFERENCES

LIST OF REFERENCES

[1] Bouslog, S.A., An, M.Y., Hartmann, L.N., and Derry, S.M. Review of Boundary Layer Transition Flight Data on the Space Shuttle Orbiter. Paper 91-0741, AIAA, January 1991.

[2] Goodrich, W.D., Derry, S.M., and Bertin, J.J. Shuttle Orbiter Boundary Layer Transition at Flight and Wind Tunnel Conditions. *Shuttle Performance: Lessons Learned*, NASA CP-2283 Part I, pg. 753-779, 1983.

[3] Harthun, M.H., Blumer, C.M., and Miller, B.A. Orbiter Windward Surface Entry Heating: Post-Orbital Flight Test Program Update. *Shuttle Performance: Lessons Learned*, NASA CP-2283 Part I, pg. 781-804, 1983.

[4] Berry, S.A., Horvath, T.J., Hollis, B.R., Thompson, R.A., and Hamilton II, H.H. X-33 Hypersonic Boundary-Layer Transition. *Journal of Spacecraft and Rockets*, 38(5):646-657, September-October 2001.

[5] Palmer, G., Kontinos, D., and Sherman, B. Surface Heating Effects of X-33 Vehicle Thermal-Protection-System Panel Bowing. *Journal of Spacecraft and Rockets*, 36(6):836-841, November-December 1999.

[6] McClinton, C.R., Rausch, V.L., Sitz, J., and Reukauf, P. Hyper-X Program Status. Paper 2001-0828, AIAA, January 2001.

[7] Whitehead Jr., A. NASP Aerodynamics. Paper 89-5013, AIAA, July 1989.

[8] Johnson, D., Espinosa, A., and Althuis, J. NASP Derived Vehicles: Not Just to Space! Paper 92-5020, AIAA, December 1992.

[9] Heiser, W.H. and Pratt, D.T. Hypersonic Airbreathing Propulsion, AIAA Education Series, Copyright 1994, New York.

[10] An, M.Y., Wang, K.C., Campbell, C.H., and Pelley, R.L. Space Shuttle Orbiter Aerodynamics Induced by Asymmetric Boundary-Layer Transition. Paper 96-0808, AIAA, January 1996.

[11] Hingst, U.G. Laminar/Turbulent Flow Transition Effects on High-Speed Missile Domes. AGARD CP-493, pg. 27.1-27.8, 1990.

[12] Korejwo CDR, H.A. and Holden, M.S. Ground Test Facility for Aerothermal and Aero-Optical Evaluations of Hypersonic Interceptors. Paper 92-1074, AIAA, February 1992.

[13] Defense Science Board, Report of the Defense Science Board Task Force on the National Aerospace Plane (NASP). DTIC Citation AD-A201 124, September 1988.

[14] Defense Science Board, Report of the Defense Science Board Task Force on National Aero-Space Plane (NASP) Program. DTIC Citation AD-A274 530, 94-00052, November 1992.

[15] Jaffe, N.A., Okamura, T.T., and Smith, A.M.O. Determination of Spatial Amplification Factors and Their Applications to Predicting Transition. *AIAA Journal*, 8(2):301-308, February 1970.

[16] Reshotko, E. Boundary Layer Instability, Transition and Control. Paper 94-0001, AIAA, January 1994.

[17] Bushnell, D.M., Malik, M.R., and Harvey, W.D. Transition Prediction in External Flows via Linear Stability Theory. Symposium Transsonicum III, pg. 225-242, Springer-Verlag, 1989, Proceedings of an IUTAM Sympsium held May 1988.

[18] Kleiser, L. and Zang, T. Numerical Simulation of Transition in Wall-Bounded Shear Flows. *Annual Review of Fluid Mechanics*, 23:495-537, 1991.

[19] Reed, H.L. Direct Numerical Simulation of Transition: The Spatial Approach. AGARD Report 793, Special Course on Transition Modeling, 1993.

[20] Herbert, T. On the Stability of 3D Boundary Layers. Paper 97-1961, AIAA, June 1997.

[21] Herbert, T. Parabolized Stability Equations, AGARD Report 793, Special Course on Progress in Transition Modelling, pg. 4.1-4.34, 1994.

[22] Herbert, T. Parabolized Stability Equations. *Annual Review of Fluid Mechanics*, 29:245-283, 1997.

[23] Janke, E. Receptivity and Transition Control of Swept-Wing Boundary-Layers; Effects of Surface Curvature and Nonlinearity. Paper 2001-2980, June 2001.

[24] Schneider, S.P. and Haven, C.E. Quiet-Flow Ludweig Tube for High-Speed Transition Research. *AIAA Journal*, 33(4):688-693, April 1995.

[25] Pate, S.R. Effects of Wind Tunnel Disturbances on Boundary-Layer Transition with Emphasis on Radiated Noise: A Review. Paper 80-0431, AIAA, March 1980.

[26] Pate, S.R. and Schueler, C.J. Radiated Aerodynamic Noise Effects on Boundary-Layer Transition in Supersonic and Hypersonic Wind Tunnels. *AIAA Journal*, 7(3):450-457, March 1969.

[27] Schneider, S.P. Effects of High-Speed Tunnel Noise on Laminar-Turbulent Transition. *Journal of Spacecraft and Rockets*, 38(3):323-333, May-June 2001.

[28] Chen, F.J. Malik, M.R., and Beckwith, I.E. Boundary-Layer Transition on a Cone and Flat Plate at Mach 3.5. *AIAA Journal*, 27(6):687-693, June 1989.

[29] Schneider, S.P. and Skoch, C. Mean Flow and Noise Measurements in the Purdue Mach-6 Quiet-Flow Ludwieg Tube. Paper 2001-2778, AIAA, June 2001.

[30] Schneider, S.P., Skoch, C., Rufer, S., Matsumura, S., and Swanson, E. Transition Research in the Boeing/AFOSR Mach-6 Quiet Tunnel. Paper 2002-0302, AIAA, January 2002.

[31] Schneider, S.P., Matsumura, S., Rufer, S., Skoch, C., and Swanson, E. Hypersonic Stability and Transition Experiments on Blunt Cones and a Generic Scramjet Forebody. Paper 2003-1130, AIAA, January 2003.

[32] Schneider, S.P., Matsumura, S., Rufer, S., Skoch, C., and Swanson, E. Progress in the Operation of the Boeing/AFOSR Mach-6 Quiet Tunnel. Paper 2002-3033, June 2002.

[33] Blanchard, A.E., Lachowicz, J.T., and Wilkinson, S.P. NASA Langley Mach 6 Quiet Wind-Tunnel Performance. *AIAA Journal*, 35(1):23-28, January 1997.

[34] Swanson, E. Mean Flow Measurements and Cone Flow Visualization at Mach 6. Master's Thesis, School of Aeronautics and Astronautics, Purdue University, December 2002.

[35] Matsumura, S., Huang, C., Choi, Y.S., Swanson, E.O., Salyer, T.R., and Sakaue, H. Feasibility of Detecting Streamwise Vortices from Roughness Elements Using Temperature Sensitive Paint in a Mach 4 Ludwieg Tube. Paper 2002-3238, AIAA, June 2002.

[36] Sakaue, H. and Matsumura, S., Schneider, S.P., and Sullivan, J.P. Anodized Aluminum Pressure Sensitive Paint for Short Duration Testing. Paper 2002-2908, AIAA, June 2002.

[37] Mack, L.M. Boundary-Layer Stability Theory. AGARD Report 709, Presented at the the AGARD Special Course on Stability and Transition, March 1984.

[38] Ladoon, D.W. Wave Packets Generated by a Surface Glow Discharge on a Cone at Mach 4. Doctoral Thesis, School of Aeronautics and Astronautics, Purdue University, December 1998.

[39] Schmisseur, J.D. Receptivity of the Boundary Layer on a Mach-4 Elliptic Cone to Laser-Generated Localized Freestream Perturbations. Doctoral Thesis, School of Aeronautics and Astronautics, Purdue University, December 1997.

[40] Reed, H., Saric, W., Lyttle, I., and Asada, Y. Stability and Control of High-Speed Flows. Paper 2001-2700, AIAA, June 2001.

[41] Berry, S.A., Auslender, A.H., Dilley, A.D., and Calleja, J.F. Hypersonic Boundary-Layer Trip Development for Hyper-X. *Journal of Spacecraft and Rockets*, 38(6):853-864, November-December 2001.

[42] Floryan, J.M. On the Gortler Instability of Boundary Layers. *Progress in Aerospace Sciences*, 28:235-271, 1991.

[43] Whang, C.W. and Zhong, X. Receptivity of Gortler Vortices in Hypersonic Boundary Layers. Paper 2002-0151, AIAA, January 2002.

[44] Chapman, D.R., Kuehn, D.M., and Larson, H.K. Investigation of Separated Flows in Supersonic and Subsonic Streams with Emphasis on the Effect of Transition. NACA Report 1356, 1958.

[45] Simeonides, G., Haase, W., and Manna, M. Experimental, Analytical, and Computational Methods Applied to Hypersonic Compression Ramp Flows. *AIAA Journal*, 32(2):301-309, February 1994.

[46] Lewis, J.E., Kubota, T., and Lees, L. Experimental Investigation of Supersonic Laminar, Two-Dimensional Boundary-Layer Separation in a Compression Corner with and without Cooling. *AIAA Journal*, 6(1):7-14, January 1968.

[47] Chpoun, A. Hypersonic Flow in a Compression Corner in 2D and 3D Configurations. Paper 89-1876, AIAA, June 1989.

[48] Cassel, K.W., Ruban, A.I., and Walker, J.D.A. An Instability in Supersonic Boundary-Layer Flow Over a Compression Ramp. *Journal of Fluid Mechanics*, 300:265-285, 1995.

[49] Balakumar, P., Zhao, H., and Atkins, H. Stability of Hypersonic Boundary-Layers Over a Compression Corner. Paper 2002-2848, AIAA, June 2002.

[50] Kosinov, A.D. and Shevelkov, S.G. Epxerimental Investigation of Separation and Stability of Supersonic Laminar Boundary Layer. V.V. Kozlov and A.V. Dovgal, editors, Separated Flows and Jets. Proceedings of the IUTAM Symposium, Novosibirsk, 1990, Berlin, 1991. Springer-Verlag.

[51] Simeonides, G. and Haase, W. Experimental and Computational Investigations of Hypersonic Flow About Compression Ramps. *Journal of Fluid Mechanics*, 283:17-42, 1995.

[52] Nakakita, K., Yamazaki, T., Asai, K., Teduka, N., Fuji, A., and Kameda, M. Pressure Sensitive Paint Measurement in a Hypersonic Shock Tunnel. Paper 2000-2523, AIAA, June 2000.

[53] Ginoux, J.J. On Some Properties of Reattaching Laminar and Transitional High Speed Flows. VKI Technical Note 53, September 1969.

[54] De Luca, L., Cardone, G., Chevalerie, D.A., and Fonteneau, A. Viscous Interaction Phenomena in Hypersonic Wedge Flow. *AIAA Journal*, 33(12):2293-2298, December 1995.

[55] Campbell, B.T., Liu, T., and Sullivan, J.P. Temperature Sensitive Fluorescent Paint Systems. Paper 94-2483, AIAA, June 1994.

[56] Liu, T., Campbell, B.T., Burns, S.P., and Sullivan, J.P. Temperature- and Pressure-Sensitive Luminescent Paints in Aerodynamics. *Applied Mechanics Review*, 50(4):227-246.

[57] Hamner, M.P. Demystifying Luminescent Paint Technology: A Guide for Non-Developers. Paper 2001-2981, AIAA, June 2001.

[58] Liu, T., Campbell, B.T., and Sullivan, J.P. Fluorescent Paint for Measurement of Heat Transfer in Shock-Turbulent Boundary Layer Interaction. *Experimental Thermal and Fluid Science*, 10:101-112, 1993.

[59] Hubner, J.P., Carroll, B.F., Schanze, K.S., Ji, H.F., and Holden, M.S. Temperature- and Pressure-Sensitive Paint Measurments in Short-Duration Hypersonic Flow. *AIAA Journal*, 39(4):654-659, April 2001.

[60] Nakakita, K., Osafune, T., and Asai, K. Global Heat Transfer Measurement in a Hypersonic Shock Tunnel Using Temperature-Sensitive Paint. Paper 2003-0743, AIAA, January 2003.

[61] Asai, K., Kanda, H., Kunimasu, T., Liu, T., and Sullivan, J.P. Boundary-Layer Transition Detection in a Cryogenic Wind Tunnel Using Luminescent Paint. *Journal of Aircraft*, 34(1):34-42, January-February 1997.

[62] Hamner, M.P., Popernack Jr., T.G., Owens, L.R., and Wahls, R.A. Using Temperature Sensitive Paint Technology. Paper 2002-0742, AIAA, January 2002.

[63] McLachlan, B.G., Bell, J.H., Gallery, J., Gouterman, M., and Callis, J. Boundary Layer Transition Detection by Luminescence Imaging. Paper 93-0177, AIAA, January 1993.

[64] Stollery, J.L. Some Viscous Interactions Affecting the Design of Hypersonic Intakes and Nozzles. Bertin, J.J., Periaux, J., and Ballman, J., editors, *Advances in Hypersonics: Defining the Hypersonic Environment*, pg. 418-437, Birkhauser, Boston, 1992.

[65] Bottaro, A., Zebib, A. Gortler Vortices Promoted by Wall Roughness. Fluid Dynamics Research. 19:343-362, 1997.

[66] Schneider, S.P. Fabrication and Testing of the Purdue Mach-6 Quiet-Flow Ludwieg Tube. Paper 2000-0295, AIAA, January 2000.

[67] Schneider, S.P. Design of a Mach-6 Quiet-flow Wind-Tunnel Nozzle Using the e**N Method for Transition Estimation. Paper 98-0547, AIAA, January 1998.

[68] Beckwith, I.E., Chen, F.-J., and Malik, M.R. Design and Fabrication Requirements for Low-Noise Supersonic/Hypersonic Wind Tunnels. Paper 88-0143, AIAA, January 1988.

[69] Schneider, S.P. Design and Fabrication of a 9.5-inch Mach-6 Quiet-Flow Ludwieg Tube. Paper 98-2511, AIAA, June 1998.

[70] Schneider, S.P. Fabrication and Testing of the Purdue Mach-6 Quiet-Flow Ludwieg Tube. Paper 2000-0295, AIAA, January 2000.

[71] Schneider, S.P., Rufer, S.J., Randall, L., and Skoch, C. Shakedown of the Purdue Mach-6 Quiet-Flow Ludwieg Tube. Paper 2001-0457, AIAA, January 2001.

[72] Salyer, T.R. Laser Differential Interferometry for Supersonic Blunt Body Receptivity Experiments. Doctoral Thesis, School of Aeronautics and Astronautics, Purdue University, May 2002.

[73] Kwon, S.W. and Schneider, S.P. Stress Analysis for the Window of the Purdue Quiet-Flow Ludwieg Tube. Paper 2002-0309, AIAA, January 2002.

[74] Matsumura, S. Experiences with Pressure Testing the Plexiglas Window for the Mach 6 Quiet-Flow Ludwieg Tube. Internal Report, School of Aeronautics and Astronautics, Purdue University, August 2001.

[75] Matsumura, S. Experiences with Fixing the Gap Between the Window and the Window Frame for the Mach 6 Tunnel. Internal Report, School of Aeronautics and Astronautics, Purdue University, September 2001.

[76] Schneider, S.P., Collicott, S.H., Schmisseur, J.D., Ladoon, D., Randall, L.A., Munro, S.E., and Salyer, T.R. Laminar-Turbulent Transition Research in the Purdue Mach-4 Quiet-Flow Ludwieg Tube. Paper 96-2191, AIAA, June 1996.

[77] Berry, S.A., DiFulvio, M., and Kowalkowski, K. Forced Boundary-Layer Transition on X-43 (Hyper-X) in NASA LaRC 20-Inch Mach 6 Air Tunnel. NASA TM-2000-210316, August 2000.

[78] Allison, S.W. and Gillies, G.T. Remote Thermography with Thermographic Phosphors: Instrumentation and Applications. *Review of Scientific Instruments,* 68(7):2615-2650, July 1997.

[79] Baker, W.M. Recent Experiences with Pressure Sensitive Paint Testing. Paper 2001-0135, AIAA, January 2001.

[80] Bell, J.H., Schairer, E.T., Hand, L.A., and Mehta, R.D. Surface Pressure Measurements Using Luminescent Coatings. *Annual Review of Fluid Mechanics,* 33:155-206, 2001.

[81] Creswell, L.A. and Cripps, M.N. Independent Pressure and Temperature Measurements from Double Layer Using Fluorescent Lifetime and Radiometric Imaging. Proceedings from the 8th PSP Workshop, 2000.

[82] Sakaue, H., Sullivan, J.P., Asai, K., Iijima, Y., and Kunimasu, T. Anodized Aluminum Pressure Sensitive Paint in a Cryogenic Wind Tunnel. Proceedings of the Instrumentation Society of America, 1999.

[83] Sakaue, H. and Sullivan, J.P. Fast Response Time Characteristics of Anodized Aluminum Pressure Sensitive Paint. Paper 2000-0506, AIAA, January 2000.

[84] Hubner, J.P., Carroll, B.F., and Schanze, K.S. Heat Transfer Measurements in Hypersonic Flow Using Luminescent Coating Techniques. Paper 2002-0741, AIAA, January 2002.

[85] Crafton, J., Lachendro, N., Guille, M., Sullivan, J.P., and Jordan, J.D. Application of Temperature and Pressure Sensitive Paint to an Obliquely Impinging Jet. Paper 99-0387, AIAA, January 1999.

[86] Chen, L.A. DuPont Titanium Technologies Technical Support. Private Communication, January 21, 2003.

[87] Iijima, Y., Kanda, H., Kunimasu, T., and Asai, K. Sample Tests of Temperature-Sensitive Paints with 18 Different Formulations (Japanese Text). 59th Wind Tunnel Research Conference, November 1997.

[88] Nakakita, K. and Asai, K. Pressure-Sensitive Paint Application to a Wing-Body Model in a Hypersonic Shock Tunnel. Paper 2002-2911, AIAA, June 2002.

[89] Shimbo, Y., Noguchi, M., and Makino, Y. Blowdown Tunnel Application of Pressure Sensitive Paint. Paper 99-3169, AIAA, June 1999.

[90] Schairer, E.T., Mehta, R.D., and Olsen, M.E. Effects of Pressure-Sensitive Paint on Experimentally Measured Wing Forces and Pressures. *AIAA Journal*, 40(9):1830-1838, September 2002.

[91] Schairer, E.T. Optimum Thickness of Pressure-Sensitive Paint for Unsteady Measurements. *AIAA Journal*, 40(11):2312-2318, November 2002.

[92] Cattafesta III, L.N. and Moore, J.G. Uncertainty Estimates for Luminescent Temperature-Sensitive Paint Intensity Measurements. Paper 95-2193, AIAA, June 1995.

[93] Novak, K. Rectification of Digital Imagery. *Photogrammetric Engineering & Remote Sensing*, 58:339-344, 1992.

[94] Donovan, J.F., Morris, M.J., Pal, A., Benne, M.E., and Crites, R.C. Data Analysis Techniques for Pressure- and Temperature-Sensitive Paint. Paper 93-0176, AIAA, January 1993.

[95] Weaver, W.L., Jordan, J.D., Dale, G.A., and Navarra, K.R. Data Analysis Methods for the Development and Deployment of Pressure Sensitive Paints. Paper 99-0565, AIAA, January 1999.

[96] Devereux, B.J., Fuller, M., Carter, L., and Parsell, R.J. Geometric Correction of Airborne Scanner Imagery by Matching Delaunay Triangles. *International Journal of Remote Sensing*, 11(12):2237-2251, 1990.

[97] Shanmugasundaram, R. and Samareh-Abolhassani, J. Modified Scatter Data Interpolation Used to Correct Pressure Sensitive Paint Images. Paper 95-2041, AIAA, June 1995.

[98] Bell, J.H. and McLachlan, B.G. Image Registration for Pressure-Sensitive Paint Applications. *Experiments in Fluids*, 22:78-86, 1996.

[99] Le Sant, Y. and Merienne, M-C. An Image Resection Method Applied to Mapping Techniques. Proceedings from ICIASF, 1995.

[100] Abdel-Aziz, Y.I. and Karara, H.M. Direct Linear Transformation from Comparator Coordinates into Object Space Coordinates in Close-Range Photogrammetry. Proceedings from the Symposium on Close-range Photogrammetry, pg 1-18, 1971.

[101] Liu, T. Geometric, Kinematic and Radiometric Aspect of Image-Based Measurements. Paper 2002-3239, AIAA, June 2002.

[102] Tsai, R.Y. A Versatile Camera Calibration Technique for High-Accuracy 3D Machine Vision Metrology Using Off-the-Shelf TV Cameras and Lenses. *IEEE Journal of Robotics and Automation*, RA-3(4):323-344, August 1987.

[103] Karara, H.M. and Abdel-Aziz, Y.I. Accuracy Aspects of Non-Metric Imageries. *Photogrammetric Engineering*, pg. 1107-1117, 1974.

[104] Liu, T., Cattafesta III, L.N., Radeztsky, R.H., and Burner, A.W. Photogrammetry Applied to Wind-Tunnel Testing. *AIAA Journal*, 38(6):964-971, June 2000.

[105] Goffe, W. L., Ferrier, G. D., and Rogers, J. Global Optimization of Statistical Functions with Simulated Annealing. *Journal of Econometrics*, Vol. 60, No. 1-2, pg. 65-99, January-February 1994.

[106] Press, W.H., Flannery, B.P., Teukolsky, S.A., and Vetterling, W.T. Numerical Recipes in Fortran: The Art of Scientific Computing. Cambridge University Press, Copyright 1992.

[107] Crossley, W.A. Genetic Algorithm for Global Optimization. AAE 590G, School of Aeronautics and Astronautics, Purdue University, 2000.

[108] Hollis, B.R. User's Manual for the One-Dimensional Hypersonic Aero-Thermodynamic (IDHEAT) Data Reduction Code. NASA CR-4691, August 1995.

[109] Asai, K., Kunimasu, T., and Iijima, Y. Visualization of the Quiet Test Region in a Supersonic Wind Tunnel Using Luminescent Paint. Proceedings from the 17th ICIASF, 1997.

[110] Liu, T., Campbell, B.T., Sullivan, J.P., Lafferty, J., and Yanta, W. Heat Transfer Measurement on a Waverider at Mach 10 Using Fluorescent Paint. *Journal of Thermophysics and Heat Transfer*. 9(4):605-611, October-December 1995.

[111] Radeztsky, R.H., Reibert, M.S., and Saric, W.S. Effect of Isolated Micron-Sized Roughness on Transition in Swept-Wing Flows. *AIAA Journal*, 37(11):1370-1377, November 1999.

[112] Fay, J.A. and Riddell, F.R. Theory of Stagnation Point Heat Transfer in Dissociated Air. *Journal of Aerospace Sciences*, 25(2):73-85, 121, 1958.

[113] Daryabeigi, K., Berry, S.A., Horvath, T.J., and Nowak, R.J. Finite Volume Numerical Methods for Aeroheating Rate Calculations From Infrared Thermographic Data. Paper 2003-3634, AIAA, June 2003.

APPENDIX

APPENDIX

This section will give a brief description of the data reduction routines developed for this research. The discussion will cover the data reduction up to the calculation of the heat-transfer rates. Further processing and analysis (such as the spectral analysis) is considered specific to the research problem of interest, and not appropriate for a general overview. No official name has been given to the complete software package, however for reference purposes it will be referred to as PM6PP (Purdue Mach 6 Paints Processor). The routines are available either through the author or the faculty advisor, and are unlimited distribution.

PM6PP is specifically written to automate as much of the data and image-processing that is necessary for image-based measurement systems. PM6PP is currently written specifically for TSP applications using the intensity-based method. However, adapting the codes to handle PSP and lifetime methods should be relatively straight-forward, and is encouraged as a future developmental task. The implementation of automated routines require the development of not only codes which contain automation logic, but the development of the total data reduction system. This includes features such as standardized file names, use of file and directory structures, PC and UNIX machine compatibility, and so on.

PM6PP uses both Matlab and Fortran routines. All of the pre-processing codes which require user input are run within Matlab, which then may call compiled executables written in Fortran. Because of the vast number of subroutines, it is highly recommended that the routines be well-organized (preferably in the original directory structure), and the directories be added to the path in order for them to be accessible from any working directory. A SEPARATE DIRECTORY MUST BE USED FOR EACH TUNNEL RUN, and named “RUN**”. For run numbers 1-9, they must be labeled using two digits, for example “Run01”. A single tunnel run can have multiple wind-on images,

but this is treated as a single tunnel run. All of the file names described within the discussion must be kept consistent throughout all tunnel run cases. In addition, a text file containing the test conditions is necessary in the root-directory where the individual run-directories are located.

The data reduction tasks are split into seven main steps listed below. A description of each step will be given.

1. Determine test conditions. This includes the freestream conditions and the model temperature.
2. Generate a grid of the registration marks on the model.
3. Record the pixel locations of the registration marks.
4. Construct the image-mapping equations.
5. Map the dark, wind-off, and wind-on images onto the grid.
6. Apply the temperature calibration to the mapped intensity ratio image.
7. Apply the heat-transfer model to the temperature image.

1. Determining Test Conditions

user code: condition.m

input files:

plenum.trc	oscilloscope record of the plenum pressure (trigger signal for plenum.trc, pulse.trc)
pulse.trc	5-volt output from the CCD camera
contrac.trc	oscilloscope record of the contraction pressure
pulses.trc	5-volt output from the CCD camera, short trace (trigger signal for pulses.trc and contrac.trc)
contraction.txt	calibration data for the contraction pressure transducer
plenum.txt	calibration data for the plenum pressure transducer

This routine will determine the time interval between tunnel startup and image acquisition. The mean total pressure and temperature, and unit Reynolds number during image-acquisition will also be determined. If the run contains multiple wind-on images, then the time intervals between each images, and the flow condition for each will also be determined. These must be manually recorded into conditions.txt.

2. Generate a Grid of the Registration Marks on the Model

output files:	pointid.txt	ID numbers of each registration mark, their dimensional coordinates, and the region of the model which they are located in.
	regiondef.txt	defines the coordinates of each region the model is split into

These two files will then be used as input files for other routines during the data reduction process. These two files must be generated manually. It is recommended that these two files be stored in a separate directory away from the experimental data. If the registration mark locations are standardized, then these files could be used for several sets of data.

3. Record the Pixel Locations of the Registration Marks

user code:	ptfinder.m	
input files:	grid.txt	contains the pixel locations of the registration marks IN THE GRID, NOT IN THE IMAGES
output files:	allpts.txt	contains the pixel locations of the registration marks in the images

The pixel locations of each registration mark are recorded. This process is automated using feature recognition programming techniques. However, this

process cannot be made fail-proof, and consequently the user must either accept or reject each point that is detected by the algorithm. The routine searches for the number of points that are listed in grid.txt. In some instances, the routine may not be able to find all of the points. The output file allpts.txt is outputted to take this into account. The user can accept it as is, or may be modified manually. The feature recognition algorithm generally works well (finding ALL of the points correctly) provided that the registration marks are applied to the model neatly and clearly.

4. Construct the Image-Mapping Equations.

user code:	findcoef.m	
input files:	allpts.txt	
output files:	coefs.txt	contains the coefficients of the image-mapping equations

The coefficients of the image-mapping equations are solved using the pixel locations stored in allpts.txt.

5. Map the Dark, Wind-Off, and Wind-On Images onto the Grid

user code:	mapper.m	
input files:	coefs.txt	
	on1.tif	first wind-on image
	on2.tif	second wind-on image (if it exists)
	off.tif	wind-off image
	dark.tif	dark image
output files:	on1c.tif	corrected first wind-on image
	on2c.tif	corrected second wind-on image (if it exists)
	offc.tif	corrected wind-off image
	darkc.tif	corrected dark image

The image-mapping equations are applied to the images. This routine typically takes 5-10 minutes on a UNIX machine or a Pentium-IV machine. It is recommended to be executed on one of the UNIX machines, so that the PC could be used for other tasks (such as the image registration of other tunnel runs).

6. Apply the Temperature Calibration

user code:	tsptemp.m	
input files:	tspcal.txt	contains the TSP temperature calibration data
	conditions.txt	
output files:	temp.mat	contains the 2X2XN matrix of the temperature image (Matlab binary file format)

Applies the a-priori temperature calibration data to the intensity ratio image. The reference temperature (temperature of model prior to tunnel run) is automatically read from the conditions.txt file.

7. Apply the Heat-Transfer Model

user code:	tspheat.m	
input files:	temp.mat	
	conditions.txt	
	tgrid.txt	contains the insulator thickness measurements in a look-up table format
	thickness.txt	contains the mean thickness of the insulator for each regions defined in the regiondef.txt file.
output files:	heatx.mat	contains the 2X2XN matrix of the heat-transfer image (Matlab binary file format)

The heat-transfer rate is computed using Fourier's Law. Several prompts will be made by the routine which gives the user options on how to use the insulator thickness measurements. ONLY ONE OF THE TWO THICKNESS FILES

SHOULD BE PRESENT IN THE WORKING DIRECTORY. If a thickness grid is to be used, then thickness.txt file should be removed from the working directory, and vice-versa as well.